Molecular simulations of reversible mechanical unfolding and of phospholipid bilayers

Dissertation

zur Erlangung des Grades
"Doktor der Naturwissenschaften"
im Promotionsfach Chemie

dem Fachbereich Chemie, Pharmazie und Geowissenschaften
der Johannes Gutenberg-Universität
in Mainz vorgelegt

von

Stefan Jaschonek
geboren in Tübingen

Mainz, 2017

Dekan:

1. Gutachter:
2. Gutachter:

Tag der mündlichen Prüfung:

Contents

List of Abbreviations

AA	all-atom
AFM	atomic force microscope
AIMD	*ab initio* MD
APL	area per lipid
BO	Born-Oppenheimer
CG	coarse-grained
CHOL	cholesterol
DOPC	1,2-dioleoyl-*sn*-glycero-3-phosphocholine
DPPC	1,2-dipalmitoyl-*sn*-glycero-3-phosphocholine
FE	force extension
FPMD	force probe molecular dynamics
HB	hydrogen bonds
KMC	kinetic Monte Carlo
MD	molecular dynamics
MFPT	mean first passage time
NPT	isobaric-isothermal ensemble
NVT	canonical ensemble
OPLS	Optimized Potentials for Liquid Simulations
PBC	periodic boundary conditions
PF	particle-field
PME	particle-mesh Ewald
PMF	potential of mean force
PPPF	particle-particle particle-field
RE	end-to-end distance extension
SCF	self consistent field
STM	scanning tunneling microscope
UE	urea-ether
UU	urea-urea

1. Introduction

Molecular dynamics (MD) simulations of soft matter have become one of the most versatile and powerful tools in chemistry and molecular biology. They serve as a computational microscope and it is possible to capture key biochemical processes such as protein folding, drug binding and membrane transport. [1] Due to MD simulations the early view of proteins as relatively rigid structures was replaced by a dynamic model in which the internal motions and resulting conformational changes play an essential role in their function. [2]
MD methods were conceived within the theoretical physics community during the 1950s. In 1957 the earliest MD simulation was performed by Wainwright using the so called hard-sphere model. [3] These simulation techniques were refined to mimic real atomic interactions [4]. By then important breakthroughs in structural biology have provided many atomic-resolution models of molecules essential to life such as proteins and nucleic acids. The first MD simulation of a system of biological interest was performed by McCammon [5] in 1977 and concerned the bovine pancreatic trypsin inhibitor. It was performed in vacuum with a crude molecular dynamic potential and lasted only for 9.2 ps but let to the realization that biological molecules are indeed dynamic systems. [1, 5]
Fast forward to now, improvements in achievable simulation speed and underlying physical models have enabled atomic-level simulations on timescales as long as milliseconds. [1] Even though speed and accuracy have improved significantly, the basic form of simulation has endured. Typically the underlying models for MD simulations consist of spherical atoms connected by springs which represent bonds. Forces experienced in the model are described using simple mathematical functions. With such simple models, MD simulations numerically solve Netwon's equation of motion and therefore structural fluctuations can be observed with respect to time. [6] MD simulations allow therefore to investigate structural changes like in protein folding which is essential for the understanding of the function of many processes in the body. Often, these structural changes occur on much slower time scales than those accessible with conventional simulation techniques. Force probe MD (FPMD) simulations provide powerful means to overcome this limitation and to get insight into the atomistic mechanisms. [7] By applying an external force molecules unfold much faster and the computational cost is therefore greatly reduced.
Besides folding processes also biomembranes are intensively investigated using MD techniques. [8] In order to observe physiological relevant processes, the time and length scales accessible by an atomistic approach are not suitable. Approaches such as coarse-grained (CG) models and particle-field (PF) models allow to access such time scales. [9, 10]
This thesis is structured as follows: In chapter 2 the theoretical background used in this work is covered. There, the focus is on different approaches of MD simulations techniques. Furthermore, this chapter gives a short introduction on stochastic models used to rationalize the results of FPMD simulations.
Chapter 3 covers the work on reversibly unbinding model systems calix[4]arene-catenanes. Here, the goal is to study the dependence of FPMD simulations on the pulling parameters for three different variations of this model system. Chapter 4 comprises the studies done on phospholipid bilayers. The focus in this chapter is on the correct representation of the phase behavior over a range of temperatures using CG and PF approaches. In order to achieve this, new refined models

of phospholipids and cholesterol are introduced and discussed.
In chapter 5 a summary of the entire work is given. Furthermore an outlook an potential improvements and future investigation of the systems studied in this work is presented.

2. Theory

2.1. Molecular dynamics simulations

Molecular dynamics (MD) is a simulation method to study the dynamical evolution of a system consisting of atoms and molecules. To describe such an evolution correctly, the time-dependent Schrödinger equation has to be solved. This is a rather complicated task and can be simplified using the Born-Oppenheimer (BO) approximation. [11] With this approximation the motion of the atomic nuclei and the electrons can be separated. Instead of solving the time-dependent Schrödinger equation for the nuclei one usually neglects quantum effects and solves the classical equations of motion. The forces among the nuclei are deduced from the Born-Oppenheimer potential for each configuration of the nuclei via a solution of the electronic Schrödinger equation and the resulting method is called *ab initio* MD (AIMD). [12] Due to the computational cost of AIMD, it is only possible to simulate smaller systems ($\approx$ 500 atoms) for short periods of time ($\approx 50\,\mathrm{ns}$). [13]
Another approach is taken in classical MD simulations where the BO potential is approximated by an empirical force field. MD simulations numerically solve the classical equations of motion which are given for a simple system of particles by

$$m_i \ddot{\mathbf{r}}_i = \mathbf{F}_i(\mathbf{r}_i) \qquad \text{with} \qquad \mathbf{F}_i(\mathbf{r}_i) = -\frac{\partial}{\partial \mathbf{r}_i} U(\{\mathbf{r}\}). \tag{2.1}$$

with the BO potential $U(\{\mathbf{r}\})$. $\mathbf{r} = \mathbf{r}_1, \mathbf{r}_2, \ldots \mathbf{r}_N$ describes the complete set of $3N$ nuclear coordinates. [14, 15]
The potential energy of the BO potential is given as a set of functions and parameters. The different types of potential functions are discussed in section 2.1.1. Potential functions and their parameters form a so-called force field.
It is obvious that every MD program requires a good algorithm to integrate classical equations of motion. This is the center part of every MD simulation. One of the most common algorithms, the leap frog integrator, is described in section 2.1.2.
To set up a MD simulation, a box with a certain volume V is chosen and the particles are placed inside the box. The number of particles is limited by computational cost. This gives rise to several problems because the aim of MD simulations is to provide information about the properties of a macroscopic system. The simulated systems are too small and far away from the thermodynamic limit. For such small systems, boundary conditions do not have a negligible effect because for N particles in a system, roughly $N^{2/3}$ are at the surface. Even for a system consisting of $N = 10^6$ particles this would mean that $1\,\%$ are at the surface. One way to treat the problem is to use periodic boundary conditions (PBC) (cf. App. A.1).
To carry out a simulation at experimental conditions, e.g. at constant temperature and pressure, methods to control these parameters have to be included in a simulation. These methods are discussed in section 2.1.3.

2.1.1. Force fields

The various interactions in a system consisting of particles or molecules are described by potential functions. A set of potential functions and their parameters form a force field. There are various force fields which use different potential functions and parameters. Here, the potential functions used in the OPLS-AA (Optimized Potentials for Liquid Simulations All-Atom) force field are presented. All-atom (AA) means, that every atom is represented in this force field. A force field in which groups of atoms are reduced to point masses is discussed in section 2.1.4. In general, the potential functions are split into two parts: bonded and non-bonded interactions

$$U = U_{\text{bonded}} + U_{\text{non-bonded}}. \tag{2.2}$$

Bonded interactions

The bonded interactions are given by three different dominant contributions to the bonding potentials

$$U_{\text{bonded}} = U_{\text{bond}}(k_{\text{AB}}, r_{\text{AB}}) + U_{\text{angle}}(k_{\text{BCD}}, \theta_{\text{BCD}}) + U_{\text{dihedral}}(k_{\text{ABCD}}, \omega_{\text{ABCD}}) \tag{2.3}$$

with the bond stretching potential U_{bond}, the bond angle potential U_{angle} and the dihedral angle potential U_{dihedral}. An illustration of these potentials and their parameters, the interatomic distance r_{AB}, bond angle θ_{BCD} and torsion angle ω_{ABCD} are given in Figure 2.1.

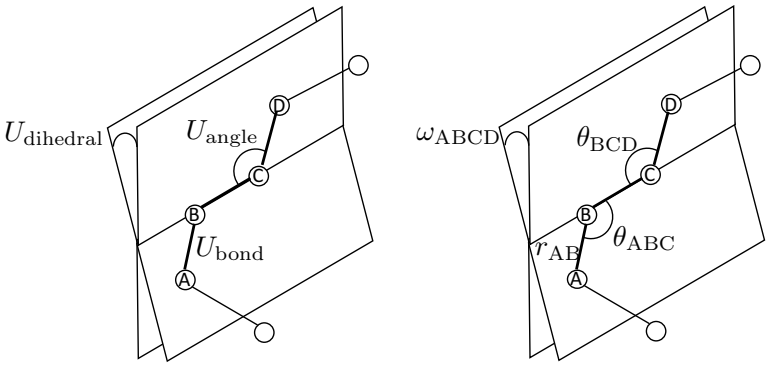

Figure 2.1.: Illustration of the definition of the different bonded potentials; interatomic distance r_{AB}, bond angle θ_{BCD} and torsion angle ω_{ABCD} .

Bond stretching potential The bond stretching potential U_{bond} between the atoms A and B should have an analytic form and must be continuously differentiable. A popular form for such a potential is a harmonic approximation

$$U_{\text{bond}} = \frac{1}{2} \sum_{\text{bonds}} k_{AB}(r_{AB} - r_{\text{eq}})^2 \tag{2.4}$$

with the force constant k_{AB} and the equilibrium distance r_{eq}. For most MD simulations eq. (2.4) is a good approximation and k_{AB} is derived from either quantumchemical calculations or from experiment.

Bond angle potential In MD simulations the potential for the angular deformations is typically described by

$$U_{\text{angle}} = \frac{1}{2} \sum_{\text{angles}} k_{ABC}(\theta_{ABC} - \theta_{\text{eq}})^2 \tag{2.5}$$

where θ_{ABC} is the valence angle between the bonds AB and BC (see Figure 2.1) and k_{ABC} is the force constant for the angular deformation.

Dihedral angle potential The dihedral angle potential is chosen as a periodic function and depends on the dihedral angle ω_{ABCD}

$$U_{\text{dihedral}} = \frac{1}{2} \sum_{\text{dihedrals}} \sum_{m} k_{ABCD}^{\omega,m}(1 + \cos(m\omega_{ABCD} - \gamma_m)). \tag{2.6}$$

$k_{\text{ABCD}}^{\omega,m}$ is the force constant, γ_m and m are parameters of the periodic function and describe the phase shift as well as the number of minima in the potential.

Non-bonded interactions

The non-bonded interactions are split into the van der Waals (vdW) interactions U_{vdW} and the Coulomb interactions V_{Coulomb}:

$$U_{\text{non-bonded}} = U_{\text{vdW}} + U_{\text{Coulomb}}. \tag{2.7}$$

van der Waals interactions Van der Waals interactions are *short-range* interactions and are usually described by the Lennard-Jones potential. The Lennard-Jones potential for two atoms A and B is given by

$$U_{\text{LJ}}(r_{\text{AB}}) = 4\varepsilon \left[\left(\frac{\sigma}{r_{\text{AB}}} \right)^{12} - \left(\frac{\sigma}{r_{\text{AB}}} \right)^{6} \right]. \tag{2.8}$$

ε is the depth of the of the potential and σ denotes the characteristic radius. The Lennard-Jones potential consists of an repulsive r^{12}-term and an attractive r^6-term representing vdW interactions. An illustration of the Lennard-Jones potential, its attractive and repulsive terms and the parameters are shown in Figure 2.2.

Coulomb interactions Coulomb interactions are *long-range* electrostatic interactions between two atoms A and B. Assigning a charge to each atom, the Coulomb potential is given by

$$U_{\text{Coulomb}}(r_{\text{AB}}) = \frac{q_{\text{A}} q_{\text{B}}}{4\pi\epsilon_0 r_{\text{AB}}} \tag{2.9}$$

with the charges q_{A} and q_{B} and the vacuum permittivity ε_0.
Due to the long-range nature ($U_{\text{Coulomb}} \propto r^{-1}$), the forces among all particles have to be computed which is very demanding. The long-range contributions are therefore calculated separately from

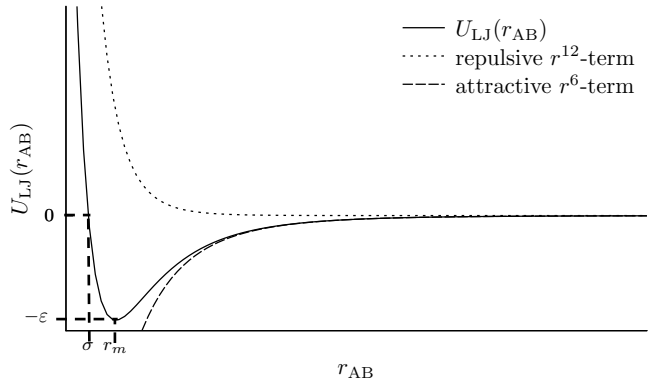

Figure 2.2.: Illustration of the Lennard-Jones potential $V_{\mathrm{LJ}}(r_{\mathrm{AB}})$. The minimum is at $r_m = \sqrt[6]{2}\sigma$.

the short-range interactions. This can be done by Ewald summation ($\mathcal{O}(N^{3/2})$) [16], fast multipole methods ($\mathcal{O}(N)$) [17] and particle-mesh based methods ($\mathcal{O}(N \log N)$) such as particle-mesh Ewald (PME). [18]
PME was used for all the classical MD simulations performed in this work. It is a method to reduce computational cost when calculating the Coulomb contribution to the potential energy. The basic idea is outlined next and a schematic illustration is shown in Figure 2.3.
The horizontal line in Figure 2.3 (a) represents a one dimensional unit cell and the straight lines represent the point charges A, B and C. The aim is to calculate the interaction of point charge A with all other point charges (here: B and C).

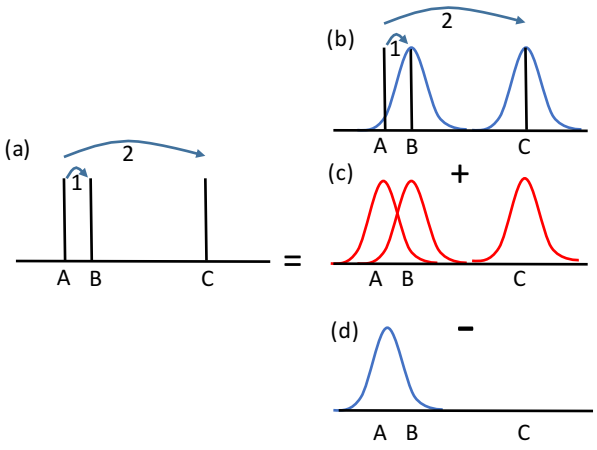

Figure 2.3.: Illustration of the PME method. The point charges are represented by straight lines, the screening charges by blue curves and the compensating screening charges by red curves. The horizontal line represents the length of the unit cell.

To improve the situation gaussian distribution of charges of opposite sign than the point charges are added to all point charges except A, thereby acting as screening charges. Because there is no overlap between point charge A and screening charge C, C is completely screened from A and interaction 2 does therefore no longer contribute. Interaction 1 still contributes as B is not

completely screened from A. This is illustrated by the overlap of the screening charge curve with the straight line for point charge A.
In order to compensate for the error that was introduced through the use of the screening charges, compensating screening charges of opposite sign than the ones marked in blue are added, cf. (c). The contribution of these compensating charges can easily be calculated by a fast converging Fourier series at low computational cost. This contribution is the same for all interactions and has therefore only to be calculated once.
Finally, the contribution of the compensating screening charge at A must be removed by adding a screening charge of opposite sign at A as shown in (d). The procedure outlined here is very efficient and greatly reduces computational cost ($\mathcal{O}(N \log N)$).

2.1.2. Integration of the equations of motion

After deriving the forces from listed potentials, the next step is to solve the equations of motion with a fast and efficient algorithm in order to get the positions $\mathbf{r}_i$ and the velocities $\mathbf{v}_i$ as a function of time. Within MD programs, these equations are solved numerically using a time step Δt. In this work the *leap frog* algorithm was used and is described in the following.
The leap frog integrator evaluates the velocities, $\mathbf{v}_i = \frac{d\mathbf{r}_i(t)}{dt}$, at half time steps and uses the velocities to calculate the new positions. The velocities can be written as

$$\begin{aligned} \mathbf{v}_i(t - \Delta t/2) = &\quad \frac{\mathbf{r}_i(t) - \mathbf{r}_i(t - \Delta t)}{\Delta t} \\ \mathbf{v}_i(t + \Delta t/2) = &\quad \frac{\mathbf{r}_i(t + \Delta t) - \mathbf{r}_i(t)}{\Delta t} \end{aligned} \tag{2.10}$$

and an expression for the new positions based on the old positions and velocities can be obtained via

$$\begin{aligned} \mathbf{r}_i(t - \Delta t) = &\quad r(t) - \Delta t\, \mathbf{v}_i(t - \Delta t/2) \\ \mathbf{r}_i(t + \Delta t) = &\quad r(t) + \Delta t\, \mathbf{v}_i(t + \Delta t/2). \end{aligned} \tag{2.11}$$

The leapfrog integrator uses a truncated Taylor expansion up to second order of the particle coordinates $\mathbf{r}_i(t \pm \Delta t)$:

$$\begin{aligned} \mathbf{r}_i(t + \Delta t) = &\quad \mathbf{r}_i(t) + \dot{\mathbf{r}}_i(t)\Delta t + \frac{1}{2}\ddot{\mathbf{r}}_i(t)\Delta t^2 \\ \mathbf{r}_i(t - \Delta t) = &\quad \mathbf{r}_i(t) - \dot{\mathbf{r}}_i(t)\Delta t + \frac{1}{2}\ddot{\mathbf{r}}_i(t)\Delta t^2 \end{aligned} \tag{2.12}$$

Summing these equations

$$\mathbf{r}_i(t + \Delta t) = 2\mathbf{r}_i(t) - \mathbf{r}_i(t - \Delta t) + \ddot{\mathbf{r}}_i(t)\Delta t^2 \tag{2.13}$$

and subsitution with eqs. (2.11) yields

$$\mathbf{v}_i(t + \Delta t/2) = \mathbf{v}_i(t - \Delta t/2) + \ddot{\mathbf{r}}_i(t)\Delta t. \tag{2.14}$$

By inserting Newton's second law $\mathbf{F}_i(t) = m_i\ddot{\mathbf{r}}_i(t)$, the expression for the update of the velocities is obtained:

$$\mathbf{v}_i(t + \Delta t/2) = \mathbf{v}_i(t - \Delta t/2) + \frac{\mathbf{F}_i(t)}{m_i}\Delta t. \tag{2.15}$$

Within a simulation, the positions $\mathrm{r}(t + \Delta t)$ (2.11) and the the velocities $\mathrm{v}(t + \Delta t/2)$ (2.15) are calculated at interleaved time points. An illustration of the algorithm is shown in Figure 2.4. [14]

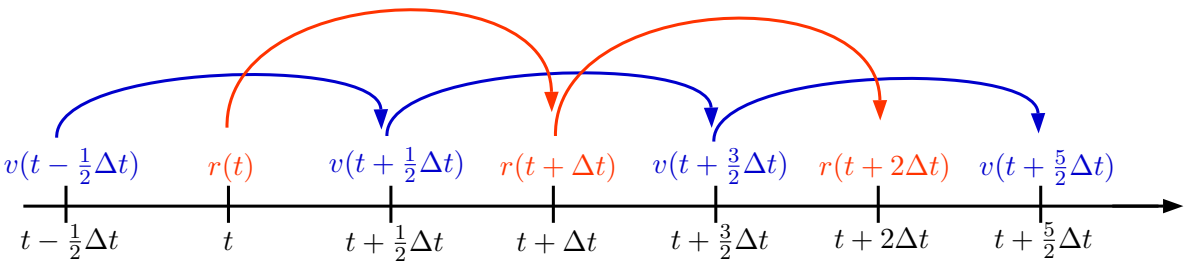

Figure 2.4.: Illustration of the leapfrog integrator.

2.1.3. Statistical ensemble

It is straight forward to perform a MD simulation in the microcanonical ensemble. Here, the volume V and the number of particles N is kept constant and the energy E is conserved. Because of these constant parameters, the microcanonical ensemble is also-called the NVE ensemble. The NVE ensemble is easy to implement but not the most reasonable choice because the energy is not observable in experiments. Hence, methods to control the pressure P and temperature T are needed in order to realize the canonical (NVT) ensemble and the isobaric-isothermal (NPT) ensemble. A short outline of these ensembles and how the temperature T and the pressure P can be controlled is given in the following.

Canonical ensemble (NVT)

In the canonical ensemble, the volume and the temperature have to be constant. The temperature is related to the kinetic energy U_{kin} via

$$\sum_{i=1}^{3N} \frac{m_i \mathbf{v}_i^2}{2} = \frac{k_B T}{2} f \tag{2.16}$$

where N is the number of particles, f denotes the number of the degrees of freedom and $k_B T$ is the thermal energy ($k_B = 1.38064852 \cdot 10^{-23}\,\mathrm{m^2\,kg\,s^{-2}\,K^{-1}}$). The temperature can be altered by scaling the velocities. This can be achieved by multiplying the velocities with a scaling factor λ. According to eq. (2.16), the temperature T at time t is given by $T(t) = \sum_i^N \frac{m_i \mathbf{v}_i^2}{f k_B}$ and the change in temperature ΔT can be calculated by

$$\Delta T = \sum_{i}^{3N} \frac{m_i \lambda^2 \mathbf{v}_i^2}{f k_B} - \sum_{i}^{3N} \frac{m_i \mathbf{v}_i^2}{f k_B} = (\lambda^2 - 1) T(t). \tag{2.17}$$

By simply multiplying the velocities at each time step with $\lambda = \sqrt{T_0 / T(t)}$, where T_0 is the desired temperature, the temperature is kept constant. This simple *velocity scaling* approach gives rise to one problem: it does not allow for fluctuations in temperature which are present in the canonical ensemble.
The *Berendsen thermostat* uses a more flexible approach. The system is coupled to an external heat bath with a fixed temperature T_0. Here, the rate of change in temperature is proportional to the difference in temperature

$$\frac{dT(t)}{dt} = \frac{T_0 - T(t)}{\tau_T} \tag{2.18}$$

where τ_T is a coupling parameter. This parameter describes the strength of the coupling. The change in temperature between two successive time steps Δt is

$$\Delta T = \frac{\Delta t}{\tau_T}(T_0 - T(t)). \tag{2.19}$$

The velocities are then scaled by

$$\lambda_T = \sqrt{1 + \frac{\Delta t}{\tau_T}\left(\frac{T_0}{T(t-\Delta t)} - 1\right)}. \tag{2.20}$$

The coupling parameter τ_T is an empirical parameter. For the limit $\tau_T \to \infty$ the Berendsen thermostat is inactive and the simulation is sampling a microcanonical ensemble. When the parameter τ_T is chosen too small, the fluctuations in temperature are unrealistically small. For $\tau_T = \Delta t$, λ_T is equal to the scaling factor used in velocity scaling. [19]

Isobaric-isothermal ensemble (NPT)

The isobaric-isothermal ensemble is of great interest because most experiments are carried out at a constant pressure and a constant temperature. To keep the pressure constant, the box size and the coordinates of the particles are scaled at every time step Δt which can be done by various different barostats. The pressure is given by

$$P = \frac{2}{3V}(U_{\text{kin}} - \Xi) \tag{2.21}$$

with the box volume V and the inner virial scalar

$$\Xi = -\frac{1}{2}\sum_{i<j} \mathbf{r}_{ij}\mathbf{F}_{ij} \qquad \text{with} \qquad \mathbf{r}_{ij} = \mathbf{r}_i - \mathbf{r}_j \tag{2.22}$$

where $\mathbf{F}_{ij}$ is the force on particle i due to particle j. The pressure in a simulation can be corrected by a change of Ξ.
Similar to the approach in the Berendsen thermostat, in the *Berendsen barostat* the rate of change in pressure is proportional to the difference in pressure

$$\left(\frac{dP}{dt}\right)_{\text{bath}} = \frac{P_0 - P}{\tau_P} \tag{2.23}$$

where P_0 is the reference pressure and τ_P is a coupling parameter. The change in the coordinates and the volume of the box is given by

$$\frac{d\mathbf{r}}{dt} = \lambda_P \mathbf{r} \tag{2.24}$$

and

$$\frac{dV}{dt} = 3\lambda_P V \tag{2.25}$$

where λ_P is the scaling parameter. A change in pressure is related to the isothermal compressibility κ via

$$\frac{dP}{dt} = -\frac{1}{\kappa V}\frac{dV}{dt}. \tag{2.26}$$

With eqs. (2.25) and (2.23) this results in

$$\lambda_P = \frac{\kappa(P_0 - P)}{3\tau_P}. \tag{2.27}$$

The latter equation assumes that the system is isotropic and placed in a cubic box. [19]

2.1.4. Coarse grained molecular dynamics simulations

In contrast to all-atom (AA) molecular dynamics simulations in a coarse grained (CG) model one averages over some features of the system in a prescribed manner. The resulting reduction of the number of degrees of freedom leads to a smoother energy landscape, i.e., the potential energy as a function of all coordinates, which is faster to equilibrate. With this approach it is possible to study larger systems at longer time scales at lower computational cost. On the other hand, however, these approximations lead to a decreased accuracy of the simulations. [20]
The CG approach is widely used in MD simulations. In classical MD, CG usually refers to a simplified molecular system which is obtained by reducing groups of atoms to point masses, so-called "beads". This transformation from a fine to a coarse grained model is referred to as mapping. Another possibility to save computational cost is a field approach for the intermolecular interactions. Here, a molecule is not directly interacting with its surrounding particles but through a field which is represented by a CG density. [21]
An important aspect of the CG procedure is parametrization. Even though CG MD models are less accurate than its atomistic counterparts, the correct physical behavior should approximately be preserved. Two basic strategies are used to do this: the *bottom-up* and the *top-down* method. In the bottom-up method, simulations, models or experiments on a more detailed scale are used to parametrize a model at a more coarse grained scale. Alternatively, one can also use properties measured in bulk in order to parametrize simulations on a much smaller scale. This is done in top-down modeling approaches. [9, 20]

Martini force field

The Martini force field is a CG model developed for biomolecular simulations. [9] The beads used are constructed from the functional groups of the underlying AA system. It has been used successfully in simulations of important biochemical processes such as lipid self-assembly [22], peptide membrane binding [23] and protein-protein recognition. [24]
An illustration for the mapping procedure can be found in Figure 2.5 (a) and (b). The potential functions used for the bonded and non-bonded interactions are the same as already discussed in section 2.1.1. [9]

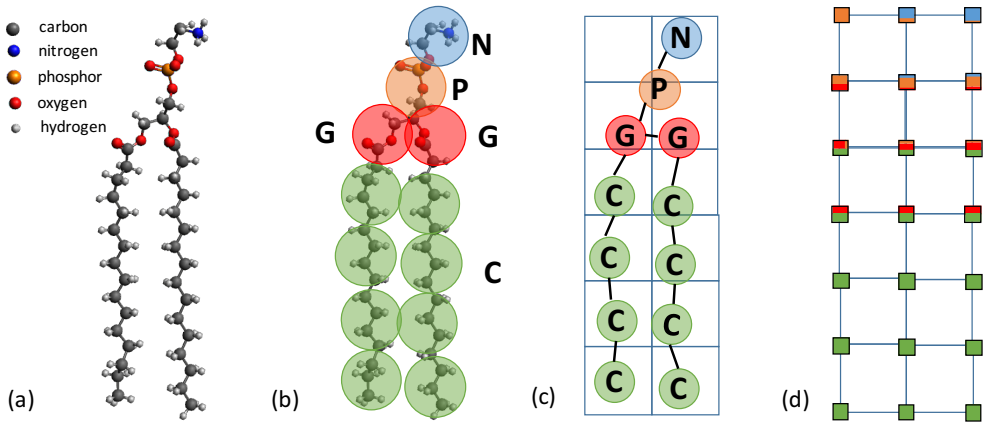

Figure 2.5.: Illustration of the mapping procedure for dipalmitoylphosphatidylcholine (DPPC). (a) All atom model of DPPC, (b) mapping of DPPC into the Martini force field, (c) simplified CG model of DPPC with an overlaying lattice and (d) CG density field for the SCF MD simulations. [9, 25]

Self consistent field MD

In self consistent field (SCF) MD, the evaluation of the non-bonded force between atoms/beads of different molecules is replaced by the evaluation of the external force which depends on the local particle density at position $\mathbf{r}_I$. The overall particle density at point $\mathbf{r}_I$ is given by

$$\rho(\mathbf{r}_I) = \rho_{\mathrm{A}}(\mathbf{r}_I) + \rho_{\mathrm{B}}(\mathbf{r}_I) + \rho_{\mathrm{C}}(\mathbf{r}_I) + \cdots \tag{2.28}$$

where the $\rho_{\mathrm{X}}(\mathbf{r}_I)$ are the partial particle densities of the different beads/atom types $\mathrm{X} = \mathrm{A}, \mathrm{B}, \mathrm{C}, \cdots$. This density $\rho(\mathbf{r}_I)$ can then further be simplified by mapping it to a coarse grained density $\rho_{\mathrm{CG}}(\mathbf{r}_{\tilde{I}})$ where $\mathbf{r}_{\tilde{I}}$ represent points on a grid.
The mapping procedure for a single molecule consisting of beads for the CG particle density is shown in Figure 2.5. A lattice is chosen and a fraction of the particle density is assigned to each lattice point (Figure 2.5 (c) and (d).) The closer a bead is to a lattice point, the larger the fraction of the particle density of this bead at that point. In this way, one can also map systems consisting of several molecules. An illustration of the resulting CG density is shown in Figure 2.6.

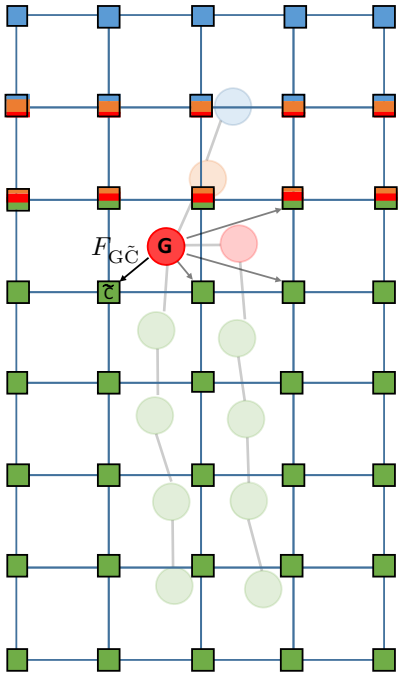

Figure 2.6.: Illustration of a lipid in a coarse grained density field. The highlighted red particle G at position $\mathbf{r}_{\mathrm{G}}$ is interacting with the extrapolated coarse grained density of the sourrounding grid points $\tilde{\rho}_{\tilde{\mathrm{X}}}$ at position $\mathbf{r}_{\mathrm{G}}$. The forces for these interaction are given by $F_{\mathrm{G}\tilde{\mathrm{X}}}(\mathbf{r}_{\mathrm{G}})$ and are indicated by the arrows.

The force acting on the bead G of a molecule is then given by the sum of the contributing CG forces

$$F_{\mathrm{G}}(\mathbf{r}_{\mathrm{G}}) = \sum_{\tilde{\mathrm{X}}} F_{\mathrm{C}\tilde{\mathrm{X}}}. \tag{2.29}$$

The contribution $F_{\mathrm{G}\tilde{\mathrm{C}}}$ which is highlighted in Figure 2.6 is given by

$$F_{\mathrm{G}\tilde{\mathrm{C}}}(\mathbf{r}_{\mathrm{G}}) = -k_B T \left(\chi_{\mathrm{G}\tilde{\mathrm{C}}} \frac{\partial \tilde{\rho}_{\tilde{\mathrm{C}}}(\mathbf{r}_{\mathrm{G}})}{\partial \mathbf{r}_{\mathrm{G}}} \right) - \frac{\partial U_{\tilde{\mathrm{C}}}(\mathbf{r}_{\mathrm{G}})}{\partial \mathbf{r}_{\mathrm{G}}} \tag{2.30}$$

where the first term describes the "soft" long-range interactions and second term the "hard" short-range interactions. $\tilde{\rho}_{\tilde{\mathrm{C}}}(\mathbf{r}_{\mathrm{G}})$ is the extrapolated density of point $\tilde{\mathrm{C}}$ at position $\mathbf{r}_{\mathrm{G}}$. The term for the long-range interactions has its origin in the theory of polymer-solvent interactions. [26]
The mean field parameter χ_{YX} can be calculated following the Flory-Huggins approach with the result [27]

$$\chi_{\mathrm{XY}} = \frac{z_{\mathrm{CN}}}{k_{\mathrm{B}} T} \left[\frac{-2\varepsilon_{\mathrm{XY}} + \varepsilon_{\mathrm{XX}} + \varepsilon_{\mathrm{YY}}}{2} \right] \tag{2.31}$$

where $\varepsilon_{\mathrm{XY}}$ is the Lennard-Jones ε parameter for the corresponding particle-particle interactions and z_{CN} the coordination number, which for a simple cubic three-dimensional lattice is given as $z_{\mathrm{CN}} = 6$. In this work, these parameters were systematically optimized to reproduce the desired properties.
The short-range interactions can be calculated in two different ways. One method is using the compressibility κ to describe the short-range interactions between particle and field. The short-range term is then given by

$$\frac{\partial U_{\tilde{\mathrm{C}}}(\mathbf{r}_{\mathrm{G}})}{\partial \mathbf{r}_{\mathrm{G}}} = \frac{1}{\kappa} \left(\frac{\partial \tilde{\rho}_{\tilde{\mathrm{C}}}(\mathbf{r}_{\mathrm{G}})}{\partial \mathbf{r}_{\mathrm{G}}} \right) \tag{2.32}$$

where the compressibility is to be chosen sufficiently small ($\kappa \approx 0.1\,\mathrm{Pa}^{-1}$). In this way, the intermolecular interaction is replaced completely by an evaluation of the forces between the particle and the field. This approach is therefore called *particle-field* (PF) method.
Another way to calculate the short-range interactions is to introduce particle-particle interactions. Here, a Lennard-Jones potential is used up to a certain cut-off r_{cut}

$$\frac{\partial U_{\tilde{\mathrm{C}}}(\mathbf{r}_{\mathrm{G}})}{\partial \mathbf{r}_{\mathrm{G}}} = \frac{\partial U^{r_{\mathrm{cut}}}_{\mathrm{LJ,GC}}(\mathbf{r}_{\mathrm{G}})}{\partial \mathbf{r}_{\mathrm{G}}}. \tag{2.33}$$

For r_{cut} generally a value near the minimum $r_m = \sqrt[6]{2}\sigma$ is chosen (see also Figure 2.2). Thus, the soft long-range interactions are treated by the field but the short-range interactions are described by particle-particle interaction. Therefore this approach is called *particle-particle particle-field* (PPPF) approach. [21, 25]

2.1.5. Potential of mean force

The energy landscape of a stable system has one global minimum but can have a very complex structure with multiple local minima separated by barriers of various heights. A reduced description of the energy landscape is given by the *potential of mean force* (PMF). It describes the potential along a specific coordinate. Because PMFs are often used to describe reactions or transitions between different potential wells, the relevant coordinate is called *reaction coordinate*. PMFs are also often used to describe the energy landscape of folding pathways in proteins and other biomolecules. [28, 29] The advantage of an PMF is that it is easier to interpret than a multidimensional potential energy surface. It is defined by

$$U_{\mathrm{PMF}}(q) = -k_{\mathrm{B}} T \ln \left[c \int d\mathbf{r}\, \exp(-\beta U(\mathbf{r}) \delta(q(\mathbf{r}) - q) \right] \tag{2.34}$$

where $q(\mathbf{r})$ is the reaction coordinate and a function of $\mathbf{r}$ but q is the value of the reaction coordinate. c is a constant which derives from integrating the momenta. An illustration of a PMF with two wells is given in Figure 2.7. This could be the PMF of a chemical reaction with A being the reactant and B being the product. Another example could be the closed/folded (C) and the open/unfolded state (O) of a complex molecule.

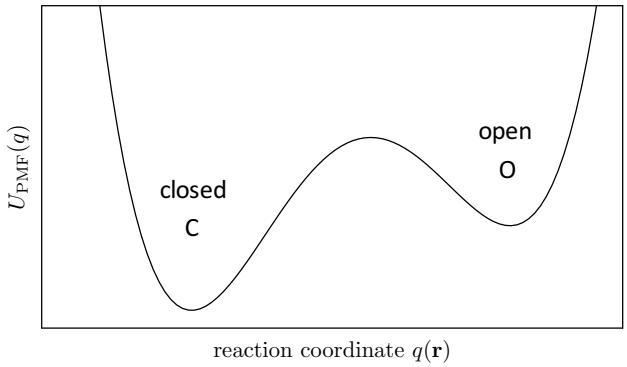

Figure 2.7.: Potential of mean force (PMF) along the reaction coordinate $q(\mathbf{r})$.

One way of computing the PMF is the method of thermodynamic integration. [30] Values for the derivatives of the PMF at given configurations can be obtained by performing constraint equilibrium simulations. The constraint force $F_c(q')$ is defined as the force required to keep the system at a given value of q'. By performing a sufficient number of such simulations along the desired reaction coordinate, the PMF can be obtained from numerical integration by

$$U_{\mathrm{PMF}}(q) = -\int_0^q \left[\left\langle F_c(q')\right\rangle + \frac{2k_{\mathrm{B}}T}{q'}\right] dq' \tag{2.35}$$

with $\langle F_c(q')\rangle$ the average of the constraint force. The second term in eq. (2.35), $\frac{2k_{\mathrm{B}}T}{q'}$, is correcting the entropic contribution to $\langle F_c(q')\rangle$. In this work, the PMF for a molecule in a FPMD simulation was obtained using this method. [30, 31]

2.1.6. Modeling of stochastic processes

Stochastic processes can be viewed as the time-evolution of certain random variables and play an important role in physics and chemistry. In this work, the dynamics of a model systems moving in a double well potential will be modeled as a stochastic process. In particular, it is assumed that the reaction coordinate, i.e., the extension of the molecule considered, is a random variable evolving under the influence of the deterministic forces excerted by the potential and an external force and additionally by a stochastic force representing the coupling to the external degrees of freedom that serve as a heat bath.

Modeling of rupture events

In Figure 2.8 (a) a double well potential with the wells C and O is shown. The minimum of well C is located at q_{C} and the one of O at q_{O}. These minima correspond to stable configurations. Such a potential could for example be the PMF of a rupture event, C being the closed, more

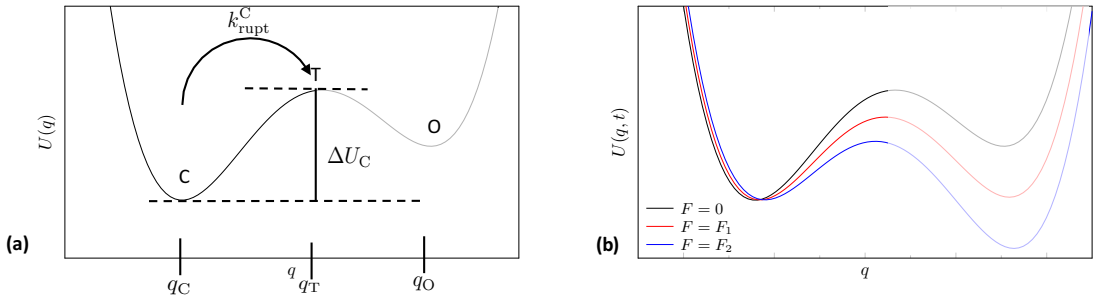

Figure 2.8.: a) Double well potential $U(q)$ with the wells C and O. The minimum of well C is located at q_{C} and the one of well O at q_{O}. C is the more stable state and O another possible, but less stable state. The transition state is marked by T and at position q_{T}. The arrow shows escape from well C with its rate $k^{\mathrm{C}}_{\mathrm{rupt}}$. b) This graph shows the influence of an external force F on the potential and the height of the barrier $\Delta U_{\mathrm{C}}(F) = \Delta U_{\mathrm{C}} - F q_{\mathrm{TC}}$, $F_1 < F_2$. The external potential tilts the energy landscape.

stable state and O the open state. The transition state T is at the maximum of the potential at position q_{T}.
A simple model of a rupture event is the escape from a free energy well. In Figure 2.8 (a) this is shown for for the escape from well C with rate $k^{\mathrm{C}}_{\mathrm{rupt}}$ for the transition C $\rightarrow$ T. For such a simple model, the rate can be calculated with the Arrhenius equation which also expresses the relationship between rate and energy

$$k^{\mathrm{C}}_{\mathrm{rupt}} = k^{\mathrm{C},0}_{\mathrm{rupt}} \exp(-\beta \Delta U_{\mathrm{C}}) \tag{2.36}$$

where $\Delta U_{\mathrm{C}} = U(q_{\mathrm{T}}) - U(q_{\mathrm{C}})$ is the activation energy or height of the barrier. $k^{\mathrm{C},0}_{\mathrm{rupt}}$ is a prefactor and $\beta^{-1} = k_B T$ where k_B is the Boltzmann constant. The rate is therefore dominated by the height of the barrier ΔU_{C}. For a simple system as shown here, the rates are not time-dependent and the temporal evolution of the system can be described by the rate equation

$$\dot{p}^{\mathrm{C}}_{\mathrm{rupt}}(t) = k^{\mathrm{C}}_{\mathrm{rupt}} p^{\mathrm{C}}_{\mathrm{rupt}}(t) \quad \text{with} \quad \dot{p}^{\mathrm{C}}_{\mathrm{rupt}}(t) = \frac{\partial p^{\mathrm{C}}_{\mathrm{rupt}}(t)}{\partial t} \tag{2.37}$$

where $p^{\mathrm{C}}_{\mathrm{rupt}}(t)$ is the population in state C as function of time. To calculate the population $p^{\mathrm{C}}_{\mathrm{rupt}}(t)$, the latter equation is integrated yielding

$$p^{\mathrm{C}}_{\mathrm{rupt}}(t) = \exp\left(-k^{\mathrm{C}}_{\mathrm{rupt}} t\right). \tag{2.38}$$

Another interesting quantity is the waiting time distribution $\Phi^{\mathrm{C}}_{\mathrm{rupt}}(t)$ which is also-called probability density function. $\Phi^{\mathrm{C}}_{\mathrm{rupt}}(t)$ is calculated by $\Phi^{\mathrm{C}}_{\mathrm{rupt}}(t) = -\frac{d}{dt} p^{\mathrm{C}}_{\mathrm{rupt}}(t)$ and is therefore given by

$$\Phi^{\mathrm{C}}_{\mathrm{rupt}}(t) = k^{\mathrm{C}}_{\mathrm{rupt}} p^{\mathrm{C}}_{\mathrm{rupt}}(t) \tag{2.39}$$

The mean of the waiting time $\langle \tau^{\mathrm{C}}_{\mathrm{rupt}} \rangle$ is given by the first moment of the waiting time distribution

$$\langle \tau^{\mathrm{C}}_{\mathrm{rupt}} \rangle = \int_0^\infty dt\, \Phi^{\mathrm{C}}_{\mathrm{rupt}}(t)\, t = (k^{\mathrm{C}}_{\mathrm{rupt}})^{-1} \tag{2.40}$$

and is therefore the inverse of the rate $k^{\mathrm{C}}_{\mathrm{rupt}}$.

Influence of an external force

In this section, the impact of an external potential on the energy landscape will be discussed. The simple model of the escape from a free energy well is taken as a starting point. The influence of a very simple external potential $U_{\text{ext}}(q, F) = -Fq$ can be described by

$$U(q, F) = U(q, 0) + U_{\text{ext}}(q, F) = U(q, 0) - Fq \tag{2.41}$$

which is also illustrated in Figure 2.8 (b). The protocol used for applying a time-independent force to a system is called *constant force* protocol. The external potential tilts the energy landscape and lowers the barrier ΔU_{C}. A closer look at the position q_{C}, q_{T} and q_{O} shows that these positions in general are shifting under the influence of an external force. The impact of this simple external potential will be discussed with help of the *Bell model*. [32] In this model, the positions of q_{C} and q_{T} are independent of the external force. With this assumption, the height of the barrier $\Delta U_{\text{C}}(F)$ under the influence of an external force is given by $\Delta U_{\text{C}}(F) = \Delta U_{\text{C}} - Fq_{\text{TC}}$ where $q_{\text{XY}} = q_{\text{X}} - q_{\text{Y}}$. With (2.36), the force-dependent transition rate can be expressed as

$$k^{\text{C}}_{\text{rupt}}(F) = k^{\text{C,0}}_{\text{rupt}} \exp(-\beta(\Delta U_{\text{C}} - Fq_{\text{TC}})) \tag{2.42}$$

where $k^{\text{C,0}}_{\text{rupt}}$ is the transition rate in absence of an external force. The barrier vanishes at the critical force F_{crit}, given by $F_{\text{crit}} = \frac{\Delta U_{\text{C}}}{q_{TC}}$. For forces $F > F_{\text{crit}}$, the barrier is no longer present in the system and the transition proceeds as a *down hill* process. In such a case, the transition is strictly dominated by diffusion.
Besides using a constant force, it is also possible to use a time-dependent force $F(t)$. This is done in the *force ramp* protocol. Here, the focus is on a time dependent increase in the force which has its origin in a harmonic potential. In this case the force $F(t)$ is given by

$$F(q, t) = -K(q - Vt) \tag{2.43}$$

where K is the force constant of the underlying harmonic potential and V is the velocity. It simulates an experiment where a pulling device with force constant K is attached to a molecule and then moved with velocity V. The time-dependent external potential is then $U_{\text{ext}}(q, t) = \frac{1}{2}K(q-Vt)^2$ and the change in barrier height is given by $\Delta U_{\text{ext}}(q_{TC}, t) = -KVq_{TC}t + \frac{1}{2}K(q^2_{\text{T}} - q^2_{\text{C}})$. For small values of K, the second term $\frac{1}{2}K(q^2_{\text{T}} - q^2_{\text{C}})$ can be neglected. This approximation is called the *soft spring approximation*. Here, the barrier height is only dependent on the distance to the barrier $q_{TC} = q_{\text{T}} - q_{\text{C}}$ and the *loading rate* $\mu = KV$. The transition rate $k^{\text{C}}_{\text{rupt}}$ is a function of time and is given by

$$k^{\text{C}}_{\text{rupt}}(t) = k^{\text{C,0}}_{\text{rupt}} \exp(-\beta(\Delta U_{\text{C}} - \mu q_{\text{TC}} t)). \tag{2.44}$$

In force ramp experiments, the force $f = \mu t$ at which the rupture event takes place is much more interesting than the time. The rupture force distribution is then given as

$$\Phi^{\text{C}}_{\text{rupt}}(f) = \frac{k^{\text{C}}_{\text{rupt}}(f)}{\mu} \exp\left(\frac{1}{\beta\mu q_{\text{TC}}}\left[k^{\text{C,0}}_{\text{rupt}} - k^{\text{C}}_{\text{rupt}}(f)\right]\right). \tag{2.45}$$

The maximum of the rupture force distribution as a function of loading rate μ can be calculated by

$$f_{\max}(\mu) = \frac{1}{\beta q_{\text{TC}}} \ln\left(\frac{\beta\mu q_{\text{TC}}}{k^{\text{C,0}}_{\text{rupt}}}\right). \tag{2.46}$$

This so-called force spectrum is proportional to the logarithm of the loading rate. Comparisons of experimental results and results from simulations show that eq. (2.46) is no longer valid for larger loading rates. An illustration of this behavior can be found in Figure 2.9. Because of computational limitations it is not possible to simulate at the same time scales as in experiments. In fact, the velocities in simulations are up to six orders of magnitude larger than those typically used in the experiments.

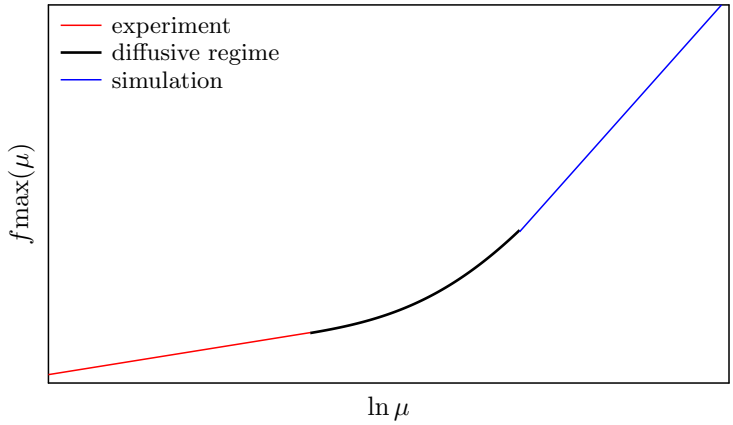

Figure 2.9.: Illustration of a force spectrum $f_{\max}$ versus $\ln \mu$. For the thermally acivated regime at smaller loading rates (red line), $f_{\max}(\mu) < f_{\text{crit}}$, the behavior is according to Bell's model. For larger loading rates (blue line), $f_{\max} \gg f_{\text{crit}}$, the slope of the curve is much larger and Bell's model not longer valid. The diffusive regime, $f_{\max} \geq f_{\text{crit}}$, is marked in black.

The different behavior of $f_{\max}$ for small and large loading rates can be explained by the following: For small loading rates, the energy landscape is tilted but the barrier is still present at the rupture event. In this way the transition is thermally activated like it is assumed in eq. (2.44). This regime is also-called *thermally activated regime* and is marked in Figure 2.9 by a red line ($f_{\max} < f_{\text{crit}}$). For the other regime, marked blue in the illustration, the undisturbed potential is overwhelmed by the external potential and the barrier vanishes before the rupture event could take place. This means, that $f_{\max} \gg f_{\text{crit}}$. This regime is called *drift regime*. [33] In this work, the crossover from the activated to the drift regime is thoroughly investigated for a model system. This crossover regime, $f_{\max} \geq f_{\text{crit}}$, is also-called the *diffusive regime* and marked by the black line.

Mean first passage times The discussed Bell model for the calculation of the rupture rate $k_{\text{rupt}}^{\text{C}}$ is a purely phenomenological model. With the simple Bell model it is easy to calculate transition rates analytically but for more complicated energy landscapes, other more complex methods are used. In this work, rates were calculated as *mean first passage times* (MFPT). [34]
The escape from a potential well can also be described by using the Fokker-Planck equation (Smoluchowski equation). [34] The Fokker-Planck equation describes the time evolution of the probability density function of the position q of a particle under the influence of drag forces and

random forces, as in Brownian motion. It is given by

$$\dot{p}(q,t) = D\left[\frac{\partial}{\partial q}e^{-\beta U(q,t)}\frac{\partial}{\partial q}e^{\beta U(q,t)}\right]p(q,t) \tag{2.47}$$

where $D = \gamma T$, γ is the damping constant and $U(q,t)$ is a potential of any shape. From the Fokker-Plank equation, one can derive expressions for the transition rates from C to T as mean first passage times [34]:

$$\tau^{\mathrm{C}}_{\mathrm{rupt}}(t) = \frac{1}{D}\int_{q_{\mathrm{C}}(t)}^{q_{\mathrm{T}}(t)} dq\, e^{\beta U(q,t)}\int_{-\infty}^{q} dq'\, e^{-\beta U(q',t)}. \tag{2.48}$$

and the rupture rate is then given by $k^{\mathrm{C}}_{\mathrm{rupt}}(t) = (\tau^{\mathrm{C}}_{\mathrm{rupt}}(t))^{-1}$. Note, that the position of $q_{\mathrm{C}}(t)$ and $q_{\mathrm{T}}(t)$ are also time-dependent unlike in the Bell model. The waiting times as given in eq. (2.48) can only be calculated as long as q_{C} and q_{T} are clearly defined. For a force-dependent potential $U(q,t)$ as shown in Figure 2.8 (b), the barrier vanishes at the critical force f_{crit} and the equation for $\tau^{\mathrm{C}}_{\mathrm{rupt}}(t)$ can not longer be solved. Likewise to the here shown mean first passage time $\tau^{\mathrm{C}}_{\mathrm{rupt}}$, any transition from any starting position $q_{\mathrm{X}}(t)$ to any end position $q_{\mathrm{Y}}(t)$ can be calculated, e.g. the passage time $\tau^{\mathrm{O}}_{\mathrm{rupt}}$ for the transition C $\rightarrow$ O.
As an example for $U(q,t)$ one can choose for instance a harmonic cusp surface [35] $U(q) = \Delta U_{\mathrm{C}}\left(\frac{q}{q_{\mathrm{TC}}}\right)^2$ for $q < q_{\mathrm{TC}}$ and $-\infty$ for $q \geq q_{\mathrm{TC}}$. For a sufficiently high barrier $\Delta U_{\mathrm{C}} \gg \beta^{-1}$ one can use the Kramers theory [34] which is a simplified version of eq. (2.48). The rates under the presence of a force F are then calculated by [36]

$$k^{\mathrm{C}}_{\mathrm{rupt}}(F) = k^{\mathrm{C},0}_{\mathrm{rupt}}\left(1-\frac{F}{F_{\mathrm{crit}}}\right)e^{\beta\Delta U_{\mathrm{C}}\left(1-\left(1-\frac{F}{F_{\mathrm{crit}}}\right)^2\right)} \quad \text{with} \quad F_{\mathrm{crit}} = \frac{\Delta U_{\mathrm{C}}}{q_{\mathrm{TC}}}. \tag{2.49}$$

The obtained result is very similar to the result obtained for the phenomenological Bell model (cf. eq. (2.42)).
In order to extract parameters like the bare rate $k^{\mathrm{C},0}_{\mathrm{rupt}}$, barrier height ΔU_{C} and effective distance from the barrier q_{TC}, eq. (2.49) is fitted to rates obtained from experiments or simulations. Such a fit is only meaningful for experiments/simulations in the regime for activated dynamics and forces smaller than the critical force F_{crit}. To inspect rupture events in the drift regime, other methods have to be used, e.g. stochastic simulations like kinetic Monte Carlo.

Kinetic Monte Carlo Stochastic simulations like *kinetic Monte Carlo* (KMC) [37] are powerful methods to investigate rupture events. Unlike in the models discussed above, KMC is not only limited to the activated regime but also simulations within the drift regime are possible. In this work, the Gillespie algorithm [38, 39] is used for solving the Master equation with Monte Carlo methods.
Here, a finite-difference version of the Fokker-Planck equation (2.47) in its Master equation form is solved. For this the continuous coordinate q is divided in a grid of points $\{q_i\}$ with spacing $\Delta q = q_{i+1} - q_i$ (see Figure 2.10) resulting in

$$\frac{\partial p(q_i,t)}{\partial t}\Delta q = p(q_{i-1},t)k_{i,i-1}(t) + p(q_{i+1},t)k_{i,i+1}(t) - p(q_i,t)\left[k_{i,i-1}(t) + k_{i,i+1}(t)\right] \tag{2.50}$$

and the transition rates are given by [40]

$$k_{i,i\pm1}(t) = \frac{D}{(\Delta q)^2}\exp\left(-\frac{1}{2}\beta\Delta U_{\pm}(q,t)\right) \quad \text{with} \quad \begin{cases}\Delta U_{+}(t) & = U(q_{i+1},t) - U(q_i,t)\\ \Delta U_{-}(t) & = U(q_i,t) - U(q_{i-1},t)\end{cases} \tag{2.51}$$

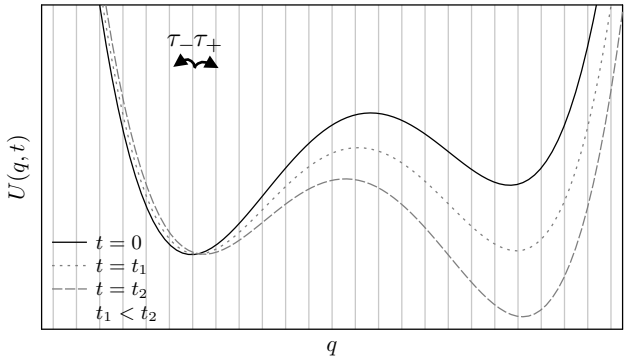

Figure 2.10.: Scheme for KMC using the 'next reaction method' of the Gillespie algorithm. The continious coordinate q is diveded in a grid of points $\{q_i\}$ with spacing Δq. For the initial condition t_0 the system is in the minima of well C. Random waiting times $\tau_\pm$ are calculated and then the system is propagated into the direction with the smaller waiting time.

Next, the waiting time for each step has to be determined. This is done by using the 'next reaction method' of the Gillespie algorithm. Here, waiting times τ are drawn from the corresponding probability density function and then the system is propagated into the direction with the shorter waiting time. To determine the waiting time τ the cumulative waiting time distribution is used

$$C(t) = \int_{t_0}^{t} \Phi(t')dt' = p(t_0) - p(t) = 1 - \exp\left(-\int_{t_0}^{t} k(t')\,dt'\right) \tag{2.52}$$

which is the probability that at least one transition takes place in the interval $[t_0, t]$. Eq. (2.52) is obtained using $\dot{\Phi}(t) = -\dot{p}(t)$, $p(t_0) = 1$ and $p(t) = \exp\left(-\int_{t_0}^{t} k(t')\,dt'\right)$. The inversion of this function gives the time $t = C^{-1}(p)$ after which the transition has occurred with probability p. The waiting time between two subsequent transition is then given by

$$\tau = t - t_0 = C^{-1}(p) - t_0. \tag{2.53}$$

For the probability p a random number ξ in the interval $[0, 1]$ is chosen. With ξ and $\xi' = 1 - \xi$ having the same distribution over the same interval as ξ, eq. (2.52) can be rewritten to

$$\xi' = \exp\left(-\int_{t_0}^{t} k(t')\,dt'\right). \tag{2.54}$$

The latter equation can be easily solved for a time-independent rate k. The waiting time $\tau = t - t_0$ is then given by

$$\tau = -\frac{\ln \xi}{k}. \tag{2.55}$$

For a time dependent rate as given in eq. (2.51) the waiting times are calculated by

$$\tau_\pm(q_i, t_0) = \frac{1}{\pm b_q \mu} \ln\left(1 - \frac{\pm b_q \mu}{k_\pm^0(q_i) e^{\pm b_q t_0 \mu}} \ln \xi_\pm\right) \quad \text{with} \quad b_q = \frac{\beta \Delta q}{2}. \tag{2.56}$$

The rate $k_\pm^0(q_i)$ is the time-independent but q-dependent rate. Two random numbers, ξ_+ and ξ_-, are generated and the shorter waiting time is used to propagate the system (see Figure 2.10). In this way, a stochastic trajectory is created which is not limited to the activated regime.

3. Pulling parameter dependence in reversible force probe molecular dynamics simulations

Self-organization is a key feature of biological systems and has given rise to the formation of complex systems like cells and even whole organisms. Even three-dimensional structures of biomolecules on their own, such as the fold of proteins and the RNA structure, are impressive examples. Undeniably, these biomolecules with their specific structure and their conformational changes are essential to life. Understanding these self-organization processes in detail requires a detailed knowledge on how the involved interaction such as hydrogen bonds, forces between charges, van der Waals interaction, and so forth, lead to such defined structures. [41]
For a long time, binding and folding energies could only be measured by calorimetry experiments. From such experiments one can only obtain ensemble-averaged information and not information concerning details of the energy landscape that determine the three-dimensional structure. In the 1980s, scanning probe techniques were developed and it was now possible to measure forces which stabilize biomolecular structures directly on a single molecule. [41] These techniques were initially developed to image surfaces with atomic resolution. The development of the scanning tunneling microscope (STM) by Gerd Binnig and Heinrich Rohrer in 1982 let to the invention of the atomic force microscope (AFM) by Calvin Quate in 1986. [42] With this new technique it was now possible to measure forces as small as 10^{-18} N and investigate surfaces of insulators on an atomic scale.
In 1994 Ernst Ludwig Florin, Vincent Moy and Hermann Gaub measured the binding forces of single molecules for the first time. [43] As model system they choose biotin and streptavidin because the structures of these molecules are known to atomic detail. A sketch of the setup of the experiment can be found in Figure 3.1.

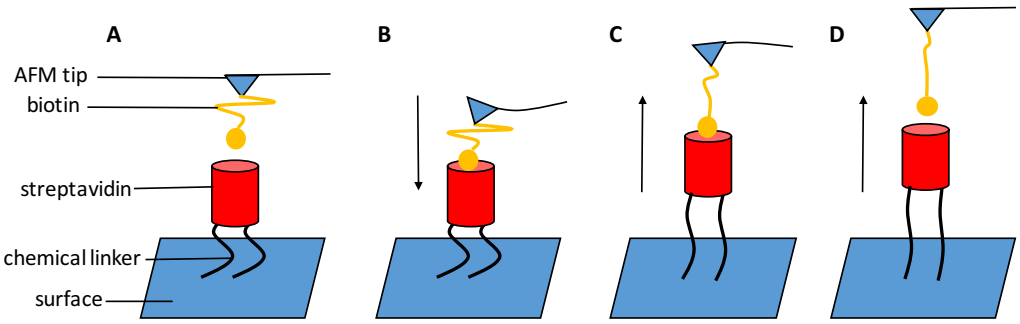

Figure 3.1.: Sketch of the streptavidin-biotin experiment. [43] **A:** Setup of the experiment. **B:** Lowering of the AFM tip, a streptavidin-biotin complex is built. **C:** Retracting the AFM tip. **D:** Rupture event.

Single biotin molecules were coupled covalently to a AFM tip via a chemical linker. A surface was prepared in a similar way and functionalized with streptavidin molecules (**A**). By slowly lowering the tip of the AFM a few streptavidin-biotin complexes are built (**B**). The tip was then slowly

retracted (**C**) and the rupture force measured (**D**). This procedure was repeated several hundred times and resulted in a distribution of rupture forces. The binding force of the streptavidin-biotin pair was determined to be 160 pN per binding pair. This experiment showed furthermore that it is possible to measure the binding force of a single ligand-receptor complex. Despite this big improvement in experimental technique, little is known about the binding and unbinding pathway of this complex. In order to reveal this pathway, extended MD simulations were performed and suggested a detailed multiple-pathway mechanism involving several unbinding steps. [44] Like in the experiment, the complex was stretched and the force measured. Such force probe MD (FPMD) simulations are therefore more than just an addition to experiments that probe the force: they continue where experimental techniques fail. The combination of both techniques, FPMD simulation and force spectroscopy, offers therefore a unique way to study fundamental theories of statistical mechanics.

So far, an irreversible process has been discussed but especially reversible processes are important features of biomolecules. Processes like protein transcription and enzyme catalysis would not be possible without reversibly folding RNA and proteins. In 2001 reversible unfolding of single molecules by mechanical force was observed for the first time in an experiment. [45] There, the unfolding and refolding of single RNA molecules were investigated. Such experiments are ideal to study the physics of nanoscopic systems but one problem still persists: the investigated energy landscape is not tunable. In order to understand the physics of reversible bond breakage a more sophisticated system is needed. The requirements for such a system are the following: Firstly, the binding partners should have well-defined non-covalent bonds, e.g., hydrogen bonds. Secondly, the reversibility and therefore the energy landscape should be tunable. Due to the vast improvements in synthetic chemistry, this second requirement can be realized by connecting the binding partners via entangled loops of variable length. [46, 47] Such mechanically interlocked structures, so-called catenanes, are considered to be one of the greatest triumphs of synthetic supramolecular chemistry. [47]

An innovative study of such a sophisticated model was published in 2009 by Janke et. al. [46] The studied system is a mechanically interlocked calix[4]arene dimer. It consists of two nanocapsules which can build a closed state by building 16 hydrogen bonds. The mechanically interlocked structure tunes the energy landscape of the dimer, thus permitting the reversible rupture and rejoin of the nanocapsules. The study comprises of three different parts: firstly, an experimental part. Here, the dimer is stretched using an atomic force microscope. The general procedure is similar to the one shown in Figure 3.1. Secondly, FPMD simulations were performed. Besides reproducing similar rupture forces, also a possible rupture and rejoin pathway is proposed. This again is a great example how simulations complete the understanding of such small systems. Thirdly, stochastic models help to understand the experiment and the FPMD simulations further. It was shown that the system offers the oppertunity to study the energy landscape of a single reaction as a function of molecular design and external force. The studied calix[4]arene is therefore the ideal testbed for modern theories of nonequilibrium statistical mechanics. [46]

Due to its ideal properties, calix[4]arene-catenane systems have been further studied via FPMD simulations. Besides a study focusing on more technical simulation details like the influence of different force fields in ref. [48], also a detailed investigation of the reversible hydrogen bond network dynamics is presented in ref. [49]. In this chapter, a detailed investigation of such a calix[4]arene-catenane which extends on these studies is presented. The system is introduced in section 3.1 and the setup of the performed FPMD simulations is discussed in section 3.2. The overall work is focusing on the dependence of FPMD simulation on the variation of the pulling parameters K, the pulling velocity, and V, the force constant.

Section 3.3 comprises a detailed study of a well-studied calix[4]arene dimer. The structural and

mechanical properties are presented before discussing more complex studies. A new way to understand the behavior of measured forces is presented in section 3.3.2. It extends on Bell's model [32] and characteristic forces can be calculated. In section 3.3.3, the influence of the hydrogen bond network is investigated and a working definition for a transition state is introduced. Furthermore, the kinetic of the studied system is analyzed. Kinetic rates are calculated in section 3.3.4 and expanded with studies of stochastic model in section 3.3.5. There, the crossover from activated to diffusive dynamics is investigated.
Section 3.4 presents structural and mechanical details of different calix[4]arenes as a function of molecular design. The degree of reversibility is investigated and definitions of a closed, intermediate and an open state are given.

3.1. Calix[4]arene-catenane: Discussion of the system

In this work, the well-studied Calix[4]arene-catenane [46, 48, 49] is investigated by force probe molecular dynamics (FPMD) simulations. The typical protocol used for these simulations consists of a linear force ramp, where a part of the molecular construct is pulled away from the remainder with a constant velocity and the force is measured. Calix[4]arene-catenane represent mechanically interlocked structures consisting of two calix[4]arene molecules and will from here on be referred to as the 'calixarene'. The catenane structure is realized by four aliphatic loops of tuneable length, l. Three different variants of this calixarene with different loop lengths l are investigated; corresponding to their loop length, these are termed T14 ($l = 14$ CH_2 units), T17 ($l = 17$ CH_2 units) and T20 ($l = 20$ CH_2 units). The chemical structure, a stick model (T14) and a cartoon of the calixarene are shown in Figure 3.2.

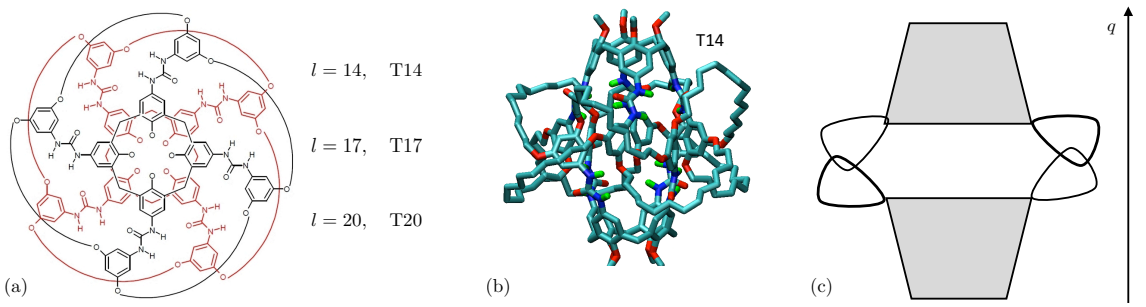

Figure 3.2.: (a) Chemical structure of the Calix[4]arene. The varying loops with different lengths l are indicated in the structure by curves. (b) Stick model of T14. (c) Cartoon of the calixarene. For simplicity, only two of the mechanically interlocked loop pairs are shown. The two calix[4]arene are represented as 'cups'.

Due to the tuneable loop length, it is possible to gain full control over the energy landscape. The calixarene can be stretched along an axis q (see Figure 3.2 (c)). Depending on the distortion along q, the calixarene and all of its variants is stabilized by a hydrogen bond network. There are two different types of hydrogen bonds possible and these are shown in Figure 3.3. For small values of q, the calixarene is stabilized by hydrogen bonds between the urea groups. These bonds of which a maximum number of 16 can be formed will be termed UU bonds. For larger values of q, the system is stabilized by hydrogen bonds between the urea and the ether groups, the UE-bonds. A maximum of 8 of these can be formed.

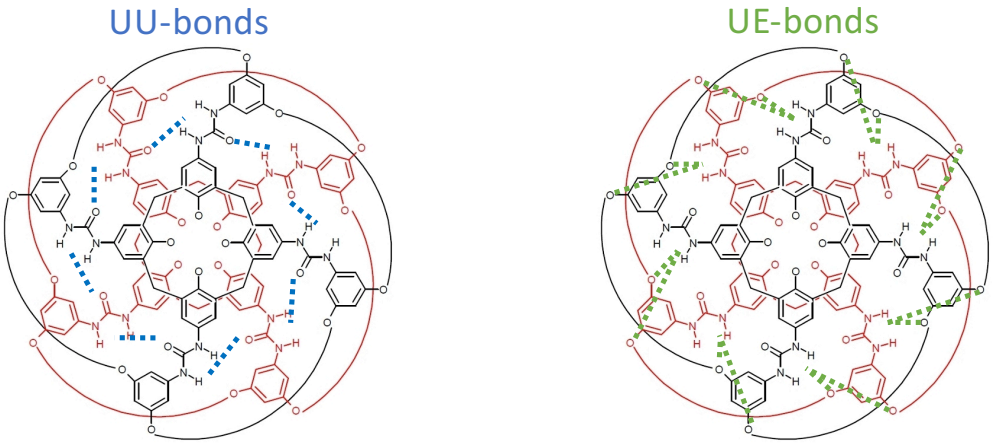

Figure 3.3.: Different possible sets of hydrogen bonds within the Calix[4]arene-catenane. Left: hydrogen bonds between different urea groups, UU-bonds. Right: hydrogen bonds between urea and ether groups, UE-bonds.

With the help of the distance q and the type of hydrogen bonds, one can define different states (closed "C", intermediate "I", and open "O") for the different variants of the calixarene. These are shown in Figure 3.4. The calixarene T14 with the shorter loops can build two different states: a closed state C at around $q = 1.5\,\text{nm}$, which is stabilized by UU-bonds, and an open state O at around 2.0 nm. State O is stabilized by UE-bonds. Calixarenes T17 and T20 are less restricted due to the increased loop lengths. The state at around 2.0 nm is an intermediate state, stabilized by UE-bonds, and the open state is located around $q \approx 2.3\,\text{nm}$ and is not stabilized by any hydrogen bonds.

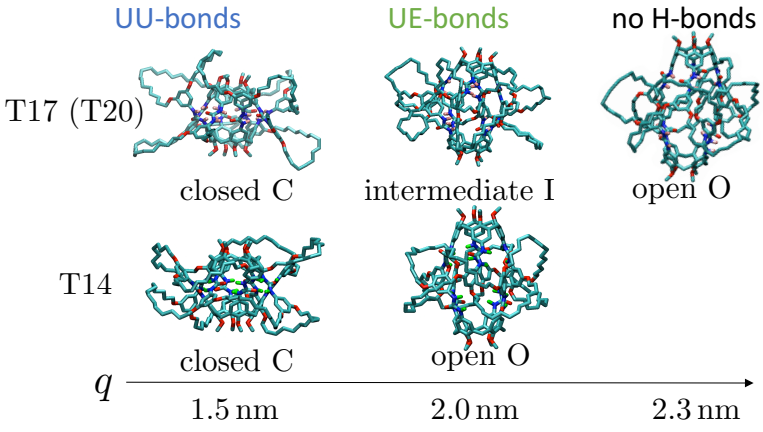

Figure 3.4.: Different possible states for the calixarene.

3.2. Setup of FPMD simulations

All of the FPMD simulations were performed using the GROMACS 4.0.7 program package [50] employing the OPLS-AA force field [51,52]. Further computational details can be found in App. A.2. All simulations were performed using mesitylene as solvent, cf. [46]. The number of atoms, molecules and the initial box sizes are collected in Table 3.1.

Table 3.1.: Initial box sizes, number of atoms and molecules for the conducted FPMD simulations of T14, T17 and T20. The total number of atoms is calculated by the product of number of molecules and the number of atoms.

	T14			**T17**			**T20**		
	mol	atoms	total	mol	atoms	total	mol	atoms	total
Mesitylene	435	21	9135	542	21	11382	859	21	18039
Calixarene	1	600	600	1	672	672	1	744	744
System	436		9735	543		12054	860		18783
initial box size:	$(5.4 \times 4.4 \times 4.4)\,\mathrm{nm}^3$			$(6.0 \times 4.6 \times 4.6)\,\mathrm{nm}^3$			$(7.2 \times 5.3 \times 5.3)\,\mathrm{nm}^3$		

The production runs were prepared as follows: First, an energy minimization for all used molecules was performed followed by a solvation procedure. On the solvated system, an energy minimization was performed again. The minimized solvated system was then equilibrated at 300 K for about 500 ps using a velocity rescaling thermostat with a time constant of 0.1 ps. [53] The system was then coupled to a barostat (Parrinello-Rahman barostat [54] with time constant 2 ps and compressibility of $8.26 \cdot 10^{-5}\,\mathrm{bar}^{-1}$). All simulation were performed in the NPT-ensemble at a pressure of 1 bar.
In Figure 3.5, a stick model of a calixarene and a sketch of the pulling device are shown. For the FPMD simulations the center of mass of the four methoxy-carbon atoms at the narrow rim of one calixarene was fixed (reference group) and a time-dependent harmonic pulling potential was applied to the center of mass of the methoxy-carbon atoms of the other calixarene (pulled group). The distance between the pulled and the reference group is denoted the end-to-end distance, q, and is a function of the simulation time t, $q(t)$. The t-dependent external harmonic potential is given by

$$U_{\mathrm{pull}}(t) = \frac{K}{2}(q_0(t) - Vt)^2 \tag{3.1}$$

where $q_0(t) = q(t) - q(0)$ is the displacement of the pulled group from its original position, V is the pulling velocity and K is the force constant. By moving in the direction of the black arrow in Figure 3.5, the end-to-end distance is increased and the pulled and the reference groups are pulled apart. This mode of pulling will therefore be denoted the *pull mode*. The displacement of the origin of the harmonic pulling potential is denoted as the extension, $x = Vt$, and is thus only dependent on the pulling speed V. The force acting on the pulled group is given by

$$F(t) = K(Vt - q_0(t)). \tag{3.2}$$

By inverting the velocity V, the end-to-end distance is decreased. In Figure 3.5, this is shown by the red arrow pointing in the opposite direction with respect to the arrow for the pull-mode. This mode is denoted the *relax mode*.
The parameters K and V are pulling parameters and their product is the so-called loading rate, $\mu = KV$. In this work, the influence of the pulling parameters are investigated. For this purpose, different combinations of K and V are tested.

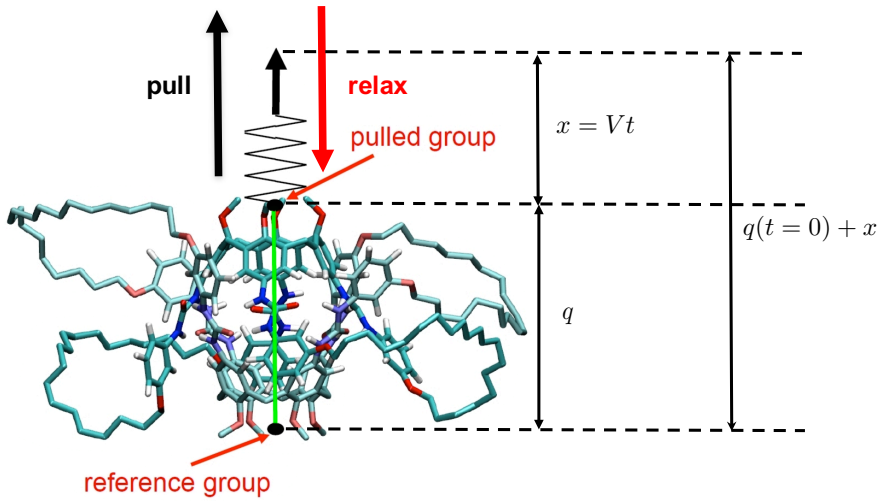

Figure 3.5.: Simple stickmodel of a calixarene and schematic representation of the force probe simulation. The center of mass of each of the four methoxy carbons (black dots) refers to the pulled and the reference group. The distance between these groups is the end-to-end distance q and is a function of time t. Within the FPMD simulation, an external potential is attached to the molecule. This potential acts on the pulled group, while the reference is at a fixed position.

3.3. Calixarene T14

In this section, the results for the calixarene T14 system are discussed. In order to investigate the dependence of characteristic forces on the pulling parameters, several combinations of different values of K and V for loading rates μ ranging from $0.08505-83.05\,\mathrm{N/s}$ were tested. These different combinations are collected in Table 3.2. For each combination of K and V, 100 simulation for the pull mode and 100 simulations for the relax mode were performed. The parameters are shown in Table 3.2.

$\mu = 83.05\,\mathrm{N/s}$		$\mu = 8.305\,\mathrm{N/s}$		$\mu = 0.8305\,\mathrm{N/s}$		$\mu = 0.08305\,\mathrm{N/s}$	
K[N/m]	V[m/s]	K[N/m]	V[m/s]	K[N/m]	V[m/s]	K[N/m]	V[m/s]
0.2048	400						
0.4153	200	0.4153	20	0.4153	2	0.4153	0.2
0.8305	100	0.8305	10	0.8305	1	0.8305	0.1
1.661	50	1.661	5	1.661	0.5	1.661	0.05
3.322	25	3.322	2.5	3.322	0.25		
6.644	12.5	6.644	1.25				
13.288	6.25						
26.576	3.125						

Table 3.2.: Combinations of K and V used in the simulations. For each set, 100 simulations (pull and relax) were performed.

3.3.1. Discussion of a single FPMD simulation

Now the results of a single FPMD simulations, pull and relax mode, of a calixarene T14 are discussed. For this simulation, the parameters $K = 0.8305\,\mathrm{N/m}$ and $V = 1\,\mathrm{m/s}$ ($\mu = KV = 0.8305\,\mathrm{N/s}$) were used. For simulations with different parameters, qualitatively comparable results are found.

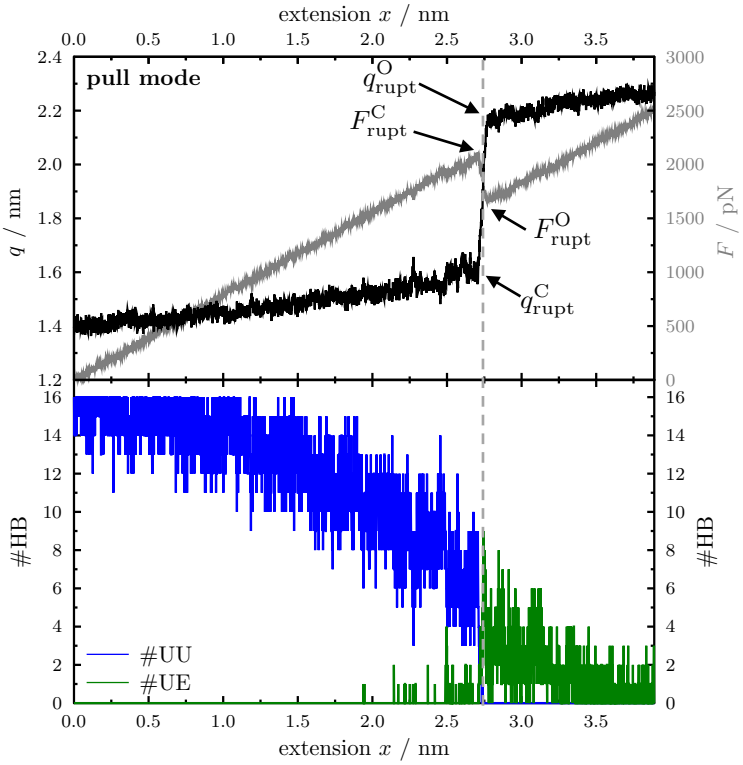

Figure 3.6.: Pull mode: All properties are plotted as a function of the extension $x = Vt$. The pulling parameters are $K = 0.8305\,\mathrm{N/m}$ and $V = 1\,\mathrm{m/s}$, resulting in a loading rate of $\mu = 0.8305\,\mathrm{N/s}$. Upper panel: sample RE curve (black) and FE curve (grey). Lower panel: Number of hydrogen bonds #HB (#UU and #UE) for the same simulation. The grey dotted line marks the rupture event at $x \approx 2.74\,\mathrm{nm}$.

In Figure 3.6, representative results for a simulation of the pull mode are shown. All results are plotted as functions of the extension x. In the upper panel, the end-to-end distance as a function of the extension is shown in black and the measured force, the so-called force extension (FE) curve, is plotted in grey. The end-to-end distance curve as a function of the extension will from here on be denoted RE (distance extension) curve. In the lower panel, the number of hydrogen bonds (#HB) are plotted. Here, the number of UU bonds (#UU) are plotted in blue and the number of UE bonds (#UE) in green. To determine if a HB exists, a purely geometrical criterion is used:

$$r_{\mathrm{HB}} \leq 0.35\,\mathrm{nm} \qquad \text{and} \qquad \alpha_{\mathrm{HB}} \leq 30\,^{\circ}$$

where the distance between donor D and acceptor A is given by r_{HB} and the angle H-D-A is given by α_{HB} (see also Figure 3.7).

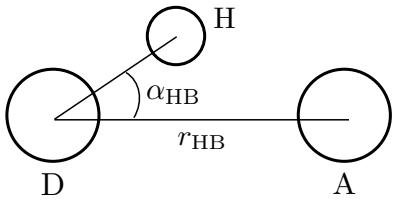

Figure 3.7.: Illustration of the distance r_{HB} and the angle α_{HB} which are used as a criterion for a HB. The criterion used is a purely geometrical criterion: $r_{\mathrm{HB}} \leq 0.35\,\mathrm{nm}$ and $\alpha_{\mathrm{HB}} \leq 30\,^{\circ}$.

The simulation is characterized by a rupture event at $x_{\mathrm{rupt}} \approx 2.74\,\mathrm{nm}$ which marks the transition from the closed state C ($x < x_{\mathrm{rupt}}$) to the open state O ($x > x_{\mathrm{rupt}}$). For $x < x_{\mathrm{rupt}}$, the force is increasing in a linear fashion and the calixarene is stretched starting from $q = 1.41\,\mathrm{nm}$. At the rupture event, the force decreases from $F^{\mathrm{C}}_{\mathrm{rupt}} \approx 2000\,\mathrm{pN}$ to $F^{\mathrm{O}}_{\mathrm{rupt}} \approx 1600\,\mathrm{pN}$. These forces, $F^{\mathrm{C/O}}_{\mathrm{rupt}}$ will be denoted as the rupture forces from now on. $F^{\mathrm{C}}_{\mathrm{rupt}}$ is the higher value and marks the force before the rupture event takes place and the system transitions into the open state O at force $F^{\mathrm{O}}_{\mathrm{rupt}}$. This drop in force is connected to the opening of UU bonds. Around x_{rupt}, the number of UU bonds decreases from around $\#\mathrm{UU} \approx 8$ to $\#\mathrm{UU} \approx 0$ and there is a steep increase in the end-to-end distance from $q^{\mathrm{C}}_{\mathrm{rupt}} \approx 1.5$ to $q^{\mathrm{C}}_{\mathrm{rupt}} \approx 2.2$, which is directly connected to the decrease in the number of UU bonds. Shortly before x_{rupt}, UE bonds are built and the number of these reaches a maximum of 8 shortly after the rupture event (lower panel in Figure 3.6).
As mentioned already, the system is in the closed state C for $x < x_{\mathrm{rupt}}$ in which mainly UU bonds exist. Given that the system shows harmonic behavior because of the linear increase in force, a force $F = K_{\mathrm{mol}} q_0$ is acting on the calixarene, where K_{mol} is the molecular force constant. Using eq. (3.2), $F = K(Vt - q_0) = K(x - q_0)$, and equating the forces, one gets

$$q_0 = \frac{K}{K + K_{\mathrm{mol}}} x. \tag{3.3}$$

From the latter equation, $F = K_{\mathrm{mol}} q_0$ can be rewritten to

$$F = K_{\mathrm{eff}} x \quad \text{with} \quad K_{\mathrm{eff}} = \frac{K K_{\mathrm{mol}}}{K + K_{\mathrm{mol}}}. \tag{3.4}$$

After the rupture event, the calixarene is no longer stabilized by UU bonds but rather by UE bonds. A maximum number of 8 UE bonds are built shortly after the transition and the number of these decays with increasing extension. For $x > x_{\mathrm{rupt}}$, the force and the end-to-end distance are increasing again in a linear fashion.
After reaching a force of $F = 2500\,\mathrm{pN}$, a distance of $q = 2.25\,\mathrm{nm}$ and an extension of $x_{\mathrm{end}} = 3.9\,\mathrm{nm}$, the simulation was stopped and the pulling direction was inverted. The end-to-end distance q, the measured force F and the number of hydrogen bonds are shown in Figure 3.8 as functions of the extension. Note that the extension for the relax mode is calculated by $x = x_{\mathrm{end}} - Vt$. The graph has therefore to be read from right to left.
The relax mode is characterized by a rejoin event at $x_{\mathrm{rejoin}} \approx 0.7\,\mathrm{nm}$. For $x > x_{\mathrm{rejoin}}$, the calixarene is in the open state and for $x < x_{\mathrm{rejoin}}$ in the closed state. Starting from an extension of 3.9 nm, the number of UE-bonds is increasing with decreasing extension until reaching a

maximum number at around $x = 1.5\,\text{nm}$. The number of UE-bonds is then slowly decreasing and at $x = 0.4\,\text{nm}$ no more UE bonds exist. The end-to-end distance q and the force F are decreasing in a linear fashion with decreasing extension. The rejoin event is marked by a sudden increase in force from $F^{\text{O}}_{\text{rejoin}} \approx 250\,\text{pN}$ to $F^{\text{C}}_{\text{rejoin}} \approx 500\,\text{pN}$ and the distance drops from $q^{\text{O}}_{\text{rejoin}} \approx 1.9\,\text{nm}$ to $q^{\text{C}}_{\text{rejoin}} \approx 1.5\,\text{nm}$. These forces will be denoted as the rejoin forces, $F^{\text{C/O}}_{\text{rejoin}}$, and the corresponding distances as $q^{\text{C/O}}_{\text{rejoin}}$. The jump in force and in end-to-end distance is linked to the abruptly increasing number of UU bonds and the transition to the closed state. After the rupture event, the force and the end-to-end distance are decreasing again. The force reaches 0 pN and one has a distance of 1.41 nm at the end of the simulation.

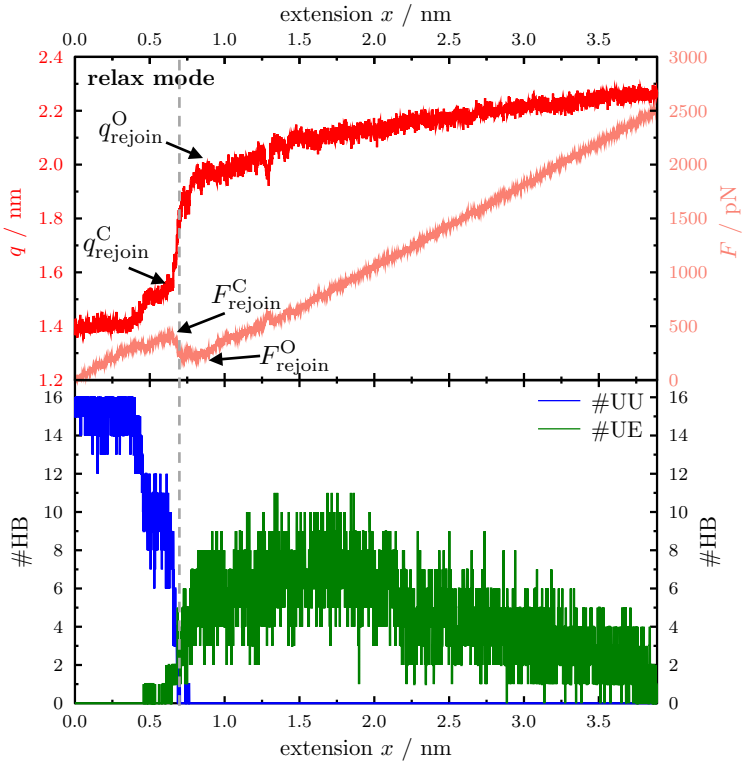

Figure 3.8.: Relax mode: All properties are plotted as a function of the extension $x = x_{\text{end}} - Vt$ and has therefore to be read form right to left. The parameters are the same as in Figure 3.6. Upper panel: sample RE curve (red) and FE curve (light red). Lower panel: Number of hydrogen bonds #HB (#UU and #UE). The grey dotted line marks the transition event at $x = 0.7\,\text{nm}$.

In order to better compare the pull and relax modes, the force and the end-to-end distance are plotted again in Figure 3.9. Outside of the interval $0.7 < x < 2.74\,\text{nm}$, the curves for F and q are almost identical. Here, the curves for the relax mode follow the same path as the curves for the pull mode. Because the two transition events occur at different values of x, the system shows a hysteresis and therefore typical non-equilibrium behavior.
Repeating the same simulation with the identical pulling parameters K and V would lead to

different results since the velocity of all the particles are randomly generated at the beginning of each simulation. The obtained rupture and rejoin events differ for each simulation and are therefore stochastic processes.

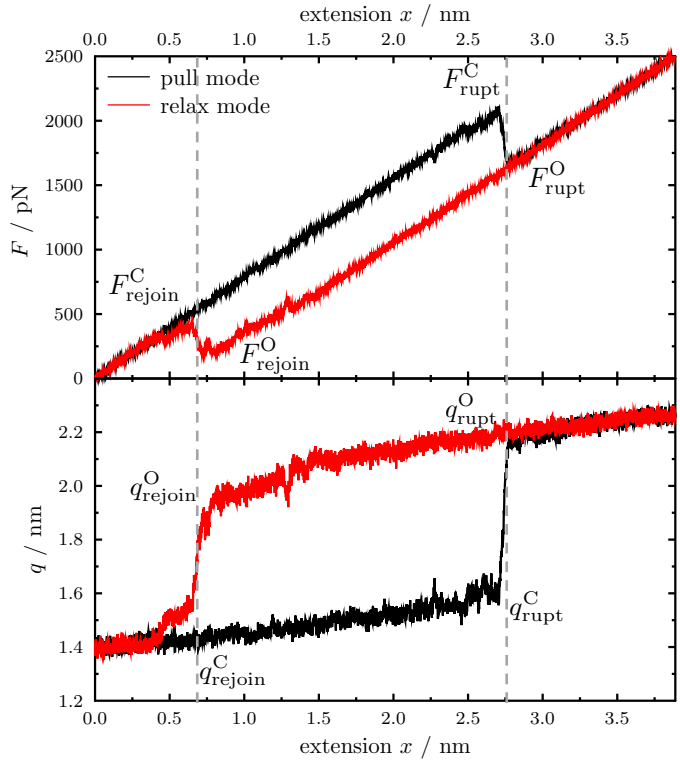

Figure 3.9.: Comparison of the measured force F (upper panel) and end-to-end distance q (lower panel) plotted as functions of the extension. The grey dotted lines mark the transition events: the rupture event at $x = 2.4\,\mathrm{nm}$ and the rejoin event at $x = 0.7\,\mathrm{nm}$.

3.3.2. Analysis of the FE curves

Due to the fact that the rupture and the rejoin events are stochastic processes, the usual analysis of a large number of FE curves conducted with identical external parameters K and V consists in the determination of the rupture and the rejoin force distribution $p(F^{\mathrm{C/O}}_{\mathrm{rupt/rejoin}})$. In Figure 3.10, histograms are shown for both, the pull mode (black and grey) and the relax mode (red and light-red). The distributions of the maximum force, F^{C}, and the minimal force, F^{O}, are individually determined as indicated in the figure. The mean values $\langle F \rangle$ are calculated as the first moment

$$\langle F \rangle = \int_{-\infty}^{+\infty} p(F) F \, dF. \tag{3.5}$$

For a loading rate of $\mu = 0.8305\,\mathrm{N/s}$, this analysis was repeated for each set of parameters K and V. Based on these results, the characteristic forces are plotted against K in Figure 3.11 (a). Here, the dotted lines are obtained by linear regression and are guides to the eye. From this plot,

it is clear that the maximum of the rupture forces (black squares, F^{C}_{rupt}) and the minimum of the rejoin forces (red squares, F^{O}_{rejoin}) show almost no K-dependence and therefore also no velocity dependence. This is different from the behavior of the minimum rupture force (grey triangles, F^{O}_{rupt}) and the maximum rejoin forces (light-red triangles, F^{C}_{rejoin}).

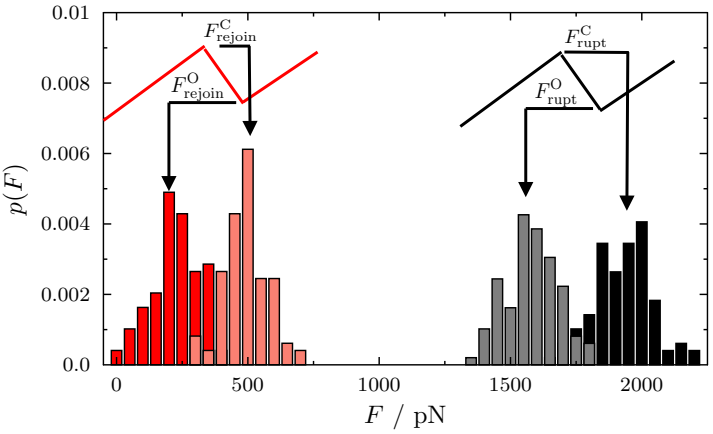

Figure 3.10.: Force distribution $p(F)$ obtained from analysis of 100 FE curves for $\mu = 0.8305\,\mathrm{N/s}$ and $V = 1\,\mathrm{m/s}$.

In addition to the mean rupture forces $\langle F \rangle$, the corresponding forces from the time of rupture, $f_{\mathrm{rupt/rejoin}} = KVt_{\mathrm{rupt/rejoin}}$, were determined. The average values $\langle f \rangle$ were obtained from the distributions $p(f)$ and are plotted in Figure 3.11 (b) as a function of K. All determined values of $\langle f \rangle$ are increasing linearly with the force constant K. The difference $\langle \Delta f \rangle = \left| \langle f^{O} \rangle - \langle f^{C} \rangle \right|$ is increasing with K. Pull and relax mode thus show similar behavior, but the relax mode is shifted to smaller forces f.

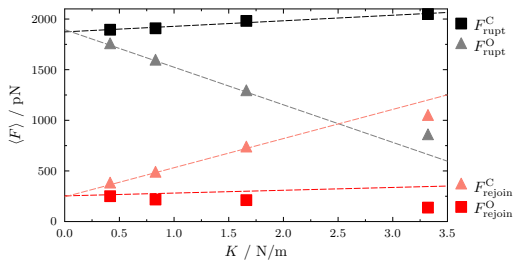

(a) Averages of the characteristic forces $\langle F \rangle$.

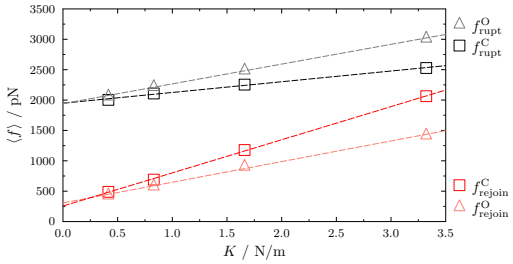

(b) Averages of the characteristic forces $\langle f \rangle$ where $f = \mu t$.

Figure 3.11.: Averages of the characteristic forces (rupture and rejoin forces) $\langle F \rangle$ and $\langle f \rangle$ for $\mu = 0.8305\,\mathrm{N/s}$ as a funtion of K. The dotted lines were obtained by linear regression.

The results of this analysis for all tested loading rates are collected in Figure 3.12. The general trends for $\langle F^{C/O} \rangle$ and $\langle f^{C/O} \rangle$ are the same as for the already discussed loading rate $\mu = 0.8305\,\mathrm{N/s}$. The values of $\langle F^{C}_{rupt} \rangle$ decrease with decreasing loading rate and the values for $\langle F^{O}_{rejoin} \rangle$ are increasing with decreasing loading rates. This means, that the height of the hysteresis loop becomes

smaller for smaller loading rates.
For the forces $\langle f \rangle$, there is a shift to smaller values with decreasing loading rate. Also the difference between $\langle f^{\mathrm{C/O}}_{\mathrm{rupt}} \rangle$ and $\langle f^{\mathrm{C/O}}_{\mathrm{rejoin}} \rangle$ becomes smaller and therefore the length of the hysteresis loop decreases with smaller loading rates. These observations are in accord with the diminishing non-equilibrium character of the FE curves with decreasing loading rate.

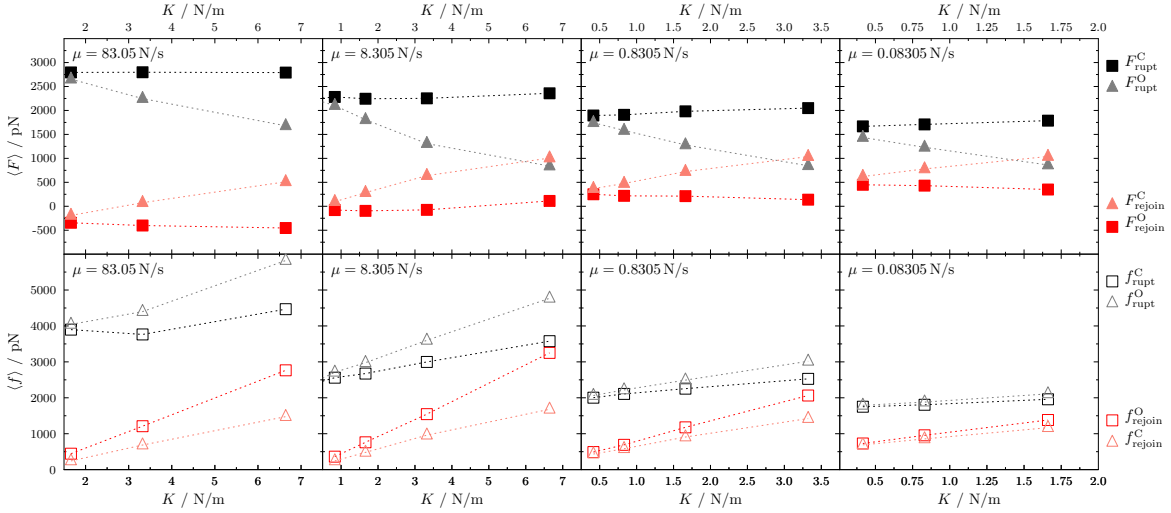

Figure 3.12.: $\langle F \rangle$ (upper panel) and $\langle f \rangle$ (lower panel) as a function of K for all of the performed simulations.

Besides determining the characteristic values $\langle F^{\mathrm{C/O}}_{\mathrm{rupt/rejoin}} \rangle$ and $\langle f^{\mathrm{C/O}}_{\mathrm{rupt/rejoin}} \rangle$, also the slopes of the FE curves were investigated. In eq. (3.4), the slope of the FE is given by K_{eff} and the molecular force constant K_{mol} is given by

$$K_{\mathrm{mol}} = \frac{K K_{\mathrm{eff}}}{K - K_{\mathrm{eff}}}. \tag{3.6}$$

The FE curves for every simulation were analyzed individually. The effective force constants for the closed and open state $K^{\mathrm{C/O}}_{\mathrm{eff}}$ were obtained individually for every single curve via linear regression. The averaged values of $K^{\mathrm{C/O}}_{\mathrm{mol}}$ are plotted in Figure 3.13.

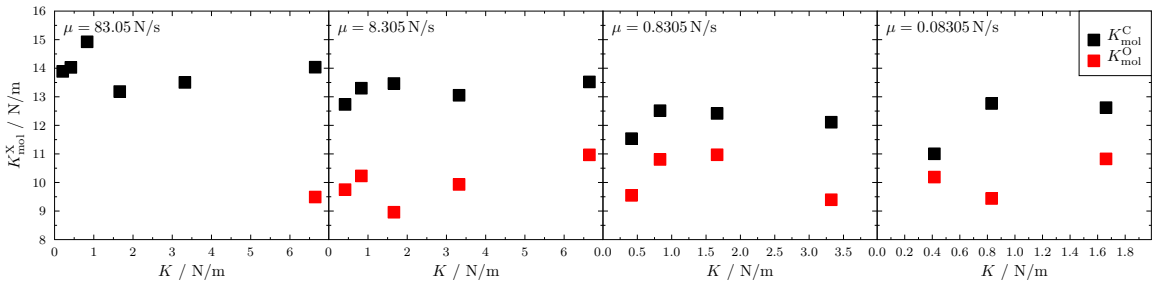

Figure 3.13.: $K^{\mathrm{C/O}}_{\mathrm{mol}}$-values as a function of K.

One can see that the values of $K^{\mathrm{C}}_{\mathrm{mol}}$ are higher than the values of $K^{\mathrm{O}}_{\mathrm{mol}}$. The average values $\langle K^{\mathrm{X}}_{\mathrm{mol}} \rangle$ over all monitored K-values and V-values are

$$\langle K^{\mathrm{C}}_{\mathrm{mol}} \rangle = 13.11\,\mathrm{N/m} \quad \text{and} \quad \langle K^{\mathrm{O}}_{\mathrm{mol}} \rangle = 10.18\,\mathrm{N/m}. \tag{3.7}$$

The closed state is therefore somewhat stiffer and more stable than the open state. This presumably is due to the fact that the closed state is stabilized by a maximum of 16 UU bonds and the open state by a maximum of 8 UE bonds.
Next, the connection between the characteristic F-values and f-values is investigated. According to eq. (3.2), the rupture force F_{rupt} is connected to f_{rupt} via

$$F_{\mathrm{rupt}} = f_{\mathrm{rupt}} - Kq(t_{\mathrm{rupt}}) \tag{3.8}$$

where t_{rupt} is the rupture time. For a simple model of a double-well potential with bare minima located at $q_{0,\mathrm{C}}$ for the closed state a barrier at $q_{0,\mathrm{T}}$ and an open state at $q_{0,\mathrm{O}}$ with $q_{0,\mathrm{X}} = q_{\mathrm{X}} - q(0)$, it is possible to compute the position of the reaction coordinate $q_0(f)$ in a harmonic approximation [55, 56]. This way one obtains the following expression for a FE curve:

$$F(f) = \xi_{\mathrm{C}}(f - Kq_{0,\mathrm{C}})\Theta(f_{\mathrm{rupt}} - f) + \xi_{\mathrm{O}}(f - Kq_{0,\mathrm{O}})\Theta(f - f_{\mathrm{rupt}}) \tag{3.9}$$

where

$$\xi_{\mathrm{X}} = (1 + K/K^{\mathrm{X}}_{\mathrm{mol}})^{-1} \quad ; \quad \mathrm{X} = \mathrm{C},\, \mathrm{O} \tag{3.10}$$

with the molecular stiffness $K^{\mathrm{X}}_{\mathrm{mol}}$ and the step function

$$\Theta(x) = \begin{cases} 1 \text{ for } x \geq 1 \\ 0 \text{ for } x < 1 \end{cases} \quad . \tag{3.11}$$

With eq. (3.9) one can also relate the force measured to the rupture/rejoin time via $F^{\mathrm{C}}_{\mathrm{rupt}} = F(f^{\mathrm{C}}_{\mathrm{rupt}})$ etc., i.e.:

$$\begin{aligned} F^{\mathrm{C}}_{\mathrm{rupt}} &= \xi_{\mathrm{C}}(f^{\mathrm{C}}_{\mathrm{rupt}} - Kq_{0,\mathrm{C}}) \quad ; \qquad F^{\mathrm{O}}_{\mathrm{rupt}} = \xi_{\mathrm{O}}(f^{\mathrm{O}}_{\mathrm{rupt}} - Kq_{0,\mathrm{O}}) \\ F^{\mathrm{C}}_{\mathrm{rejoin}} &= \xi_{\mathrm{C}}(f^{\mathrm{C}}_{\mathrm{rejoin}} - Kq_{0,\mathrm{C}}) \quad ; \qquad F^{\mathrm{O}}_{\mathrm{rejoin}} = \xi_{\mathrm{O}}(f^{\mathrm{O}}_{\mathrm{rejoin}} - Kq_{0,\mathrm{O}}) \end{aligned} \tag{3.12}$$

This kind of analysis was performed for loading rates ranging from $\mu = 0.08305\,\mathrm{N/s}$ to $\mu = 83.05\,\mathrm{N/s}$ and the results for $\mu = 0.8305\,\mathrm{N/s}$ are shown in Figure 3.14. The full symbols refer to the determined characteristic values and the open symbols refer to the ones calculated using eq. (3.12). For $K^{\mathrm{C/O}}_{\mathrm{mol}}$ the values from eq. (3.7) were used, while for $q_{0,\,\mathrm{C/O}}$ the following values were used

$$q_{0,\mathrm{C}} = 0\,\mathrm{nm} \qquad \text{and} \qquad q_{0,\mathrm{O}} = 0.63\,\mathrm{nm}.$$

The value for $q_{0,\mathrm{O}}$ was calculated from the interception point $F(0) = -\xi_{\mathrm{O}} K q_{0,\mathrm{O}}$. For the underlying harmonic potential of the closed state is was assumed, that it has its origin at $q_{0,\mathrm{C}} = 0\,\mathrm{nm}$. As may be seen from Figure 3.14, the calculated values (open symbols) agree well with the values determined from the distribution. This is also true for the other loading rates. Therefore, the Gaussian approximation for the FE-curves used here gives reasonable overall agreement with the F-values determined directly.
The approximately linear behavior of the rupture force $f^{\mathrm{C/O}}_{\mathrm{rupt}}$ and $f^{\mathrm{C/O}}_{\mathrm{rejoin}}$ can also be understood considering the above mentioned harmonic approximation. By neglecting any fluctuations, the rupture event takes place when the force-dependent position of the closed state $q_{\mathrm{C}}(f)$ reaches the position of the transition state, $q_{\mathrm{T}}(f)$ [35]. The force-dependent positions are given by

$$q_{\mathrm{C}}(f) = q_{\mathrm{C}} + \frac{f}{K + K^{\mathrm{C}}_{\mathrm{mol}}} \quad , \quad q_{\mathrm{O}}(f) = q_{\mathrm{O}} + \frac{f - Kq_{\mathrm{OC}}}{K + K^{\mathrm{O}}_{\mathrm{mol}}} \quad , \quad q_{\mathrm{T}}(f) = q_{\mathrm{T}} + \frac{f + Kq_{\mathrm{TC}}}{K^{\mathrm{T}}_{\mathrm{mol}} - K} \tag{3.13}$$

with $q_{\mathrm{XY}} = q_{\mathrm{X}} - q_{\mathrm{Y}}$. The rupture forces can then be determined from $q_{\mathrm{C}}(f^{\mathrm{C}}_{\mathrm{rupt}}) = q_{\mathrm{T}}(f^{\mathrm{T}}_{\mathrm{rupt}})$ which yields $f \approx (K^{\mathrm{C}}_{\mathrm{mol}} + K) q_{\mathrm{TC}}$ assuming a sharp barrier ($K^{\mathrm{T}}_{\mathrm{mol}} \gg K$). A least square fit to all the data yields values for q_{TC} in the range of 0.2 nm.

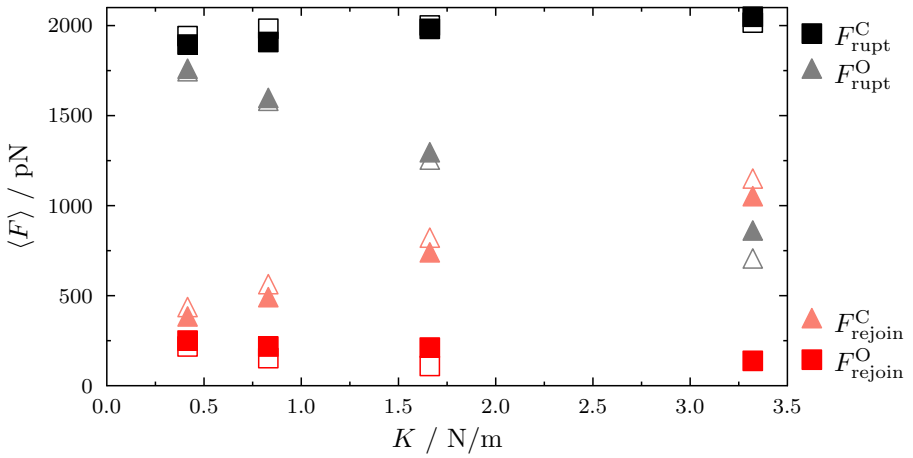

Figure 3.14.: Average of the characteristic forces (rupture and rejoin forces) as a function of K for a loading rate of $\mu = 0.8305\,\mathrm{N/s}$. Full symbols are determined from distributions and open symbols are obtained using eq. (3.12).

3.3.3. Analysis of the hydrogen bond network

As already shown in Figure 3.4, the states C and O are stabilized by different types of hydrogen bonds. In order to define the states more clearly, the dependencies of the average number of hydrogen bonds, $\langle \#\mathrm{HB} \rangle$, and the average end-to-end distance, $\langle q \rangle$, on the extension are used to compute $\langle \#\mathrm{HB} \rangle$ as a function of $\langle q \rangle$. The results are shown in Figure 3.15 in the pull mode for $K = 0.8305\,\mathrm{N/m}$ and different values of the velocity V. The behavior for other values of the force constant K is almost identical, which indicates that there is no observable K-dependence for $\langle \#\mathrm{HB} \rangle(\langle q \rangle)$ (cf. Figure B.9). In addition, the results for the relax mode simulations are almost identical apart from somewhat larger values for the maximum number of UE-bonds (cf. Figure B.10).
Figure 3.15 clearly shows that the average number of UU-bonds, $\langle \#\mathrm{UU} \rangle$, is independent of the loading rate, whereas the maximum value of $\langle \#\mathrm{UE} \rangle$ decreases with increasing loading rate (cf. Figure 3.16). The UE-bonds start to build at a distance of $\langle q \rangle \approx 1.6\,\mathrm{nm}$. In [48], this region was already shown to be the region right before the transition C $\rightarrow$ O. The average number of UU-bonds, $\langle \#\mathrm{UU} \rangle$, decreases from almost the maximum possible value of 16 to roughly 8 at $\langle q \rangle \approx 1.6\,\mathrm{nm}$. At $\langle \#\mathrm{UU} \rangle = 8$, almost exactly the inflection point of the $\langle \#\mathrm{UU} \rangle$ versus $\langle q \rangle$ is reached.
With these observations one can define the characteristic positions in the force-dependent free-energy landscape of the calixarene system. For the closed state, the value of q with 8 UU-bonds is chosen as the minimum and the value of q with the maximum number of UE-bonds as the corresponding minimum of the open state for each simulation. The mean positions of the relevant minima of the C-state and the O-state were determined by the following definitions:

$$\begin{aligned} q_{\mathrm{C}} &= \langle q \rangle(\langle \#\mathrm{UU} \rangle = 8) \\ q_{\mathrm{O}} &= \langle q \rangle(\langle \#\mathrm{UE} \rangle = \max) \end{aligned} \tag{3.14}$$

Fluctuations are given by the variances of these quantities obtained from the individual simula-

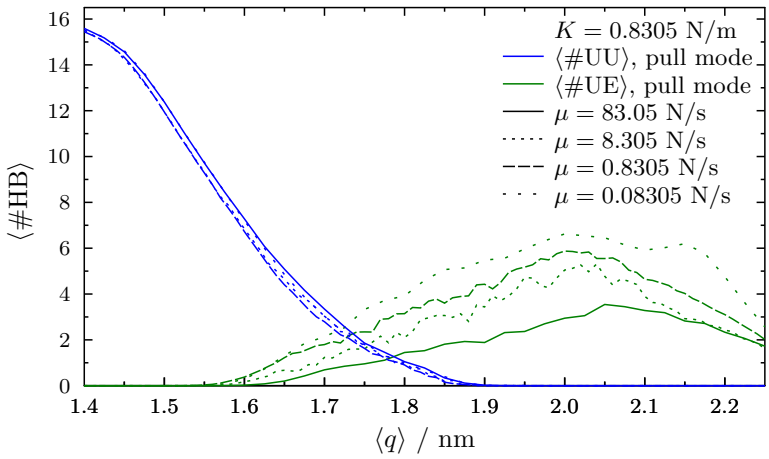

Figure 3.15.: Averaged number of hydrogen bonds, $\langle$#HB$\rangle$, as a function of the mean end-to-end distance $\langle q \rangle$ for different loading rates ranging from $0.8305\,\mathrm{N/s}$ to $83.05\,\mathrm{N/s}$. UU-bonds are depicted in blue and UE-bonds in green. The averaged number of hydrogen bonds $\langle$#HB$\rangle$ for the positions q_T and q_O are shown in Figure 3.16.

tions. These are straightforward, natural definitions of the open and closed state. The position of the transitions state, q_T, is more difficult to define. Because the closed state C is stabilized by UU-bonds and in the open state only UE-bonds exists, a working definition that q_T is located at that value of the end-to-end distance at which the number of UU-bonds and UE-bonds coincide,

$$q_\mathrm{T} = \langle q \rangle (\langle \#\mathrm{UU} \rangle = \langle \#\mathrm{UE} \rangle), \tag{3.15}$$

is a reasonable choice. In Figure 3.16, the averaged number of H-bonds $\langle$#HB$\rangle$ is shown at q_T and q_O (cf. Figure 3.15). With an increasing loading rate, $\langle$#UE$\rangle$ at q_O and $\langle$#HB$\rangle$ at q_T decrease. This trend is purely influenced by the shape of the $\langle$#UE$\rangle$ ($\langle q \rangle$) curve, which depends on the loading rate μ and is K-independent.

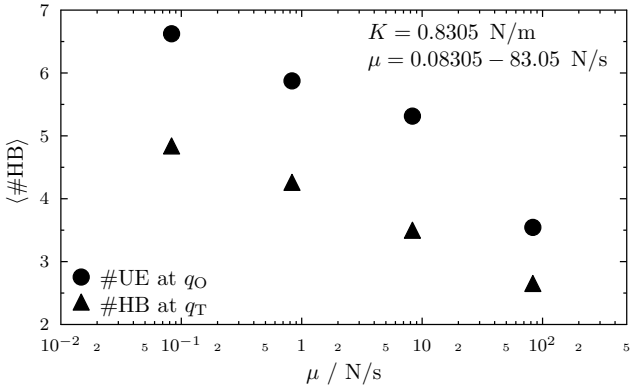

Figure 3.16.: $\langle$#HB$\rangle$ at q_O and q_C as a function of the loading rate for $K = 0.8305\,\mathrm{N/m}$. The corresponding averaged curves $\langle$#HB$\rangle$ ($\langle q \rangle$) are shown in Figure 3.15.

Using the definitions given in eqs. (3.14,3.15), the results in Figure 3.17 are obtained. Here, the collected values for q_X (X = C, T, O) are shown. With the obtained values one can determine the distances from the transition state, q_{TC} and q_{OT}. From Figure 3.17, it is clear that these values do not vary strongly and the mean values are given by $\langle q_{TC} \rangle \approx 0.13\,\text{nm}$ and $\langle q_{OT} \rangle \approx 0.41\,\text{nm}$ for the pull mode and $\langle q_{TC} \rangle \approx 0.15\,\text{nm}$ and $\langle q_{OT} \rangle \approx 0.38\,\text{nm}$ for the relax mode.

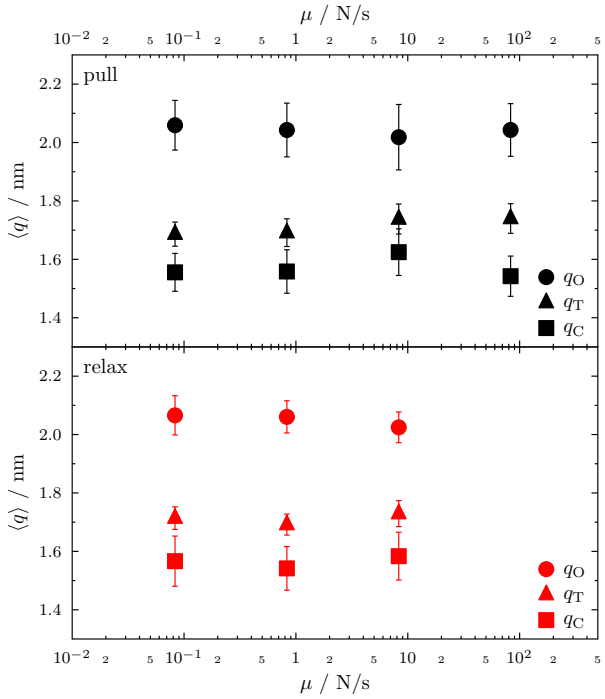

Figure 3.17.: Values q_X as determined from eqs. (3.14, 3.15) as a function of the loading rate for $K = 0.8305\,\text{N/s}$. The error bars are given by the variances. Upper panel: pull mode; lower panel: relax mode.

Using these values, the fragility defined in [57] will be analyzed. Here, the fragility-index is defined as

$$\gamma(F) = \frac{q_{TC}(F) - q_{OT}(F)}{q_{TC}(F) + q_{OT}(F)}. \tag{3.16}$$

The location of the barrier along the reaction coordinate is related to the fragility-index of the molecule, which determines to what degree the transition from C to O is sensitive to the force. Here, $\gamma < 0$ corresponds to a brittle structure at the calculated force and the position of the barrier is near the C state. This means that the molecule is not easy to deform under the influence of force. For $\gamma > 0$, the structure is flexible. The barrier is located near the open state and the molecule is easily deformed under the influence of force.
In order to calculate the fragility-index, the loading rate-dependent values $q_X(\mu)$ displayed in Figure 3.17 were converted into force-dependent ones, $q_X(F)$. This was done via the mean-force values, see Figure 3.11. The results are shown in Figure 3.18. The values obtained for the fragility-index at a given loading rate, but different combinations of K and V, are almost identical to the ones shown.
The calculated fragility averages around $\langle \gamma \rangle \approx -0.5$. This values implies, that the molecule is not easy to deform under the influence of force. This was also observed in the conducted simulations.

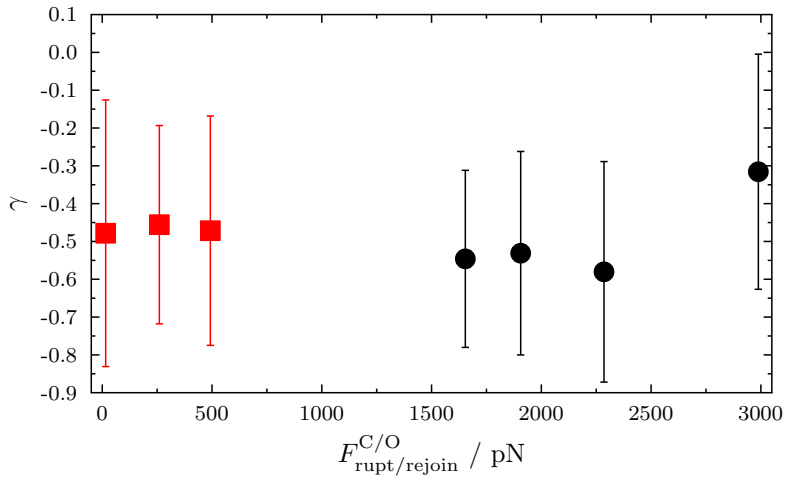

Figure 3.18.: Fragility-index γ as defined in eq. (3.16) as a function of the force.

The here studied calixarene therefore behaves drastically different from the RNA studied in [57], where a strong force dependence of the fragility was found. Of course, it is not possible to rule out a transition to more fragile structure ($\gamma \leq 1$) in the small force regime. To obtain such data, simulations at smaller loading rates have to be performed. For these the computational cost is very high due to the longer simulation time needed.

3.3.4. Kinetic rates

The kinetic rates for the rupture event $k^{\mathrm{C}}_{\mathrm{rupt}}$, transition C $\rightarrow$ T, and the kinetic rates for the rejoin event $k^{\mathrm{O}}_{\mathrm{rejoin}}$, transition O $\rightarrow$ T, can be calculated from the distributions of the rupture forces (see Figure 3.10). The model-independent procedure of [58] was used for this. The rates are calculated by the straightforward-to-implement word equation

$$k^{\mathrm{X}}(F) = \frac{\text{loading rate } \mu}{\text{trajectories in state X at } F} \times \frac{\text{counts in bin } F}{\text{bin width}}. \tag{3.17}$$

As discussed in section 3.3.2, the rupture forces $F^{\mathrm{C}}_{\mathrm{rupt}}$ and the rejoin forces $F^{\mathrm{O}}_{\mathrm{rejoin}}$ are almost independent of the stiffness K and therefore these distributions are used to determine the kinetic rates. The results are shown in Figure 3.19.

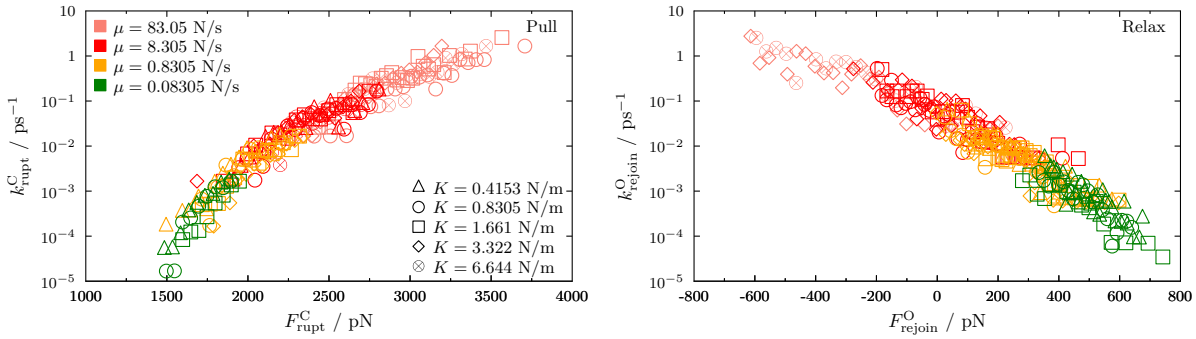

(a) Pull mode: rates $k^{\mathrm{C}}_{\mathrm{rupt}}$ as a function of the rupture forces $F^{\mathrm{C}}_{\mathrm{rupt}}$.

(b) Relax: mode: rates $k^{\mathrm{O}}_{\mathrm{rejoin}}$ as a function of the rejoin forces $F^{\mathrm{O}}_{\mathrm{rejoin}}$.

Figure 3.19.: Rates $k^{\mathrm{C}}_{\mathrm{rupt}}$ as a function of the rupture forces $F^{\mathrm{C}}_{\mathrm{rupt}}$ and rates $k^{\mathrm{O}}_{\mathrm{rejoin}}$ as a function of $F^{\mathrm{O}}_{\mathrm{rejoin}}$. Different loading rates are indicated by different colors and different K as different symbol types (cf. left panel).

The simulations allow to extract $k^{\mathrm{C}}_{\mathrm{rupt}}$ and $k^{\mathrm{O}}_{\mathrm{rejoin}}$ values ranging over almost five orders of magnitude. It is evident that the rates are practically independent of K in the range of K considered. By varying K for a given loading rate it is possible to cover a larger range of forces. Consequently a larger range of rates can be calculated. A variation of the K allows to broaden the dynamical range that can be monitored.

To study the K-dependence of the kinetic rates further, the values for $k^{\mathrm{C}}_{\mathrm{rupt}}(f^{\mathrm{C}}_{\mathrm{rupt}})$ were calculated. The results for two values of K are presented in Figure 3.20 (full symbols). Here, a strong dependence on the stiffness K contrary to the $k^{\mathrm{C}}_{\mathrm{rupt}}(F^{\mathrm{C}}_{\mathrm{rupt}})$ can be observed. This K-dependence can be completely traced back to the already discussed K-dependence of the force in section 3.3.2. With eq. (3.12), one can calculate $F^{\mathrm{C/O}}_{\mathrm{rupt/rejoin}}$ from $f^{\mathrm{C/O}}_{\mathrm{rupt/rejoin}}$ and can therefore switch between $k_{\mathrm{C}}(F^{\mathrm{C}}_{\mathrm{rupt}})$ and $k_{\mathrm{C}}(f^{\mathrm{C}}_{\mathrm{rupt}})$ or $k_{\mathrm{O}}(F^{\mathrm{O}}_{\mathrm{rejoin}})$ and $k_{\mathrm{O}}(f^{\mathrm{O}}_{\mathrm{rejoin}})$. The calculated $k^{\mathrm{C}}_{\mathrm{rupt}}(f^{\mathrm{C}}_{\mathrm{rupt}})$ from $k^{\mathrm{C}}_{\mathrm{rupt}}(F^{\mathrm{C}}_{\mathrm{rupt}})$ are shown as open symbols in Figure 3.20. The found values for the evaluated and calculated rates, closed and open symbols, agree very well. There is no extra dependence on the force constant K except the one scaling the forces. This agrees with the observations made in earlier studies. [55, 56, 59]

The force-dependent kinetic rates can be fitted to one of various expressions of $k^{\mathrm{C}}_{\mathrm{rupt}}(F)$. [35, 36, 59, 60] From these model it is possible to extract parameters like the bare rate $k^{\mathrm{C,0}}_{\mathrm{rupt}}$, the bare

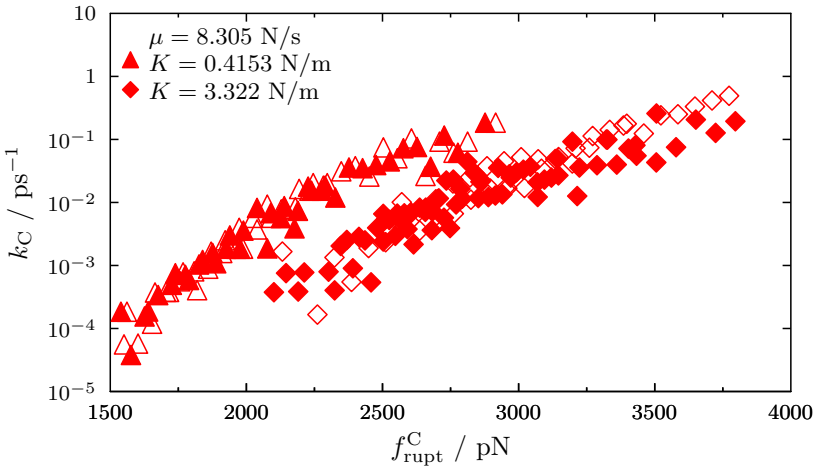

Figure 3.20.: Kinetic rates $k^C_{rupt}(f^C_{rupt})$ as determined from the distributions $p(f)$ as a function of $f = \mu t$ (full symbols) and $k^C_{rupt}(f^C_{rupt})$(calculated) computed from $k^C_{rupt}(F^C_{rupt})$ from Figure 3.19 using eq. (3.12) (open symbols).

barrier ΔU_C and the effective distance from the barrier q_{TC}. In order to gain these information the model of an quadratic-cusp shaped energy described in [36] is used. The rate k^C_{rupt} is given by eq. (2.49) and can be recast in the form

$$\ln k^C_{rupt}(F) = A(F) + \beta \Delta U_C \left(1 - \left(1 - \frac{F}{F_{crit}}\right)\right) \text{ with } A(F) = \ln\left(k^{C,0}_{rupt}\left(1 - \frac{F}{F_{crit}}\right)\right) \quad (3.18)$$

Using the latter equation to fit the data shown in Figure 3.19 (a), the values in Table 3.3 are obtained. Here the F-dependence of $A(F)$ was neglected.

Table 3.3.: Data obtained by fitting different ranges of F^C_{rupt} of the data shown in Figure 3.19 (a) with eq. (3.18). The distance from the barrier is calculated by $q_{TC} = \frac{2\Delta U_C}{F_{crit}}$.

F^C_{rupt} / pN	A	ΔU_C /pN nm	F_{crit} / pN	q_{TC} / nm
≤ 2000	-44.45	9.74	2439.38	0.0080
≤ 2200	-42.97	9.45	2495.68	0.0076
≤ 2500	-35.15	7.94	2890.51	0.0055
≤ 2800	-34.30	7.76	2939.56	0.0053

Here several ranges of F^C_{rupt} are fitted to check if the obtained values for the critical force are dependent on the fitting range. One finds a strong dependency: the larger the maximum fitted value F^C_{rupt} the larger the critical force F_{crit}. As already mentioned in section 2.1.6, these fits are only meaningful in the regime of activated dynamics and for forces $F^C_{rupt} < F_{crit}$. For simulations performed in the activated regime, the obtained critical force F_{crit} should be independent of the fitting range. This result is therefore an indication that the simulations are performed in the diffusive or drift regime (cf. Figure 2.9). Nonetheless it is possible to gain information about the molecular energy landscape without using any of these fits and can further validate that the simulations are performed in the regime of diffusive or drift dynamincs.

Assuming that the molecular energy landscape is described by a harmonic potential with a cusp barrier located at q_{T}, the critical force can be estimated by $F_{\mathrm{crit}} \approx K_{\mathrm{mol}} q_{\mathrm{TC}}$. Using the results from section 3.3.2, $K_{\mathrm{mol}}^{\mathrm{C}} \approx 10\,\mathrm{N/m}$ and $q_{\mathrm{TC}} \approx 0.2\,\mathrm{nm}$, one finds $F_{\mathrm{crit}} \approx 2000\,\mathrm{pN}$.
Another value for q_{TC} can be determined from the potential of mean force observed in [48] (cf. Figure 3.21). Assuming that the shoulder turns into a barrier in the double well region of the combined potential, one gets with $q_{\mathrm{TC}} \approx 0.4\,\mathrm{nm}$ a larger value for the critical force of $F_{\mathrm{crit}} \approx 5000\,\mathrm{pN}$.
With these values, the critical force F_{crit} ranges from 2000 pN to 5000 pN and one can take this as an indication for a crossover from activated to diffusive dynamics within in the range of forces monitored by the performed simulations.
Beside a critical force F_{crit} also a critical loading rate μ_{crit} exists which can be defined by [61]

$$\mu_{\mathrm{crit}} = F_{\mathrm{crit}} \frac{D}{q_{\mathrm{TC}}^2} \tag{3.19}$$

where D is the diffusion coefficient which is typically around $D \approx 10^8\,\mathrm{nm^2/s}$ [62]. With the above given approximate critical forces F_{crit} one obtains a critical loading μ_{crit} rate which ranges from $0.1\,\mathrm{N/s}$ to $10\,\mathrm{N/s}$. The loading rate μ of the performed simulations are ranging from $0.08305\,\mathrm{N/s}$ to $83.05\,\mathrm{N/s}$. This is an further indication for a crossover from activated to diffusive dynamics.
Another, different, approach that defines the effective distance from the barrier as the force-derivative of the barrier $\Delta U_{\mathrm{C}}(F)$ appears to be less model dependent and only assumes activated dynamics. [57] In this approach, the rate is given by

$$k_{\mathrm{rupt}}^{\mathrm{C}}(F) = k_{\mathrm{rupt}}^{\mathrm{C},0} e^{-\beta \Delta U_{\mathrm{C}}(F)} \tag{3.20}$$

and the distance from the effective barrier is given by $q_{\mathrm{TC}} = -\frac{d\Delta U_{\mathrm{C}}(F)}{dF}$. The data for $k_{\mathrm{rupt}}^{\mathrm{C}}$ and $k_{\mathrm{rejoin}}^{\mathrm{O}}$ (Figure 3.19) were smoothed and a numerical derivative of $(T \ln(k^{\mathrm{X}}))$, X = C, O, was performed. The resulting effective barriers $q_{\mathrm{TC}}(F)$ and $q_{\mathrm{OT}}(F)$, were fitted using a linear approximation as in eq. (3.13). This yields $q_{\mathrm{TC}} \approx 0.1\,\mathrm{nm}$ and $q_{\mathrm{OT}} \approx 0.05\,\mathrm{nm}$. Particularly the value of q_{OT} appears unphysically small.
From these results one can conjecture that the simulations are most probably in the dynamical regime of a crossover from activated dynamics to diffusive dynamics. This is well expected for the rather large pulling velocities employed by FPMD simulations and it is well known that this crossover takes place for fast pulling. [56, 62] Therefore analyzing the kinetic rates apparently is not giving meaningful results for q_{TC} and q_{OT} and are not in agreement with the results obtained from the potential of mean force in [48].

3.3.5. Stochastic models

In order to investigate the crossover from activated to diffusive dynamics in detail, it is helpful to consider the kinetics in a model energy landscape. In this section, the reversible bond breaking observed for the calixarene T14 is considered to be a process of diffusive barrier crossing in a model potential. The results are compared with the results obtained from FPMD simulations. The used potential was obtained by fitting the potential of mean force (PMF), $U_{\mathrm{PMF}}(q)$, from [48] to a fourth degree polynomial

$$U_0(q) = aq^4 + bq^3 + cq^2 + dq + e. \tag{3.21}$$

The result of the fit is shown in Figure 3.21 (a) and the parameters are given in App. B.3. An external force is applied through the external potential $U_{\mathrm{ext}}(q, f) = \frac{1}{2} K (q - q_{\mathrm{C}}^0)^2 - f(q - q_{\mathrm{C}}^0)$ and

the total potential is given by

$$U(q, f) = U_0(q) + U_{\text{ext}}(q, f) \tag{3.22}$$

where $q_C^0 = q_C(0)$. The influence of the force $f = \mu t$ on the potential $U(q, f)$ for a force constant of $K = 0.8305\,\text{N/m}$ is shown in Figure 3.21 (b). The external potential tilts the energy landscape and causes the force-dependent extrema, $q_C(f)$, $q_T(f)$ and $q_O(f)$ (cf. eq. (B.1)) to appear.

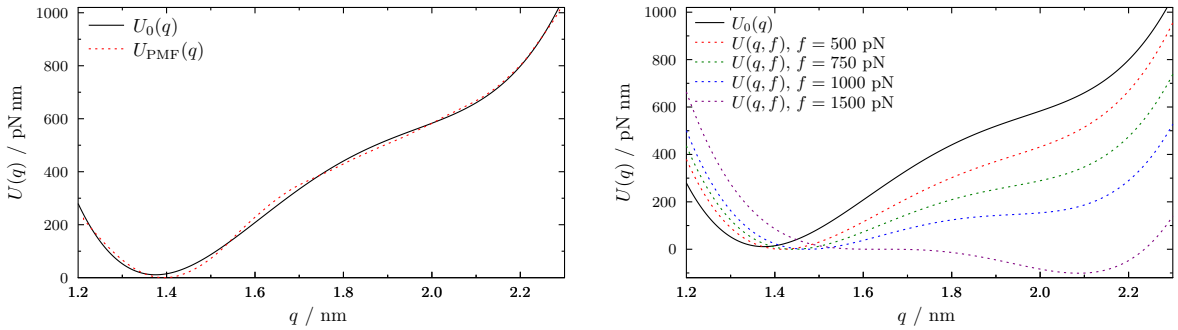

(a) Measured PMF $U_{\text{PMF}}(q)$ [48] and fitted function $U_0(q)$.

(b) Influence of $f = \mu t$ on the potential $U(q, f)$.

Figure 3.21.: (a) PMF $U_{\text{PMF}}(q)$ and fitted function $U_0(q)$. (b) Influence of an external force ($K = 0.8305\,\text{N/m}$) on $U(q, f)$.

The extrema $q_X(f)$ for force constant $K = 0.8305\,\text{N/m}$ are shown in Figure 3.22 (a). The activated regime for a transition from state C to state O only ranges from $f_{\text{crit}}^{\text{rejoin}} = 1098\,\text{pN}$ to $f_{\text{crit}}^{\text{rupt}} = 1501\,\text{pN}$. Here, the three states C, T and O exist and barrier crossing is possible. The lower bound defines the critical force $f_{\text{crit}}^{\text{rejoin}}$ in the relax mode and the upper bound defines the critical force $f_{\text{crit}}^{\text{rupt}}$ in the pull mode.

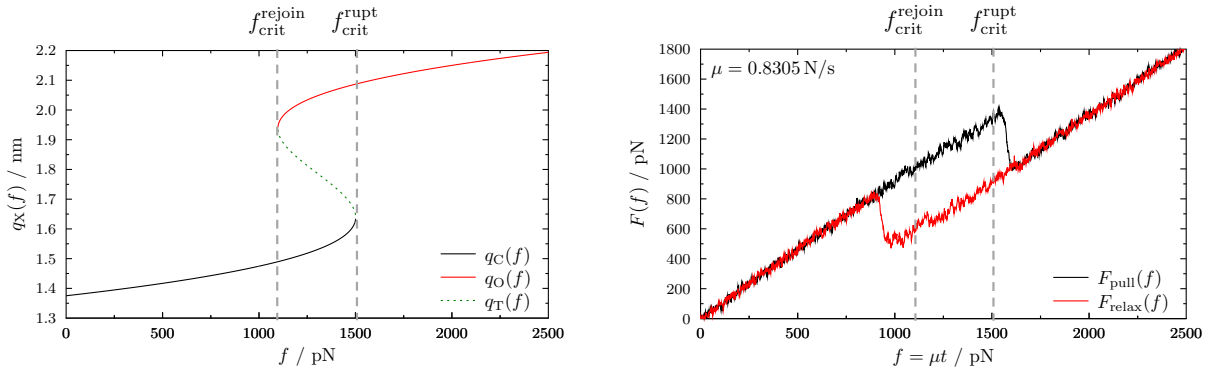

(a) $q_X(f)$ with X = C, T, O as a function of $f = \mu t$. The area in between the grey dotted lines marks the activated regime.

(b) Typical FE curve for a KMC simulation performed with a loading rate of $\mu = 0.8305\,\text{N/s}$ and a force constant of $K = 0.8305\,\text{N/m}$.

Figure 3.22.: Minima $q_X(f)$ as a function of f and measured force F as a function of f. The critical forces $f_{\text{rupt/rejoin}}^{\text{C/O}}$ are marked as dotted lines.

Stochastic trajectories $q(f)$ using KMC as described in section 2.1.6 were generated. From these trajectories the measured force can be calculated by $F(f) = \frac{1}{2}K(f/K - (q(f) - q(0))^2$. A typical FE curve for a KMC simulation performed with a loading rate of $\mu = 0.8305\,\mathrm{N/s}$ and force constant of $K = 0.8305\,\mathrm{N/m}$ is shown in Figure 3.22 (b). Other used parameters are the step-size $\Delta q = 1.0 \cdot 10^{-3}\,\mathrm{nm}$ and a diffusion coefficient of $D = 1.0 \cdot 10^{8}\,\mathrm{nm^2/s}$. This curve shows the same trends in the pull and the relax mode as a FE curve obtained from a FPMD simulation (cf. Figure 3.6 and 3.8). Note, that $f^{\mathrm{C/O}}_{\mathrm{rupt}} \leq f^{\mathrm{rupt}}_{\mathrm{crit}}$ and $f^{\mathrm{C/O}}_{\mathrm{rejoin}} \geq f^{\mathrm{rejoin}}_{\mathrm{crit}}$. This means that the simulation is performed in the diffusive regime.
Analogously to analysis performed for the FPMD simulations in section 3.3.2, the mean characteristic forces $\langle f^{\mathrm{C/O}}_{\mathrm{rupt/rejoin}} \rangle$ are determined for sets of different K and V at different loading rates. For each set of parameters 1000 simulations were performed. The tested loading rates are $\mu = 0.8305\,\mathrm{N/s}$ and $\mu = 0.008305\,\mathrm{N/s}$. The loading rate is therefore an order of magnitude smaller than the lowest loading rate performed with FPMD simulations (cf. Table 3.2). The obtained mean values of $f^{\mathrm{C/O}}_{\mathrm{rupt/rejoin}}$ as a function of K are shown in Figure 3.23.

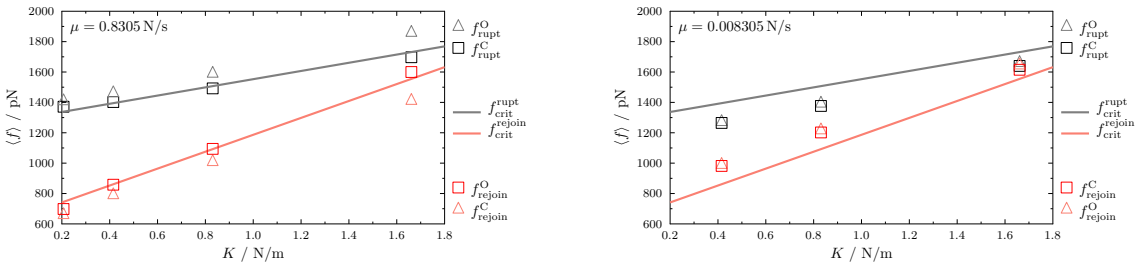

(a) Characterisitc forces $f^{\mathrm{C/O}}_{\mathrm{rupt/rejoin}}$ from KMC simulations. The lines mark the critical forces $f^{\mathrm{rupt/rejoin}}_{\mathrm{crit}}$.

(b) Characterisitc forces $f^{\mathrm{C/O}}_{\mathrm{rupt/rejoin}}$ from KMC simulations. The lines mark the critical forces $f^{\mathrm{rupt/rejoin}}_{\mathrm{crit}}$.

Figure 3.23.: Mean values of the characteristic forces $f^{\mathrm{C/O}}_{\mathrm{rupt/rejoin}}$ as a function of K for the two tested loading rates $\mu = 0.83505\,\mathrm{N/s}$ and $\mu = 0.0083505\,\mathrm{N/s}$.

The trends of the mean characteristic forces are the same as for the FPMD simulations but are shifted to smaller f-values (cf. Figure 3.12). The critical forces $f^{\mathrm{rupt/rejoin}}_{\mathrm{crit}}$ for the pull and the relax mode are shown as lines. For the faster loading rate $\mu = 0.8305\,\mathrm{N/s}$, the found values for the rupture forces are $\langle f^{\mathrm{C}}_{\mathrm{rupt}} \rangle \approx f^{\mathrm{rupt}}_{\mathrm{crit}}$ and $\langle f^{\mathrm{O}}_{\mathrm{rupt}} \rangle > f^{\mathrm{rupt}}_{\mathrm{crit}}$ for all shown K-values. For the rejoin event the same observations can be made, respectively. Here, the mean rejoin forces $\langle f^{\mathrm{O}}_{\mathrm{rejoin}} \rangle \approx f^{\mathrm{rejoin}}_{\mathrm{crit}}$ for all shown K-values. This behavior is indicating that the rupture and the rejoin event are taking place in the regime of diffusive dynamics for all shown K-values as defined in [33]: $\langle f^{\mathrm{C/O}}_{\mathrm{rupt/rejoin}} \rangle \approx f^{\mathrm{rupt/rejoin}}_{\mathrm{crit}}$. The mean characteristic forces $\langle f^{\mathrm{C/O}}_{\mathrm{rupt/rejoin}} \rangle$ for the slower loading rate $\mu = 0.008305\,\mathrm{N/s}$, cf. Figure 3.23 (b), are all well in the regime of activated dynamics [33]: $\langle f^{\mathrm{C/O}}_{\mathrm{rejoin}} \rangle > f^{\mathrm{rejoin}}_{\mathrm{crit}}$ and $\langle f^{\mathrm{C/O}}_{\mathrm{rupt}} \rangle < f^{\mathrm{rupt}}_{\mathrm{crit}}$.
Next, the obtained distributions $p(f)$ are investigated and compared to their counterparts obtained by FPMD simulations. The rupture force distribution for the characteristic forces $f^{\mathrm{C/O}}_{\mathrm{rupt}}$ is shown in Figure 3.24 for $\mu = 0.008305\,\mathrm{N/s}$ and $K = 0.8305\,\mathrm{N/s}$. The form the distributions is the same as observed for the FPMD simulations (cf. Figure 3.10).
In addition to the distributions of $f^{\mathrm{C/O}}_{\mathrm{rupt}}$ obtained from the KMC simulations, the distribution can be calculated using the two state model discussed in section 2.1.6. The transition rates are calculated as inverse MFPTs (eq. (2.48)) using the model potential $U(q, f)$. The results for the

calculated $p(f)$ is shown as dotted lines in Figure 3.24 and these agree with the distributions obtained by the KMC simulations. This agreement is expected because the simulations are performed within the activated regime (see Figure 3.22 (a)). In this regime the used integration limits for calculating the MFPT are well defined.

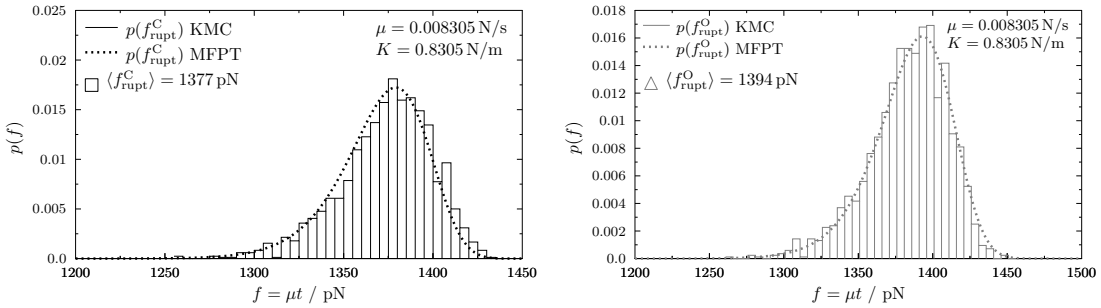

(a) Force distribution $p(f)$ for the characteristic forces f^{C}_{rupt}.

(b) Force distribution $p(f)$ for the characteristic forces f^{O}_{rupt}.

Figure 3.24.: Force distributions $p(f)$ of the charaterisitc forces $f^{C/O}_{rupt}$ in the pull mode. Used parameters: $K = 0.8305\,N/m$, $\mu = 0.008305\,N/s$, diffusion coefficient $D = 1.0 \cdot 10^{8}\,nm^2/s$, step size $\Delta q = 1.0 \cdot 10^{-3}\,nm$.

For the faster loading rate $\mu = 0.8305\,N/s$, the rupture force distributions $p(f)$ show the same form as the for the slower loading rate and therefore have the same characteristics as the ones obtained by FPMD simulations. This is also in agreement with the observations made in [61]: whether a simulation is performed in the activated, diffusive or drift regime, the characteristics of the rupture force distributions do not change.
Unlike in the simulations at the slower loading rate, the force distributions cannot be calculated using mean first passage times. This is due to the fact, that $q_C(f)$ and $q_T(f)$ disappear for forces $f > f_{crit}$. In Figure 3.25 the obtained values for $p(f)$ are shown by dotted lines.

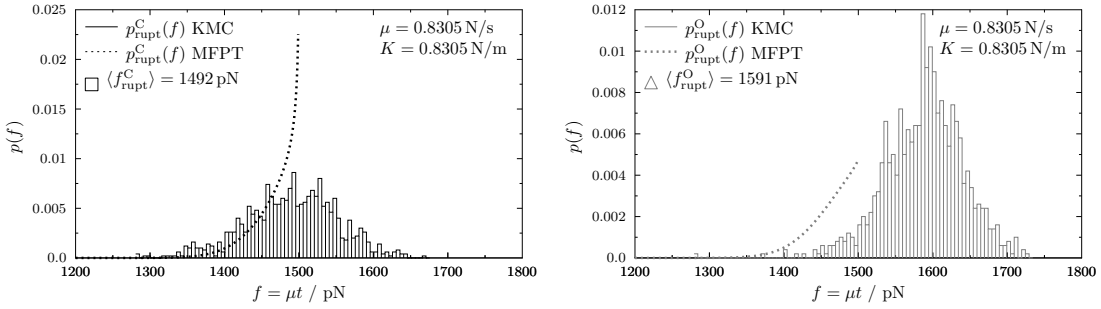

(a) Force distribution $p(f)$ for the characteristic forces f^{C}_{rupt}.

(b) Force distribution $p(f)$ for the characteristic forces f^{O}_{rupt}.

Figure 3.25.: Comparision of the results obtained from the KMC simulations (1000 runs) and the MFPT calculations for the loading rate $\mu = 0.8305\,N/s$. Used parameters: $K = 0.8305\,N/m$, diffusion coefficient $D = 1.0 \cdot 10^{8}\,nm^2/s$, step size $\Delta q = 1.0 \cdot 10^{-3}\,nm$.

The KMC simulations and the results obtained via MFPT deliver comparable results to the

FPMD simulations. With these methods it is possible to monitor the mean rupture forces over several orders of magnitude of loading rates for a well defined energy landscape $U(q, f)$. The calculated force spectrum is shown in Figure 3.26. Here the values at lower loading rates for forces $\langle f^{\mathrm{C/O}}_{\mathrm{rupt/rejoin}}\rangle < f^{\mathrm{rupt}}_{\mathrm{crit}}$ were obtained via MFPT (open symbols). Rupture forces $\langle f^{\mathrm{C/O}}_{\mathrm{rupt/rejoin}}\rangle \geq f^{\mathrm{rupt}}_{\mathrm{crit}}$ were calculated using KMC simulations. Within the diffusive regime it is possible to calculate $\langle f^{\mathrm{O}}_{\mathrm{rupt}}\rangle$ (black squares), for forces $\gg f^{\mathrm{rupt}}_{\mathrm{crit}}$ (drift regime) one can calculate only the $\langle f^{\mathrm{O}}_{\mathrm{rupt}}\rangle$-values (grey triangles).

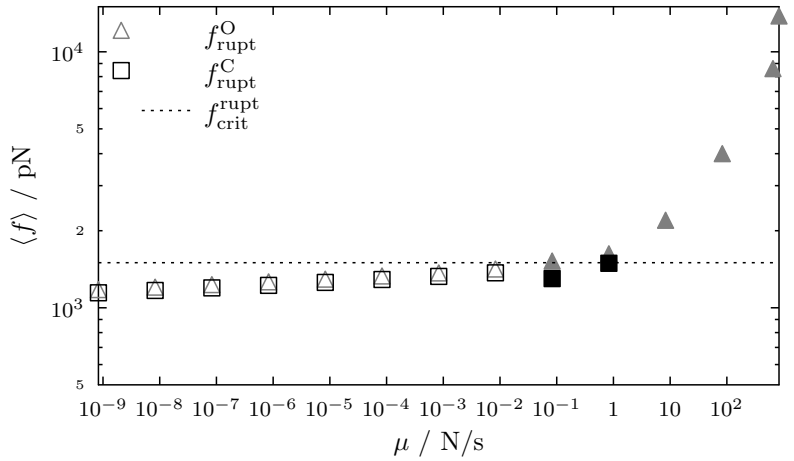

Figure 3.26.: Mean values of the characteristic forces $f^{\mathrm{C/O}}_{\mathrm{rupt}}$ as a function of the loading rate μ (force spectrum). The open symbols are obtained via MFPT calculations and the full symbols are obtained via KMC simulations. $K = 0.8305\,\mathrm{N/m}$.

In this section it was shown with the help of a well-defined energy landscape based on the PMF of the calixarene T14, that it is not possible to differentiate the regime a simulation has been performed in based on the distribution of the forces $p(F)$ and $p(f)$. Therefore, it is not possible to gain further information concerning the dynamic regime just from the force distributions as they are obtained in FPMD simulations.

3.3.6. Conclusion

Here, the dependence of FPMD simulations on the pulling parameters were studied for the reversibly unbinding model system calixarene T14. The pulling velocity V and the force constant K were varied for loading rates $\mu = KV$ ranging from $0.08305\,\mathrm{N/s}$ to $83.05\,\mathrm{N/s}$.
In section 3.3.2 the dependence of the characteristic forces, $F^{\mathrm{C/O}}_{\mathrm{rupt/rejoin}}$, on the pulling parameters were investigated. It was shown that the rupture $F^{\mathrm{C}}_{\mathrm{rupt}}$ and the rejoin force $F^{\mathrm{O}}_{\mathrm{rupt}}$ depend only very weakly on variations of K for given loading rate whereas the forces $F^{\mathrm{O}}_{\mathrm{rupt}}$ and $F^{\mathrm{C}}_{\mathrm{rejoin}}$ are strongly dependent on K in a linear fashion. This behavior can be easily understood in terms of a simple harmonic model for the molecular energy landscape. Such an harmonic model can easily reproduce the found results of the here performed FPMD simulations.
One of the main structural characteristic of the investigated model system is the hydrogen bond network which is analyzed in section 3.3.3. The open and closed state are stabilized by two different networks of hydrogen bonds. These networks and their dependence on the pulling

parameters were investigated at different loading rates. For this kind of analysis, the average number of hydrogen bonds $\langle \#\mathrm{HB} \rangle$ were plotted as a function of the average end-to-end distance $\langle q \rangle$. Here, one could see that the $\langle \#\mathrm{HB} \rangle$-values show only a minimal dependence of the force constant K for a given loading rate μ. For the range of investigated loading rates one can see no dependence of the average number of UU-bonds $\langle \#\mathrm{UU} \rangle$ whereas the average number of UE-bonds $\langle \#\mathrm{UE} \rangle$ does change. Interestingly, the results do not depend on the used mode, pull or relax. Furthermore, values for the distances to the barrier, q_{TC} and q_{OT}, were obtained. Here, the barrier is located nearer to the closed state for the range of the here investigated forces and the system shows therefore a rather brittle structure.
In section 3.3.4 the kinetic rates for the transition from the closed to the open state were extracted from the distributions of rupture forces. For the obtained rates one can find a clear cut deviation from the simple $\exp(\beta q_{\mathrm{TC}} F)$-like behavior predicted by the phenomenological Bell model. Furthermore, neither a fit of the rates to existing expressions derived from the mean first passage times for model energy landscapes nor a model-free determination of the distance to the barrier gives reliable results for the involved quantities q_{TC} and q_{OT}. This might be a hint towards a failure of the underlying assumption of thermally activated transitions which was further investigated in section 3.3.5 via stochastic models. Here, the crossover from activated to diffusive dynamics were studied considering the kinetics in a model energy landscape. The reversible bond breaking observed in the FPMD simulations are considered to be a process of diffusive barrier crossing in a model potential. As a potential a polynomial fit of the potential of mean force was used and an external force is applied through an external potential. Stochastic trajectories using KMC simulations were generated and the transition rates were calculated as inverse MFPTs. Here, one could observe that it is not possible to differentiate the regime a simulation has been performed in based on the distribution of the forces $p(F)$ and $p(f)$.

3.4. Calixarene T17 and T20

In this section, the results of the FPMD simulations of the calixarenes T17 and T20 are discussed. They differ from the previously investigated calixarene T14 in section 3.3 by a longer loop-length of 17 CH_2 units (T17) or 20 CH_2 units (T20).
Due to the longer loop-length, three different states exist: a closed state C, an intermediate state I and an open state O (see Figure Figure 3.4). The setup for the simulations is described in section 3.2 and parameters such as the initial box size, number of atoms and molecules for the conducted FPMD simulations are shown in Table 3.1. Like in the previous section, the pulling parameters, pulling velocity V and stiffness K, were varied and the different parameters sets are shown in Table 3.4.

$\mu = 8.305\,\mathrm{N/s}$		$\mu = 0.8305\,\mathrm{N/s}$		$\mu = 0.08305\,\mathrm{N/s}$	
K[N/m]	V[m/s]	K[N/m]	V[m/s]	K[N/m]	V[m/s]
0.8305	10	0.8305	1	0.8305	0.1
1.661	5	1.661	0.5		
3.322	2.5	3.322	0.25		

Table 3.4.: Combinations of K and V used in the simulations. For the loading rate $\mu = 0.08305\,\mathrm{N/s}$ only simulations for the calixarene T17 were performed.

3.4.1. Disussion of a single FPMD simulation: T17 and T20

Here, the results of a single FPMD simulation for the calixarene T17 and T20 are discussed. Representative results for the end-to-end distance q, measured force F and the number of hydrogen bonds #HB are shown in Figure 3.27 and are directly compared with the curves presented in Figure 3.6 for the calixarene T14.
As already shown in Figure 3.4, the calixarenes T17 and T20 are able to form an intermediate state which is stabilized by UE-bonds. In the RE curves for both system one can identify a shoulder when going from the closed state to the open state. This little extra step marks the transition into state I and is at the same extension as the maximum number of UE-bonds ($\#\mathrm{UE}_{\max}$). For the here shown RE curves it can be found at $q^{\mathrm{I}}_{\mathrm{rupt}} \approx 2.2\,\mathrm{nm}$ for the calixarene T17 and T20. These $q^{\mathrm{I}}_{\mathrm{rupt}}$-values are therefore almost at the same position as the $q^{\mathrm{O}}_{\mathrm{rupt}}$-value of the calixarene T14. This is not surprising because the open state O for the calixarene T14 is only stabilized by UE-bonds and in section 3.3.3 it was shown that $q_{\mathrm{O}} = \langle q \rangle (\langle \#\mathrm{UE} \rangle = \max)$ is equal to $q^{\mathrm{O}}_{\mathrm{rupt}}$ for T14. The same observation can be made for the relax mode: the $q^{\mathrm{O}}_{\mathrm{rejoin}}$-values for the calixarene T14 are equal to the $q^{\mathrm{I}}_{\mathrm{rejoin}}$-values.
Next, a look at the $q^{\mathrm{O}}_{\mathrm{rupt}}$-values is taken. This value is increasing with an increment of 0.2 nm with each additional set of $3CH_2$-units: starting at 2.2 nm for T14, 2.4 nm for T17 to 2.6 nm for T20. For the calixarenes T17 and T20, the structure is no longer stabilized by UE-bonds at $q^{\mathrm{O}}_{\mathrm{rupt}}$ which is due to the longer loop-length. In the next section, the FE curves and the characteristic forces will be discussed in depth.

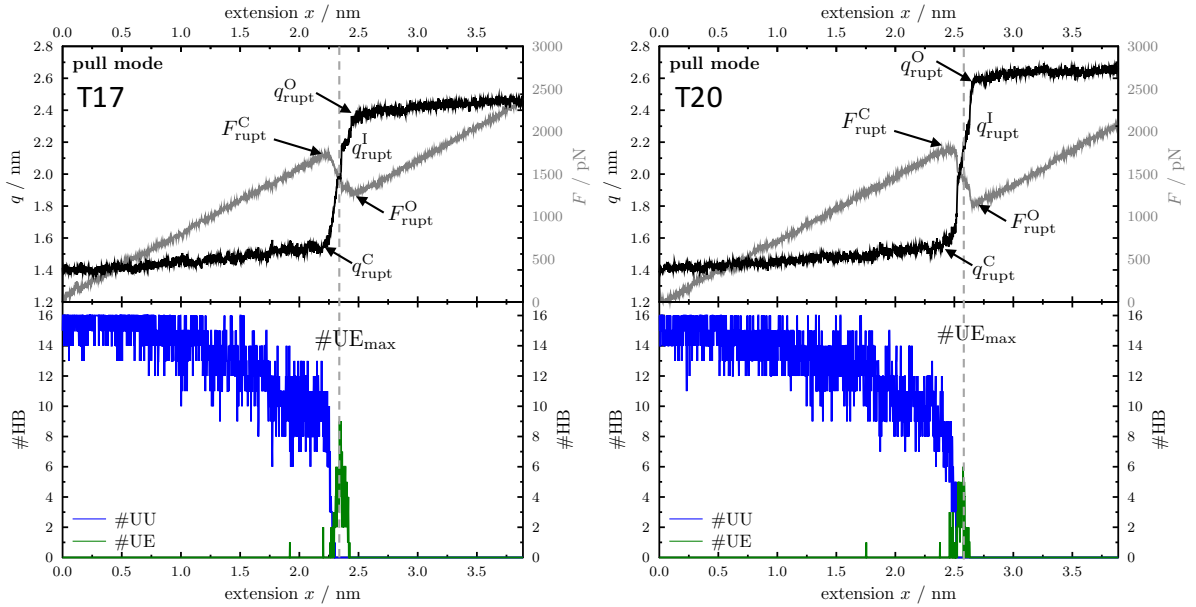

Figure 3.27.: Pull mode: All properties are plotted as a function of the extension $x = Vt$. The pulling parameters are $K = 0.8305\,\mathrm{N/m}$ and $V = 1\,\mathrm{m/s}$, resulting in a loading rate of $\mu = 0.8305\,\mathrm{N/s}$. Upper panel: sample RE curve (black) and FE curve (grey). The vertical dashed grey line marks the intermediate state I and coincides with #UE$_{max}$. Lower panel: number of hydrogen bonds #HB.

3.4.2. Analysis of the FE curves

In this section, the characteristic forces $F^{\mathrm{C/I/O,T17/T20}}_{\mathrm{rupt/rejoin}}$ for the calixarenes T17 and T20 are discussed and compared with the characteristic forces obtained for the calixarene T14, $F^{\mathrm{C/O,T14}}_{\mathrm{rupt/rejoin}}$ (cf. Figure 3.12). The analysis of the forces $F^{\mathrm{C/O,T17/T20}}_{\mathrm{rupt/rejoin}}$ were performed as described in section 3.3.2 and for the $F^{\mathrm{I,T17/T20}}_{\mathrm{rupt/rejoin}}$-values the F-values at #UE$_{max}$ were taken. The obtained characteristic forces for all performed simulations are plotted against K in Figure 3.28 and the results are illustrated via schematic drawings of FE-curves in Figure 3.29.
The pull mode is analyzed first and the following observations are made: For the maximum values for all three calixarenes one finds

$$F^{\mathrm{C,T14}}_{\mathrm{rupt}} \approx F^{\mathrm{C,T17/T20}}_{\mathrm{rupt}}.$$

This is due to the fact that all three systems are stabilized by the same hydrogen bond network. Up to the rupture force $F^{\mathrm{C}}_{\mathrm{rupt}}$ the calixarene systems are stabilized mainly by UU-bonds (see Figure 3.29, blue region). After this first rupture event which marks the transition C,T14 $\rightarrow$ O,T14 and C,T17/T20 $\rightarrow$ I,T17/T20, all three calixarenes are stabilized by UE-bonds (see Figure 3.29, green region). The number of UE-bond reaches a maximum at $F^{\mathrm{O,T14}}_{\mathrm{rupt}}$ and $F^{\mathrm{I,T17/T20}}_{\mathrm{rupt}}$ and one finds

$$F^{\mathrm{O,T14}}_{\mathrm{rupt}} \approx F^{\mathrm{I,T17/T20}}_{\mathrm{rupt}}.$$

For the calixarene T14 the measured force F is increasing in a linear fashion and the system is stabilized by UE-bonds. The calixarenes with a longer loop length show a different behavior: Due

to the longer loop length the calixarenes can be further pulled apart and the the force $F_{\text{rupt}}^{\text{O,T17/T20}}$ marks transition into the open state O,T17/T20. The open state for these T17 and T20 system is only stabilized by the loops (see Figure 3.29, grey region) and one finds

$$F_{\text{rupt}}^{\text{O,T17}} > F_{\text{rupt}}^{\text{O,T20}}.$$

These forces are therefore only influenced by the loop-length. One can conclude, that all characteristic forces for these calixarene systems are approximately the same as long as the hydrogen bond network is involved.

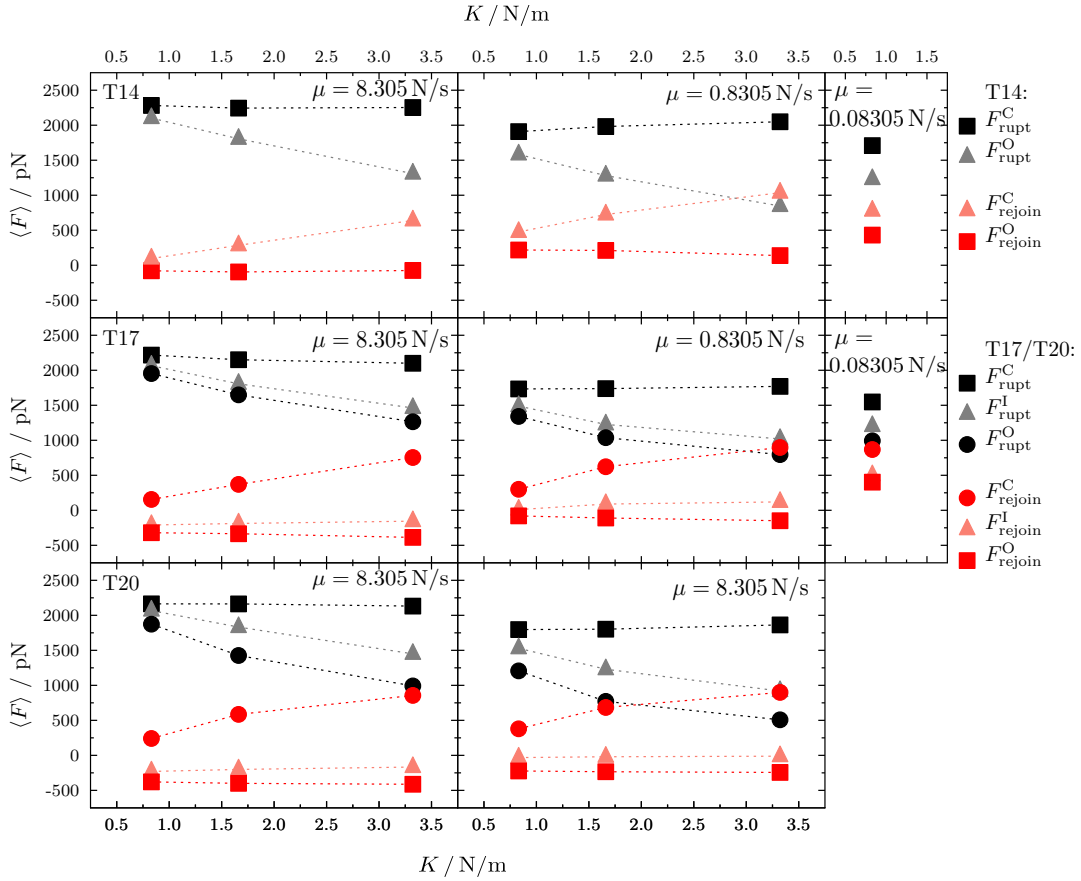

Figure 3.28.: $\langle F \rangle$ as a function of K for all performed T17 (middle panel) and T20 (lower panel) simulations. Note that for the fast loading rate ($\mu = 8.305\,\text{N/s}$, T17 and T20) not all systems reached the closed state C. The upper panel shows the obtained values for the calixarene T14.

Next, the characteristic forces of the different calixarene systems obtained in the relax mode are compared. Here, one can observe the same behavior as in the pull mode: the values of the characteristic forces are comparable as long as the hydrogen bond network is present:

$$F_{\text{rejoin}}^{\text{C,T14}} \approx F_{\text{rejoin}}^{\text{C,T17/T20}} \quad \text{and} \quad F_{\text{rejoin}}^{\text{O,T14}} \approx F_{\text{rejoin}}^{\text{I,T17/T20}}.$$

These observations are also illustrated in Figure 3.29 in the lower panel (**B**). For the forces

$F^{\mathrm{O,T17/T20}}_{\mathrm{rejoin}}$ one finds

$$F^{\mathrm{O,T17}}_{\mathrm{rejoin}} > F^{\mathrm{O,T20}}_{\mathrm{rejoin}}$$

which is due to the longer loop-length of the calixarene T20.

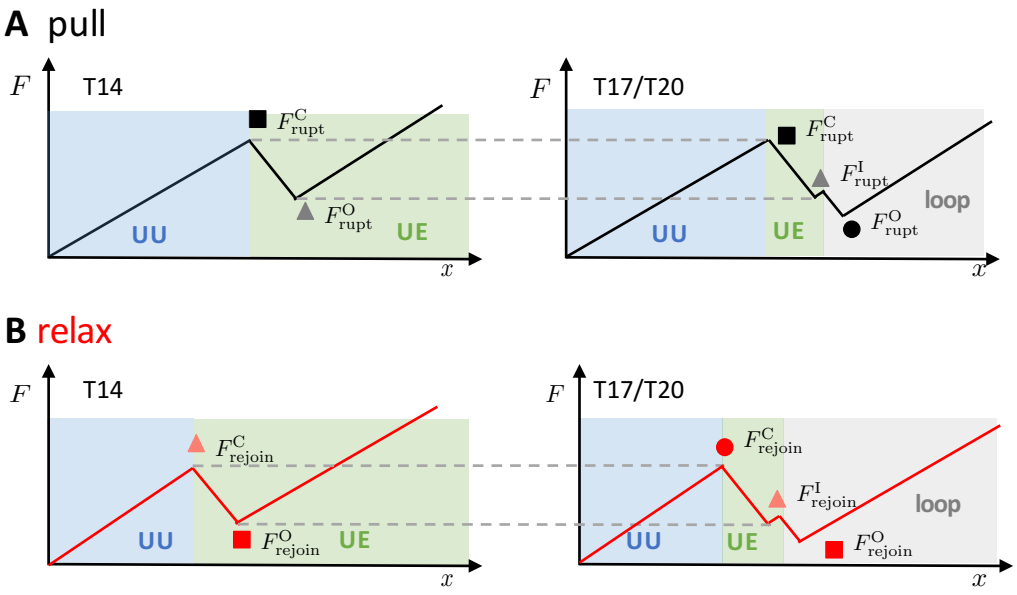

Figure 3.29.: Schematic drawing of the FE-curves for the calixarene T14 (left panel) and the calixarenes T17/T20 (right panel). The FE-curves and the characteristic forces in the pull mode are compared in the upper panel (**A**) and in the relax mode in the lower panel (**B**).

3.4.3. Influence of the pull distance on the degree of reversibility

Another important aspect of the relax simulation is the degree of reversibility which is given by

$$\text{reversibility}(\mu) = \frac{\text{simulations reaching closed state C}}{\text{performed simulations}} \times 100\%. \tag{3.23}$$

The obtained values are shown in Table 3.5. The calixarene T14 is at these loading rates (0.08305 N/s to 8.305 N/s) completely reversible. For all tested systems, the degree of reversibility is independent of the chosen pulling parameters K and V and only dependent on the loading rate μ. For every loading rate the reversibility is uniquely determined by the loop-length and is decreasing with increasing loop-length. This means that the degree of reversibility is tunable by the chosen loop-length.

Table 3.5.: Degree of reversibility for the relax simulations of the calixarenes T17 and T20.

μ	T17	T20
0.08305	100%	—
0.8305	$\sim$ 80%	$\sim$ 70%
8.305	$\sim$ 30%	$\sim$ 20%

The degree of reversibility will now be further investigated for the calixarene T20 at a loading rate of $\mu = 8.305\,\mathrm{N/s}$, $K = 0.8305\,\mathrm{N/m}$ and $V = 10\,\mathrm{m/s}$. The system is pulled apart up to a specific extension which corresponds to an average end-to-end distance $\langle q \rangle$. The pulling direction is the inverted and the system is relaxed. The percentage of simulations reaching the intermediate state I and the closed state C are calculated and shown in Figure 3.30.

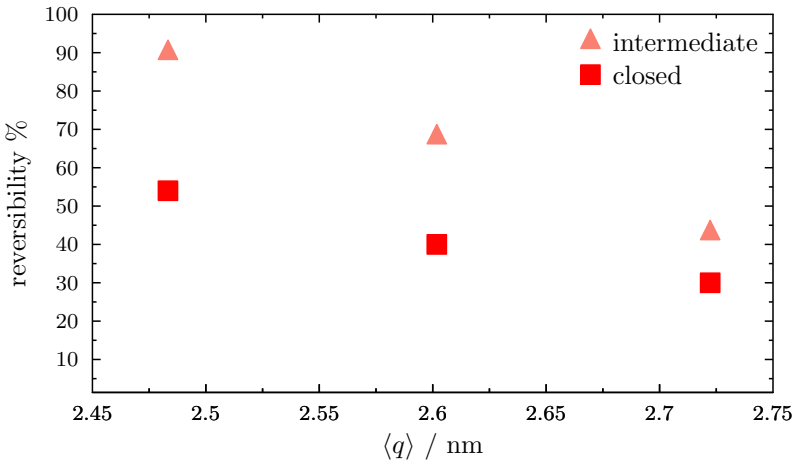

Figure 3.30.: Reversibility as a function of the average end-to-end distance $\langle q \rangle$ for calixarene T20. Used pulling parameters $\mu = 8.305\,\mathrm{N/s}$, $K = 0.8305\,\mathrm{N/m}$ and $V = 10\,\mathrm{m/s}$.

For the chosen $\langle q \rangle$-values, the T17 system is no longer stabilized by any hydrogen bonds (cf. Figure 3.31). The reversibility for both states is clearly dependent on the chosen distance $\langle q \rangle$ and decreasing with increasing starting values $\langle q \rangle$.
For $\langle q \rangle = 2.6\,\mathrm{nm}$ the degree of reversibility into the closed state C,T20 is $\sim 40\%$ and therefore the same as for the calixarene T17 (see Table 3.5). Here the same $\langle q \rangle$-value as a starting point for both simulations has been used which leads to the conclusion that for $\langle q \rangle < q_{\mathrm{rupt}}^{\mathrm{O,T17/T20}}$ the loop-length is not of importance for the reversibility.

3.4.4. Analysis of the hydrogen bond network

The importance of the hydrogen bond network has already been mentioned numerous times and is therefore characterized next. The obtained results for the calixarenes T17 and T20 are compared with the results of the calixarene T14 described in section 3.3.3. The calixarenes T17 and T20 are interpreted as three state model (closed, intermediate and open) due to their longer loop length. In order to define the states more clearly, the hydrogen bond network is analyzed using the same approach as in section 3.3.3.
In Figure 3.31 the average number of hydrogen bonds $\langle \#\mathrm{HB} \rangle$ is shown as a function of the average end-to-end distance $\langle q \rangle$ for different loading rates. Like for the calixarene T14, the UU-bonds, $\langle \#\mathrm{UU} \rangle$, are insensitive to a change in loading rate but the UE-bonds, $\langle \#\mathrm{UE} \rangle$ show a rather strong dependence on the loading rate in the here shown range. The UE-bonds increase with decreasing loading rate. For a constant loading rate $\langle \#\mathrm{UE} \rangle(\langle q \rangle)$ is K-independent. The T20 system shows the same behavior.
Next, the results for the different calixarenes systems for one loading rate ($\mu = 0.8305\,\mathrm{N/s}$) are compared and shown in Figure 3.32. The $\langle \#\mathrm{UU} \rangle$-curves are identical whereas the form of the

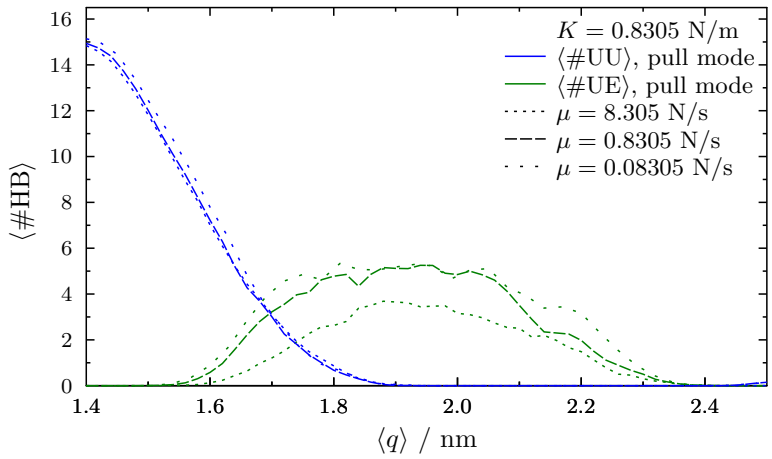

Figure 3.31.: Calixarene T17: Average number of hydrogen bonds ⟨#HB⟩ as a function of the mean end-to-end distance ⟨q⟩ for different loading rates ranging from 0.08305 N/s to 8.305 N/s.

⟨#UE⟩-curves does differ: with an increasing loop length, the maximum does shift to smaller ⟨q⟩-values. A simple explanation for this behavior could be that for the T14 calixarenes the shorter loops are stabilizing the UE-bonds additionaly because the system is restricted in its movement. The other calixarenes T17 and T20 can therefore move more freely. Furthermore the systems could be additionally destabilized due to steric effects. The longer loops need more space and and are therefore more likely to interfere with each other.

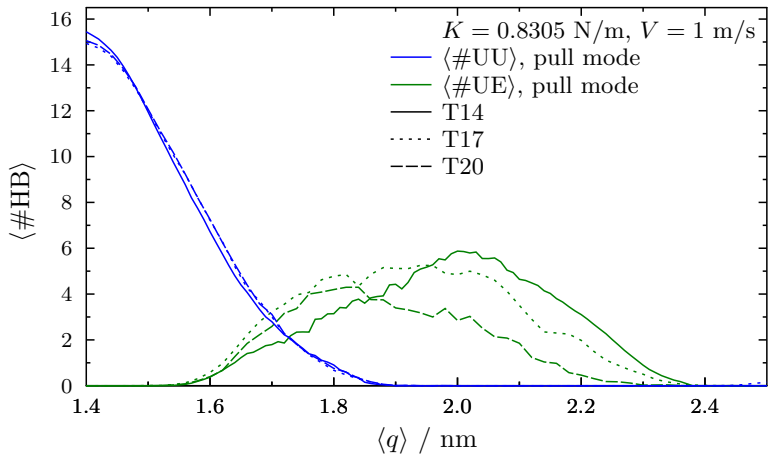

Figure 3.32.: Comparison of the average number of hydrogen bonds ⟨#HB⟩ as a function of the mean end-to-end distance ⟨q⟩ for the different calixarenes systems.

Using the definitions

$$q_C = \langle q\rangle(\langle\#UU\rangle = 8) \qquad q_T = \langle q\rangle(\langle\#UU\rangle = \langle\#UE\rangle) \qquad q_I = \langle q\rangle(\langle\#UE\rangle = \max)) \quad (3.24)$$

the results in Figure 3.33 are obtained. The different $\langle q_X \rangle$-values are shown as a function of the loading rate for a force constant of $K = 0.8305\,\mathrm{N/m}$. The dashed grey lines are the average values obtained for the calixarene T14 by eqs. (3.14, 3.15).
The $\langle q_C \rangle$-values are in agreement for all three calixarenes which is due to the identical behavior of the $\langle \#UU \rangle(\langle q \rangle)$-function. For the position of the transition state $\langle q_T \rangle$ (transition C $\rightarrow$ I) one finds similar values. As discussed for the calixarene T14 this value depends on the shapes of the UE-curve which is as shown in Figure 3.32 for the three investigated calixarene systems.

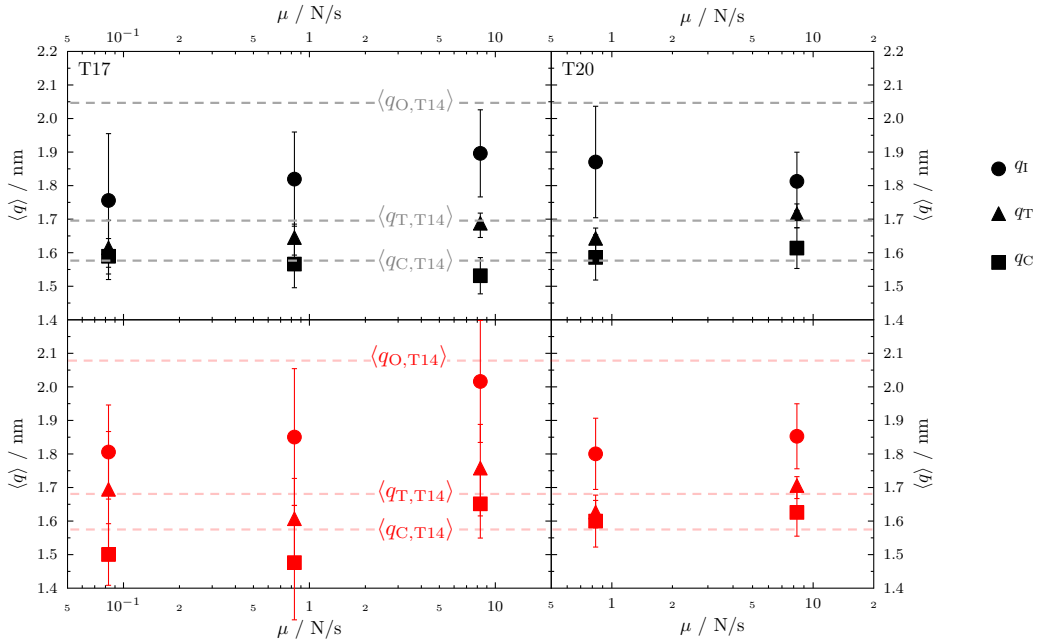

Figure 3.33.: Values q_X as a function of the loading rate for the calixarenes T17 (left) and T20 (right). Upper panel: Pull mode. Lower panel: Relax mode. The dashed lines are the average values obtained for the calixarene T14 (cf. section 3.3.3) by eqs. (3.14, 3.15).

Next the obtained values $\langle q_I \rangle$ are investigated. Note that the definition of the open state O,T14 corresponds to the definition of the intermediate state I,T17/T20. These values are as already discussed shifted to smaller values of $\langle q \rangle$ due to steric effects. The $\langle q_I \rangle$-values are insensitive to a variation of μ in the range of the tested parameters. Even though the $\langle q_I \rangle$-values do differ, the corresponding $\langle F^I_{rupt} \rangle$-values are almost identical (see section 3.4.2).
Lastly, a definition for the open state is discussed. A definition based on the hydrogen bond network is not sensible because the open state for the T17 and T20 systems is not stabilized by hydrogen bonds (see Figure 3.31) but by the loops. A reasonable choice for the open state would therefore be the end-to-end distance $q^{O,T17/T20}_{rupt}$ as defined in section 3.4.1. Using this approach gives the values $\langle q^{O,T17}_{rupt} \rangle \approx 2.38\,\mathrm{nm}$ and $\langle q^{O,T20}_{rupt} \rangle \approx 2.57\,\mathrm{nm}$. These values are also in agreement with the observations made in section 3.4.1.

3.4.5. Conclusion

In this section the dependence of FPMD simulations on the pulling parameters were studied for the reversibly unbinding systems calixarenes T17 and T20 and the results are compared with the results for the calixarene T14 (cf. section 3.3). The here investigated systems differ by a longer loop-length with 17 CH_2 units (T17) or 20 CH_2 (T20) units and can therefore be pulled apart further than the calixarene T14 with just 14 CH_2 units.
In section 3.4.2 the characteristic forces $F_{\mathrm{rupt/rejoin}}^{\mathrm{C/I/O,T17/T20}}$ are investigated. Here, one can find that the characteristic rupture forces $F_{\mathrm{rupt}}^{\mathrm{C/I,T17/T20}}$ are almost identical to the values $F_{\mathrm{rupt}}^{\mathrm{C/O,T14}}$ when comparing the same set of pulling parameters K and V. The same behavior can also be found for characteristic rejoin forces $F_{\mathrm{rejoin}}^{\mathrm{C/I,T17/T20}}$. The characteristic forces show therefore the same behavior as long as the hydrogen bond network is involved. The influence of the loop-length is negligible.
Another interesting aspect is the degree of reversibility which is discussed in section 3.4.3. The reversibility is defined as the percentage of simulations which find the closed state C. One can find a clear dependence on the loop length: the longer the loop the further the calixarene can be pulled apart and the less likely it is that the closed state C is reached. Furthermore it was observed that the degree of reversibility is only dependent on the loading rate μ but not on the chosen pulling parameters K and V.
Lastly the hydrogen bond network was investigated. Like for the calixarene T14 the average number of hydrogen bonds $\langle \#\mathrm{HB} \rangle$ was analyzed as a function of the average end-to-end distance $\langle q \rangle$. Here, one could see that only the behavior of the $\langle \#\mathrm{UE} \rangle(\langle q \rangle)$-curve is dependent on the loop-length. With increasing loop-length the position of $\langle \#\mathrm{UE}_{\mathrm{max}} \rangle$ is shifting towards smaller $\langle q \rangle$-values. From this one can conclude that a longer loop is destabilizing the intermediate state I due to steric effects.

4. Molecular dynamics simulations of phospholipid bilayers

Biomembranes are important soft condensed matter structures which surround cells and their inner organelles. These approximately three nanometer thick hydrophobic films typically delimit the environment that serves as the margin between life and death for individual cells. [63, 64] They maintain relevant concentration gradients and act as selective filter for ions and molecules. Beside this passive role they also have an active role as a host of a number of metabolic and biosynthetic activities. [64]
The view on the structure of biomembranes has evolved over the years. The first model dates back to 1925. Gorter and Grendel [65] showed with first experiments that biological membranes are thin biomolecular structures made of a double layer of lipids. In 1935 this model was refined by Danielli and Davson [66]. Their improved model took the presence of proteins in membranes into account. The model on which the modern view of biological membranes is based is the "fluid mosaic" model of Singer and Nicholson [67]. It was developed in 1972 and describes the biomembranes as a fluid bilayer which is composed of many types of lipids. In the bilayer, there are proteins embedded or attached and molecules are free to move on the bilayer plane. Because of the great variety of lipids and protein molecules the bilayer surface looks like a mosaic, hence the name. The main components of a cell membrane are phospholipids, cholesterol and glycolipids. The most abundant phospholipids are phosphatidylcholines. A schematic drawing illustrating the complexity of a biomembrane is shown in Figure 4.1. [64]

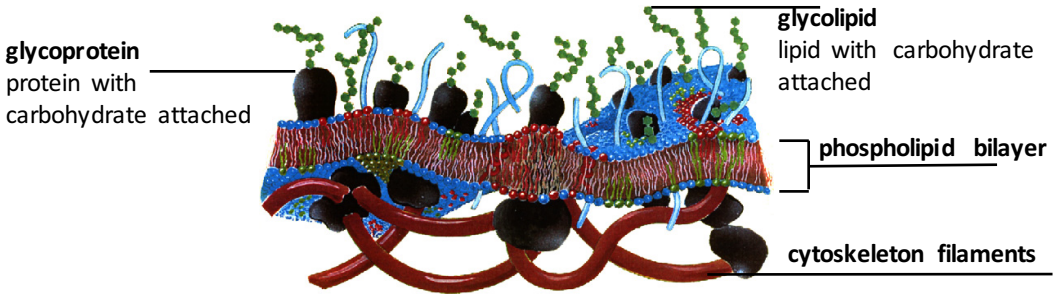

Figure 4.1.: Schematic drawing illustrating the complexity of a biomembrane taken from [64].

Because of the complexity of biomembrane structures, it is necessary to investigate simplified systems, so-called *reconstituted lipid bilayers*. These systems are only composed of one or two lipid species and embedded proteins or sterols. These reconstituted lipid bilayers provide a model system for biological membranes. The understanding of the physics of such simplified membranes yields further insight into their biological function. Furthermore they are used to investigate the cause of diseases which leads to the development of new therapeutics. They have been studied extensively by experimental methods such as spectroscopy, microscopy, fluorescence, scattering and calorimetry. In addition, a lot of theoretical models exist which are important

for the understanding of structure-function relations. They provide not only a framework of experimental data, but can also serve as a source of inspiration for future experiment. [64]
On the theoretical level, the properties of lipid bilayers can be studied on different time and length scales. In the easiest representation the bilayer is considered as an elastic sheet which is sufficient to describe quantities such as bending rigidity, spontaneous curvature and surface tension. [68] To gain further insight into the effect of molecular structure on the whole system, a particle based model is needed. Some models take into account the details of individual atoms but most of the time an intermediate approach is chosen. In this approach groups of atoms are lumped together into pseudo-particles to arrive at a coarse-grained (CG) representation of the system. This approach is also the method of choice in this work.
The chemical structure of phospholipids is illustrated in Figure 4.2. The backbone is the glycerol group to which a hydrophilic headgroup and two hydrophobic hydrocarbon chains are connected. The hydrocarbon chains may vary in length and degree of saturation and belong to a fatty acid. The phospholipids are named according to their attached fatty acids. Here, the unsaturated 1,2-dioleoyl-*sn*-glycero-3-phosphocholine (DOPC) and the saturated 1,2-dipalmitoyl-*sn*-glycero-3-phosphocholine (DPPC) are shown. The attached fatty acids are therefore oleic acid (DOPC) and palmitic acid (DPPC). These lipids are studied extensively in reconstituted lipid bilayers and are typically chosen as examples for unsaturated and saturated phospholipids.

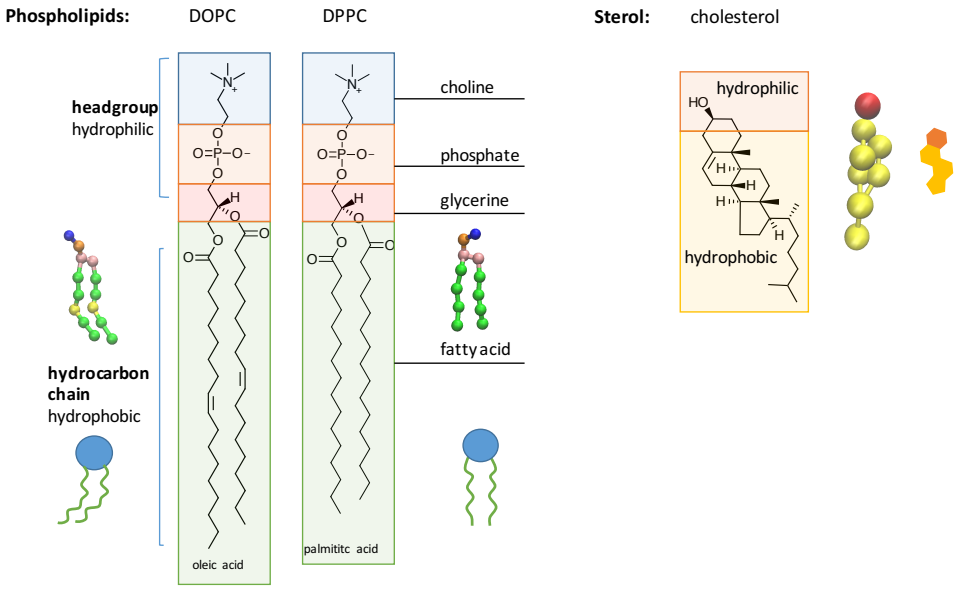

Figure 4.2.: Chemical structures of the unsaturated phosholipid DOPC, the saturated phosholipid DPPC and the sterol cholesterol. The stick models illustrate the coarse-grained representation.

Due to their amphiphilic nature lipids spontaneously self-assemble when dissolved in water in sufficiently high concentration. Depending on their shape they can form different structures such as liposomes, micelles and the lipid bilayer (Figure 4.3). The bilayer has received the most attention in research because it is very much a simplified model of a real membrane and is also the focus of this work. A schematic representation of a one-component lipid bilayer is shown in Figure 4.3 **A**. Here, the phospholipid is saturated and the hydrocarbon chains are therefore straight. This allows a close packing of the lipid tails. In a two-component lipid bilayer, shown in

B, the impact of unsaturated lipids on the packing of the lipid tails is shown. The packing of the lipid tails is disrupted by the unsaturated lipids. This causes an increase in free space and the bilayer gets more permeable. The degree of saturation has also an effect on the elasticity of the bilayer. In general, polyunsaturated chain bilayers are thinner and more flexible than saturated or monounsaturated chain bilayers. The membrane properties are important for the function and survival of cells. Most phospholipids in mammalian cell membranes have saturated or monounsaturated hydrocarbon chains and have therefore a strong, nearly impermeable interface. Only membranes in certain animal tissue like the brain are rich in polyunsaturated phospholipids and therefore "softer" and more permeable. [69, 70]

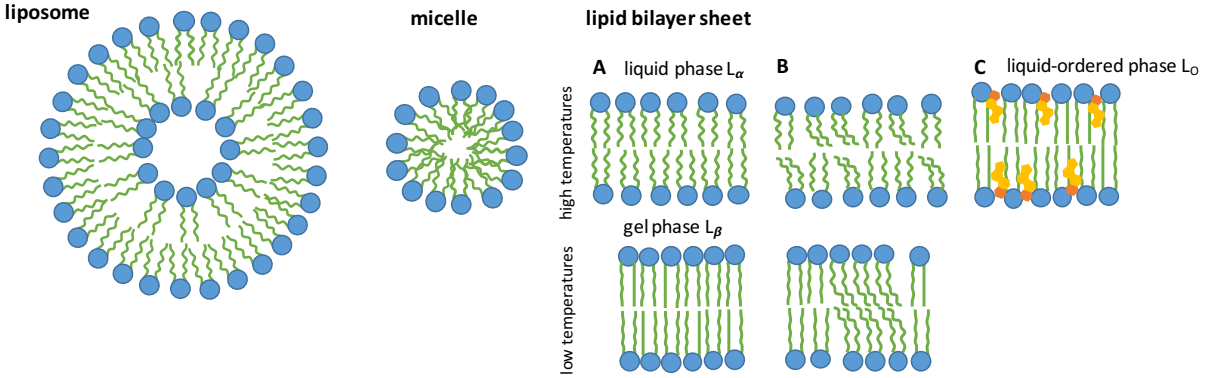

Figure 4.3.: Left: Schematic drawings of the spherical structures liposome and micelle and of lipid bilayers. Right: **A:** Lipid bilayer consisting of only saturated phospholipids: unordered/liquid phase L_α (high temperatures); ordered/gel phase L_β (low temperatures). **B:** Two-component lipid bilayer consisting of saturated and unsaturated lipids. Mixed phase at high temperatures, phase separation at low temperatures. **C:** Illustration of the placement of cholesterol within a lipid bilayer which builds the liquid-ordered phase L_O. [63, 64]

The plasma membrane of mammalian cells contains up to 50 % cholesterol (cf. Figure 4.2 and Figure 4.3 **C**). Cholesterol is important to maintain both structural integrity and fluidity in animal cells and allows animal cells to dispense with a cell wall. Therefore animal cells can change their shape and size and they can move as well due to not being restricted by cell walls. Cholesterol is more rigid than lipids and has a relatively smooth hydrophobic section. The placement of cholesterol within a lipid bilayer is shown in Figure 4.3 **C**. Due its rigid structure it acts like a sheet and increases the order of the phospholipid tails up to 40 % and the liquid-ordered phase L_O is formed. It has therefore a direct impact on the physical properties of lipid bilayers and with that also on the cell biology. [71] Addition of cholesterol to the lipid bilayer decreases the permeability to water [72, 73] and decreases the mobility of lipid tails [74]. Presence of cholesterol increases therefore the mechanical rigidity of lipid bilayers in the fluid state. [75]
A one-component lipid bilayer can exist at a given temperature in two different phases: a liquid phase L_α or a gel (solid) phase L_β (Figure 4.3 **A**). At higher temperatures, the bilayer is in the unordered phase L_α. The lipids can wander across the surface of the membrane. At lower temperatures, the bilayer is in the ordered phase L_β and its lipids are locked in place. Due to the stretched lipid tails, the bilayer thickness is increased and the distance between the headgroups is reduced compared with the fluid phase L_α. The overall packing of the lipids in the bilayer is increased. Two-component bilayers (see Figure 4.3 **B**) undergo a phase separation at lower

temperatures and build gel phases consisting of only one component. The temperature for the liquid-gel transition is dependent on the overall composition of the bilayer.
For one-component bilayers a characteristic transition temperature exists which is influenced by two major aspects: First of all, the length of hydrocarbon chain. Lipids with shorter tails have a lower transition temperature and are also more fluid than lipids with longer chains at a given temperature. Secondly, the degree of saturation. Unsaturated lipid tails prevent a close packing and with increasing degree of unsaturation the transition temperature is lower. [76, 77]
A similar observation can be made in everyday life: butter contains about 70 % saturated fats, thereof approximately 30 % palmitic acid, and is solid at room temperature. [78] On the contrary, olive oil is liquid at room temperature and contains about 80 % oleic acid. [79] The same observation can be made for one-component bilayers consisting of DOPC or DPPC at room temperature. The DOPC bilayer is in the liquid phase L_α ("olive oil") and has a transition temperature of 256 K. The DPPC bilayer is in the gel phase L_β ("butter") and has a transition temperature of 314 K. [80] In order to investigate these reconstituted lipid bilayers and others in the fluid phase, temperatures higher than room temperature have to be chosen. Most reconstituted lipid bilayers are therefore analyzed at 323 K.
In cell membranes the large composition heterogeneity (up to 100 different lipids and even more proteins) assure that the membrane stays in its functional fluid state even at lower temperatures. [81] Nonetheless, ordered domains are believed to be of biological importance, and much experimental effort is devoted to the study of gel domain formation in model lipid systems. [82] An idea is that these gel domains have a high affinity for some proteins and a low affinity for others, thereby contributing to sorting of proteins to their distinct membrane location. [63, 83] The gel domains might also come into play during signaling cascades, if the membrane phase behavior contributes to activation and inactivation of membrane bound enzymatic activities. [83, 84]
In this work one-component and two-component phospholipid bilayers of DPPC and DOPC based on the popular MARTINI model [9] are studied using molecular dynamics (MD) simulations. This widely used approach uses beads to describe lipids and is therefore a CG approach. These beads have different Lennard-Jones type interaction parameters that can smoothly describe hydrophobic and hydrophilic interactions. Even though it is a very simple model it is fairly accurate and can reproduce the properties of self-assembled lipid bilayers. [22, 85, 86] Furthermore, it is capable of describing liquid-to-gel transitions of a one-component DPPC bilayer [82] but fails to describe the transition for the monounsaturated DOPC. A correct, semi-quantitative description of the phase-temperature behavior is not only crucial to describe the ordered L_β-phase but also for the description of two-component systems and is therefore an important step towards the simulation of biological relevant multicomponent systems. Therefore, the MARTINI DOPC model is modified in section 4.1 and a new, improved DOPC model is presented which is able to describe the liquid-to-gel transition. This new model is acquired by varying angle parameters for the kink which represents the C-C double bond in the lipid chain. Besides the new DOPC model, an extensive study of the angle parameter dependency is presented. Furthermore, a two-component model system consisting of DOPC and DPPC is investigated with respect to the liquid-gel transformation and phase separation.
The so far discussed MARTINI model and other CG models offer a significant speed-up compared to atomistic models. Still, such simulations are computationally very expensive when studying processes on a mesoscopic time ($> \mu$s) and length scales (> 100 nm) and alternative computational models are constantly proposed. Simulation approaches aimed at accessing these long time and length scales are relevant in order to successfully model biological processes. [8, 25] So-called field models offer a whole new approach to simulate soft matter problems at lower computational cost. In the frame of the self-consitent field (SCF) theory, the systems are not represented by

particles but by density fields. This results in a decoupling of the mutual interactions which are now replaced by interaction between the segments and a field. The field is based on the spatially inhomogeneous particle density distribution which is determined self-consistently. The molecules are interacting through this field which reduces the amount of data exchange. With the SCF theory numerous systems such as block copolymers [87–90], proteins [91], polymer composites [92] and colloidal particles [93, 94] have been simulated successfully and this method has been shown to be a useful and powerful tool.
In more recent work by Milano, Kawakatsu and De Nicola [10, 21, 25], an SCF approach for phospholipids in the frame of hybrid particle-field MD technique is presented which will from now on be called particle-field (PF) approach. Within this approach the CG martini model is considered as a basis for further approximation. Like with the MARTINI approach, it is possible to simulate the self-assembly of a phospholipid bilayer. The PF approach has been especially parametrized to give a correct representation of the liquid phase L_α at high temperatures ($T = 323\,\mathrm{K}$).
In this work, the temperature behavior of a one-component DPPC system using the PF approach is investigated and the results are presented in section 4.2. Here the dimension of the box are modified in order to get a correct representation of the liquid phase L_α at different temperatures. It is shown, that this approach is capable of describing the liquid phase L_α and its temperature behavior in a physical sensible manner. Furthermore, by modifying the here used PF approach it is also possible to describe the gel phase L_β. The PF approach is therefore capable of describing the important phases L_α and L_β. Another, important phase in mammalian cells is the liquid-ordered phase L_O which is build by the inclusion of cholesterol as pointed out before. This phase has been modeled using different approaches, CG [81] and atomistic [95,96]. In this work the first cholesterol model for the PF approach is presented in section 4.3. With this cholesterol model one can reproduce all important aspects of the liquid-ordered phase L_O.

4.1. Phase transitions in coarse-grained saturated and unsaturated phospholipid models

In this section one-component and two-component systems of the phopholipids DPPC and DOPC are studied with respect to their liquid-gel transition using MD simulations. As a starting point, the MARTINI model [9], which is primarily parametrized to represent lipids in the liquid phase L_α, is used. The mapping and the bonded parameters of these lipids are illustrated in Figure 4.4.

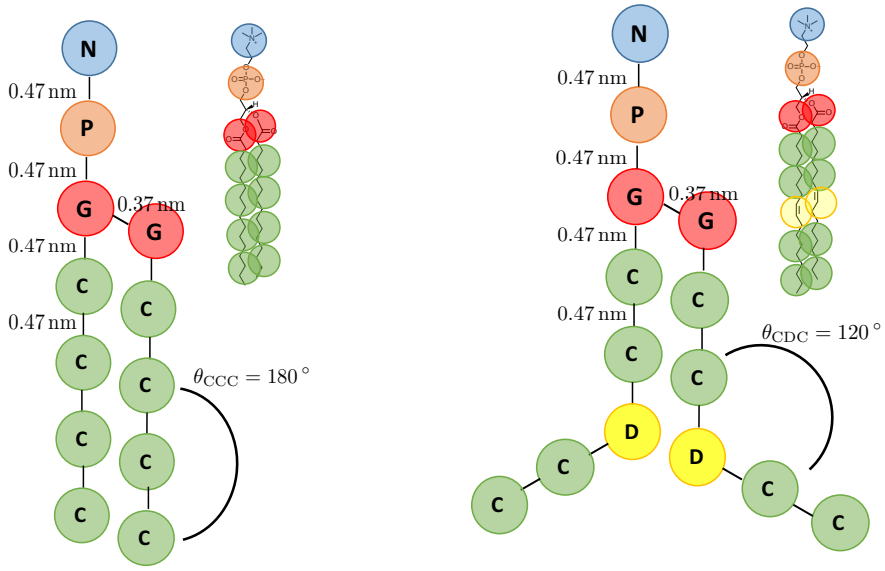

(a) DPPC (b) DOPC

Figure 4.4.: Sketch of the mapping and the bonded parameters of the coarse-grained lipids DPPC and DOPC according to the MARTINI model. [9]

In section 4.1.1 the liquid-gel transition of a one-component system consisting of DPPC (Figure 4.4 (a)) is studied. This section serves as an introduction to the setup of the simulations. Furthermore, the important physical quantities for describing the phase transition are introduced. This liquid-gel transition using the MARTINI model of DPPC was already extensively studied in [82].
In section 4.1.2, the liquid-gel transition for the MARTINI model of DOPC (Figure 4.4 (b)) is investigated. The unsaturated C-C double bond produces a kink in the hydrocarbon chain. This is shown in the standard MARTINI model by an equilibrium angle of $\theta_{CDC} = 120\,^\circ$ and by a force constant of $K_{CDC} = 45\,\mathrm{kJ/mol}$. The here used angle potentials are cosine based: $U_{\mathrm{angle}}(\theta_{CDC}) = \frac{1}{2}K_{CDC}(\cos(\angle CDC) - \cos(\theta_{CDC}))^2$ with the angles $\angle CDC$ and θ_{CDC} given in $^\circ$ and the force constant K_{CDC} given in $\mathrm{kJ/mol}$. The angle parameters, θ_{CDC} and K_{CDC}, are varied in this work in order to match the transition temperature in a semi-quantitative agreement with the experimental data ($T_{\mathrm{trans}}^{\mathrm{exp}} = 256\,\mathrm{K}$ [80]). Furthermore, the influence of the angle parameters on the transition temperature is carefully examined.
Lastly, a two-component system consisting of DPPC and DOPC is investigated in section 4.1.3. Again, the angle parameters θ_{CDC} and K_{CDC} are varied. Besides investigating only the liquid-gel transition, also the ability to describe a phase separation (cf. Figure 4.3 **B**) is examined.

4.1.1. Gel phase formation in DPPC

The MARTINI model of DPPC is known to undergo a liquid-gel transition from the fluid or liquid-crystalline phase L_α to the gel phase L_β when cooled. [82] To induce a phase transition a well equilibrated system is quenched to a lower temperature. The initial temperature is $T = 323\,\mathrm{K}$ like for most simulations of reconstituted bilayers. Therefore the starting temperature is well above the transition temperature reported for the same system in [82] of $T_{\mathrm{trans}} = 295 \pm 5\,\mathrm{K}$.
Two DPPC bilayer systems were simulated: a small patch, consisting of 128 lipids, and a large patch, consisting of 1152 lipids. This is done to rule out system size-effects [97,98] and to validate the use of the smaller system. The usage of the smaller system is highly beneficial because it allows to probe many different temperatures at a reduced computational cost. Further computational details are documented in App. C.1. In Figure 4.5, a snapshot of the big bilayer patch is shown. The blue square illustrates the size of the small bilayer patch.

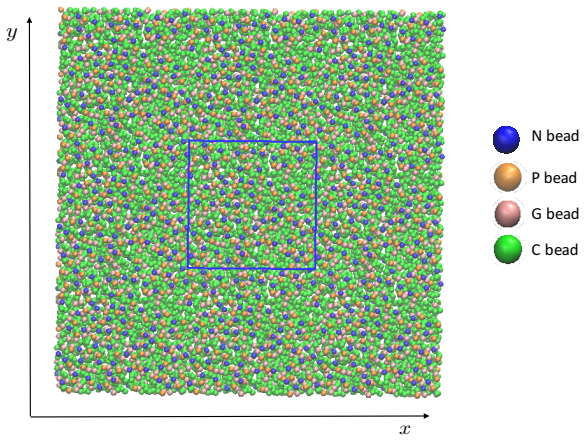

Figure 4.5.: Snapshot of the bilayer surface of a one-component system consisting of DPPC. The total number of lipids is 1152. The blue square marks the size of the small system which only consists of 128 lipids. The legend on the right shows the different beads.

As a solvent the MARTINI water model was used in two different modifications. The standard MARTINI water model "W" represents four H_2O-molecules as a sphere and has the tendency to freeze too easily. Therefore, 20 % of the standard MARTINI water model W was replaced with the slightly bigger MARTINI water model "WF" as "anti-freeze" to prevent freezing of the water. Although the WF particles are bigger in size, they still only represent four water molecules. The level of hydration for both simulated systems, small and big, was 62.5 H_2O per lipid which corresponds to 15.63 CG water spheres per lipid.
In Figure 4.3 **A** a schematic drawing of the liquid phase L_α and the gel phase L_β is shown. Here, it is pointed out that the phase L_β differs from the phase L_α by the following points:

1. the lipid tails are almost fully extended with a few gauche defects remaining
2. the area per lipid is lower
3. the lateral mobility is strongly reduced. [82]

These points are now further illustrated and physically measurable quantities are introduced.

1. Extension of the lipid tails In Figure 4.6 two snapshots of the small DPPC bilayer patch (128 lipids) at $T = 323\,\mathrm{K}$ (fluid phase, L_α, **A**) and $T = 240\,\mathrm{K}$ (gel phase, L_β, **B**) are shown. It is clearly visible that the lipid tails are almost fully extended in the gel phase. From the snapshots, it is also visible that the L_β phase is "stretched" in the z-direction. This results in an increase in the bilayer thickness and a decrease in the width of the bilayer patch with respect to the L_α phase. These observations can be characterized by the *order parameter* $\langle P_2 \rangle$, the *measured angle* $\langle \angle \mathrm{CCC} \rangle$ and by the *bilayer thickness* $\Delta d_{\mathrm{P-P}}$.

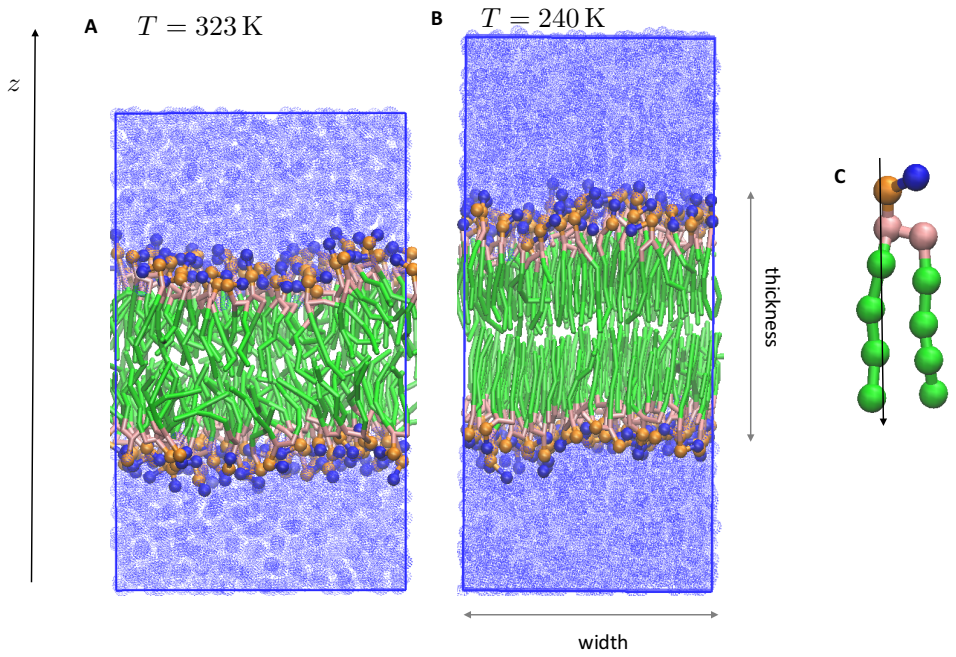

Figure 4.6.: Snapshot of the DPPC bilayer patch at $T = 323\,\mathrm{K}$ (**A**, L_α phase) and $T = 240\,\mathrm{K}$ (**B**, L_β phase). **C:** Single DPPC. The arrow indicates the long molecular axis.

The order parameter $\langle P_2 \rangle$ is given by

$$\langle P_2 \rangle = \frac{1}{2} \left\langle 3 \cos^2 \varphi - 1 \right\rangle \tag{4.1}$$

where φ is the angle between the long molecular axis (see Figure 4.6 **C**) and the preferred direction, which would here be the z direction. The order parameter is an indicator for the order within the bilayer: $\langle P_2 \rangle = 1$ means perfect alignment with the bilayer normal, $\langle P_2 \rangle = -0.5$ anti-alignment, and $\langle P_2 \rangle = 0$ corresponds to a random orientation.
In Figure 4.7 the order parameter $\langle P_2 \rangle$ is shown as a function of the temperature for both investigated system sizes. Note, that the shown temperatures T are the temperatures the system has been quenched to. The obtained values for the big system (red circles) and the small system (black squares) agree for the few selected values of T. This agreement shows, that the smaller, computationally not so demanding bilayer patch is describing the phases L_α and L_β correctly. The order parameter $\langle P_2 \rangle$ exhibits a big step of ≈ 0.17 at around 290 K. This step marks the liquid-to-gel transition.
Another way to measure the "stretch" of the lipid tails is to monitor the angle between different bonds in the lipid tail during a simulation. From the obtained angle distribution at a given temperature the maximum is determined. This value will from now on be called measured angle

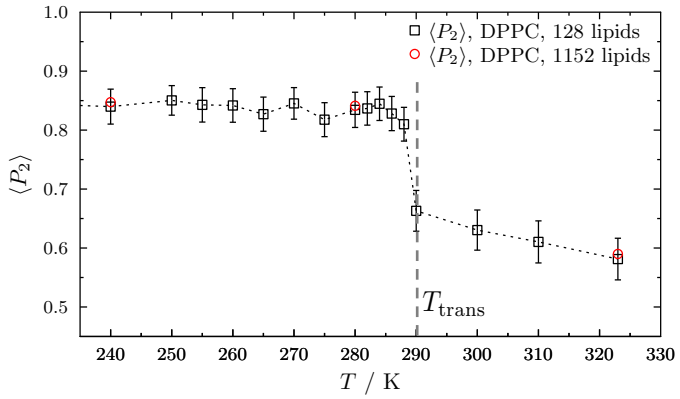

Figure 4.7.: Order parameter $\langle P_2 \rangle$ vs temperature for DPPC. Here, like for all quantities which are shown as a function of the temperature, the temperature T is the temperature the system has been quenched to.

$\langle \angle \mathrm{CCC} \rangle$ and is shown as a function of the temperature in Figure 4.8. Note, that the corresponding equilibrium angle θ_{CCC} is set to 180 ° as shown in Figure 4.4 (a). A big step can be observed at the transition temperature of $\Delta \langle \angle \mathrm{CCC} \rangle \approx 25\,^\circ$ and the angle in the liquid phase L_α is around 145 ° and in the gel phase L_β the value fluctuates around 160 °. This means, that even in the ordered gel phase the lipid tails are not completely stretched. From the observed values one can assume that the preferred CCC-angle in the gel phase is L_β is 160 °.

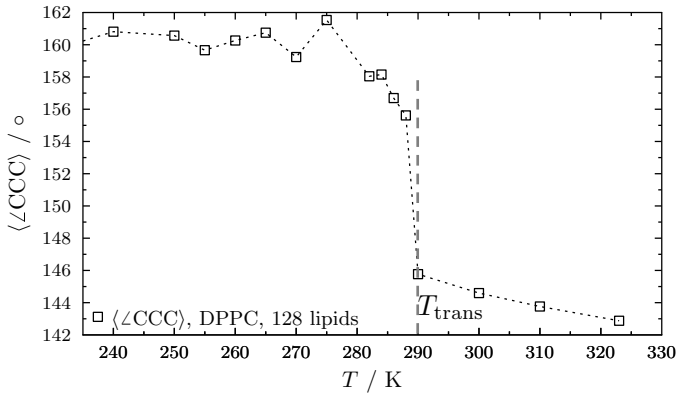

Figure 4.8.: $\langle \angle \mathrm{CCC} \rangle$ as a function of the temperature.

The overall thickness of the bilayer patch is determined via the number density of the P beads (orange beads) along the z-axis, see Figure 4.9 (a). The thickness of the bilayer $\Delta d_{\mathrm{P-P}}$ is the distance of the peaks and shown as a function of the temperature in Figure 4.9 (b). The values for the small bilayer patch and the big bilayer patch agree for the chosen values of T. A large discontinuity of $\approx 0.5\,\mathrm{nm}$ can be observed at the transition temperature $T_{\mathrm{trans}} = 290\,\mathrm{K}$.

2. Area per lipid APL In Figure 4.10 two snapshots of the DPPC bilayer surface at $T = 323\,\mathrm{K}$ (fluid phase) and $T = 240\,\mathrm{K}$ (gel phase) are shown. Here the lateral box lengths in the gel phase

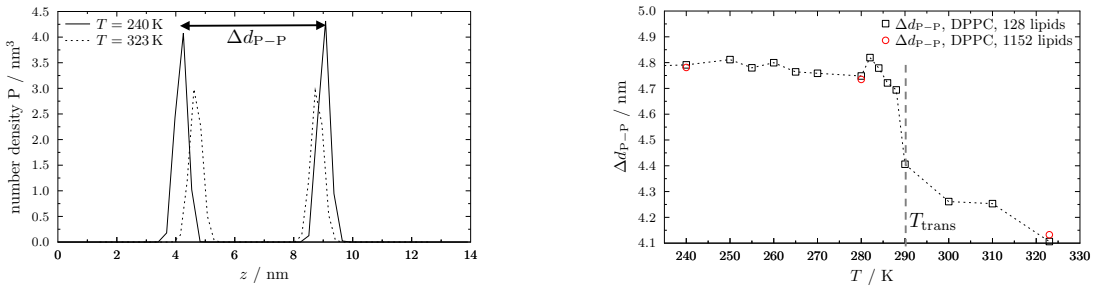

(a) Number density. (b) $\Delta d_{\mathrm{P-P}}$.

Figure 4.9.: (a) Number density of the P beads along the z-axis for $T = 323\,\mathrm{K}$ (dotted line) and $T = 240\,\mathrm{K}$ (solid line). (b) Thickness $\Delta d_{\mathrm{P-P}}$ as a function of temperature.

at $T = 240\,\mathrm{K}$ are 86 % of the lengths in the fluid phase at $T = 323\,\mathrm{K}$. From the knowledge of the box lengths the area per lipid APL can be calculated as

$$\mathrm{APL} = \frac{d_x d_y}{N_{\mathrm{lipid}}/2} \tag{4.2}$$

where d_x and d_y are the lateral box lengths and N_{lipid} is the number of lipids.

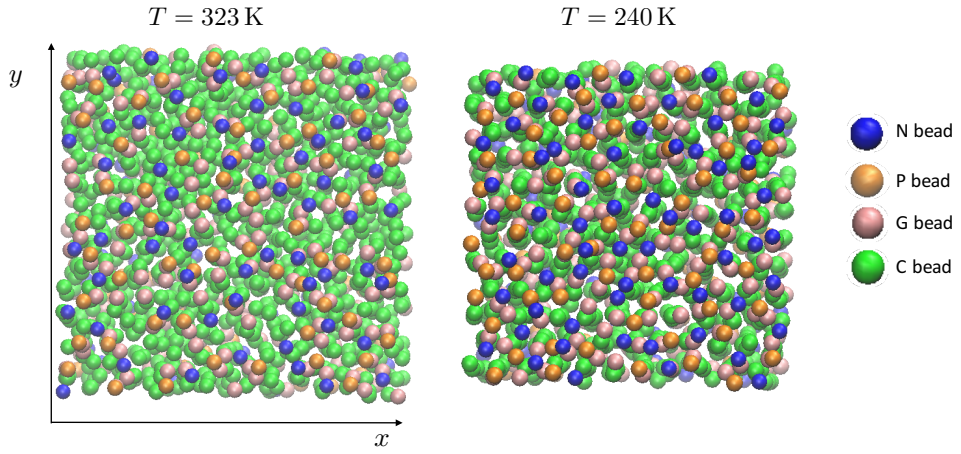

Figure 4.10.: Snapshot of the bilayer surface at $T = 323\,\mathrm{K}$ (fluid phase) and $T = 240\,\mathrm{K}$ (gel phase).

In Figure 4.11 the area per lipid as a function of the temperature is shown. There is a sudden decrease in the APL at the transition temperature $T = 290\,\mathrm{K}$ consistently with a phase transition taking place. This sudden decrease of $\approx 0.8\,\mathrm{nm}^2$ is due to a closer packing of the lipid chains in the gel phase L_β (cf. Figure 4.6). The values obtained for the small and the big system agree well with each other.

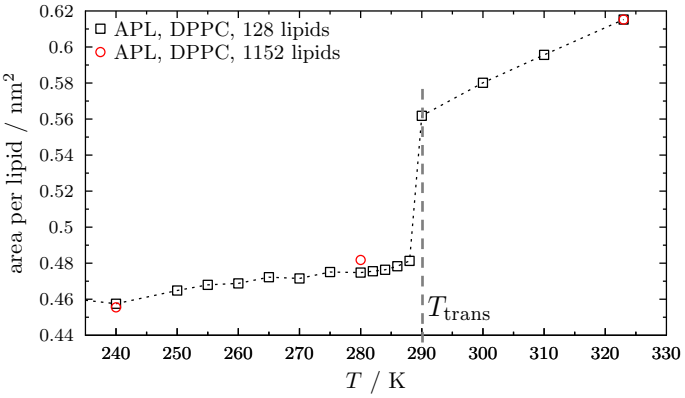

Figure 4.11.: APL vs temperature for DPPC.

3. Lateral mobility Because of their amphiphilic nature, only lateral diffusion is possible in lipid bilayers. The lateral diffusion coefficient D_{xy} gives the degree of lateral mobility. Due to the more rigid structure of the DPPC bilayer at $T < 290\,\mathrm{K}$, one can also observe a jump in the lateral diffusion D_{xy}. The lateral diffusion as a function of the inverse temperature is shown in Figure 4.12. The lipid lateral diffusion rates in the gel phase are on the order of $10^{-9}\,\mathrm{cm}^2/\mathrm{s}$ which is a drop of two orders of magnitude with respect to the fluid phase. Such a drop in the diffusion coefficient marks a phase transition. The here found values for the lateral diffusion rate in the L_α-phase are in semi-quantitative agreement with the experimental values for DPPC: $0.6 - 2 \cdot 10^{-7}\,\mathrm{cm}^2/\mathrm{s}$ between $T = 315\,\mathrm{K}$ and $335\,\mathrm{K}$. [99]

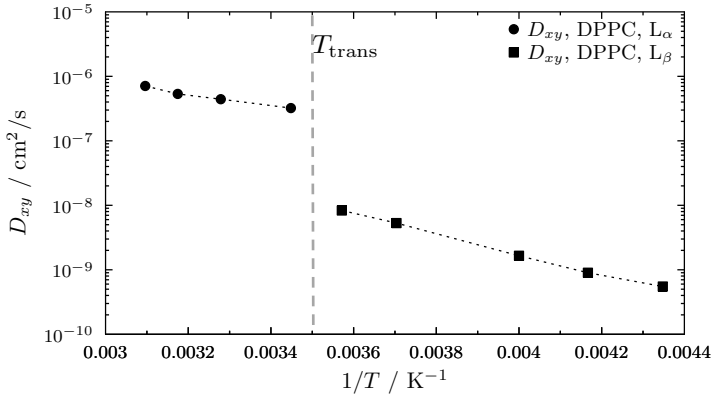

Figure 4.12.: Lateral diffusion D_{xy} of DPPC as a function of $1/T$.

Furthermore, the Arrhenius activation energy for the lipid lateral diffusion can be calculated for both phases by using eq. (2.36). In this way one obtains for the L_α-phase an activation energy of $17.9\,\mathrm{kJ/mol}$ and for the L_β-phase an activation energy of $29.8\,\mathrm{kJ/mol}$. Experimental data [100] reports doubling in the activation energy when going from the liquid L_α-phase ($E_A^{\mathrm{exp}} \approx 21\,\mathrm{kJ/mol}$) to the ordered L_β-phase ($E_A^{\mathrm{exp}} \approx 42\,\mathrm{kJ/mol}$) and the here found data for DPPC one-component system is therefore also in semi-quantitative agreement with this observation.

4.1.2. Gel phase formation in different DOPC models

In this section, the DOPC MARTINI model [9] is studied with respect to its liquid-to-gel transition. Here, the focus is on the kink in the hydrocarbon chain which represents the C-C double bond. The corresponding angular parameters are varied and their influence on the transition temperature is investigated. The bonded parameters are illustrated in Figure 4.4 (b).
The equilibrium angle between the bonds CD and DC in the MARTINI model, θ_{CDC}, is set to $120\,^\circ$ and the force constant for the angular deformation to $K_{\mathrm{CDC}} = 45\,\mathrm{kJ/mol}$. These are also the standard parameters used within the MARTINI force field to describe a single *cis*-unsaturated bond. Similar models, which are based on the MARTINI model, suggest a value of $\theta_{\mathrm{CDC}} = 145\,^\circ$ for the CDC angle in DOPC. [71] Both models were parametrized to describe the liquid phase L_α in a semi-quantitative manner.
The procedure for the setup of the system is analogous the one described in section 4.1.1. Further computational details can be found in App. C.1. To induce the phase transition, a well equilibrated system at $T = 323\,\mathrm{K}$ was quenched to a lower temperature. Again, two different system sizes were investigated: a small bilayer patch with 128 lipids and a big bilayer patch with 1152 lipids. The found values for the order parameter $\langle P_2 \rangle$, the area per lipid APL and bilayer thickness $\Delta d_{\mathrm{P-P}}$ obtained from the big system do agree, like for the one-component system of DPPC, with the values from the smaller system. Therefore only the results for the smaller system are shown in the following.
First, only the equilibrium angle is varied in order to investigate the influence on the transition temperature T_{trans} for the liquid-to-gel transition. Furthermore, the structure of the bilayer in the gel phase is investigated. For these studies the force constant for the angular deformation is set to $K_{\mathrm{CDC}} = 45\,\mathrm{kJ/mol}$ which is the standard value. Secondly, the influence of the force constant K_{CDC} on the transition temperature T_{trans} is investigated. Here again the focus is on the description of the gel phase and its structure.

Variation of the equilibrium angle CDC

In Figure 4.13 snapshots of the different DOPC models at $T = 240\,\mathrm{K}$ are shown. The tested values for the equilibrium angles are $\theta_{\mathrm{CDC}} = 120\,^\circ$ (**A**, standard MARTINI model), $\theta_{\mathrm{CDC}} = 132.5\,^\circ$ (**B**), $\theta_{\mathrm{CDC}} = 138\,^\circ$ (**C**) and $\theta_{\mathrm{CDC}} = 145\,^\circ$ (**D**). The choice of the tested angles is motivated by geometrical reasons: $\theta_{\mathrm{CDC}} = 132.5\,^\circ$ is right in between the equilibrium angles already presented in the literature: $120\,^\circ$ in [9] and $145\,^\circ$ in [71]. Furthermore, $\theta = 138\,^\circ$ is approximately in the middle of $\theta_{\mathrm{CDC}} = 132.5\,^\circ$ and $\theta_{\mathrm{CDC}} = 145\,^\circ$.
For the tested angles one can clearly see that the models with $\theta_{\mathrm{CDC}} \geq 132.5\,^\circ$ (**B, C, D**) are in the ordered gel phase L_β whereas the the standard MARTINI model (**A**) is still in the unordered liquid phase L_α. The DOPC model with $\theta = 132.5\,^\circ$ has a kink in the hydrocarbon chains which describes the unsaturated C-C bond. For higher values of θ_{CDC}, this kinks seems to completely disappear in the gel phase (cf. **C** and **D**). Furthermore, the orientation and form of the lipids in **C** and **D** are rather similar. To validate these observation, a closer look at the physical quantities as described in section 4.1.1 is taken next.

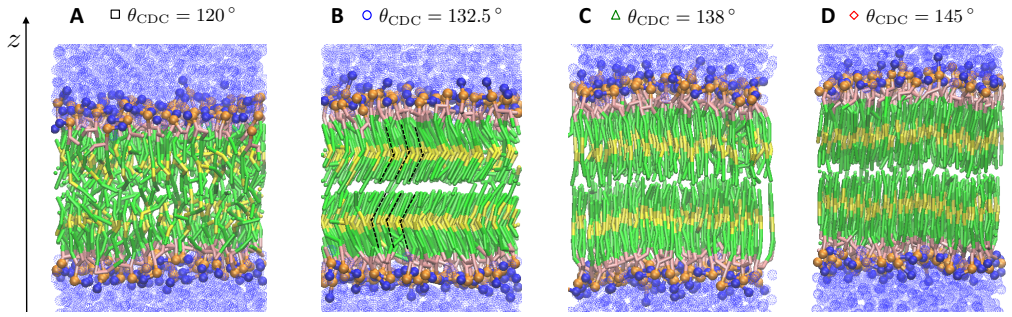

Figure 4.13.: Snapshots of the DOPC bilayer patches at $T = 240\,\mathrm{K}$ for different DOPC models. **A**: Standard MARTINI model for DOPC [9], $\theta_{\mathrm{CDC}} = 120\,°$, **B**: $\theta_{\mathrm{CDC}} = 132.5\,°$, the dotted black lines illustrate the observed kink, **C:** $\theta_{\mathrm{CDC}} = 138\,°$, **D**: $\theta_{\mathrm{CDC}} = 145\,°$ as used in [71]. The force constant for all shown models is $K_{\mathrm{CDC}} = 45\,\mathrm{kJ/mol}$.

In Figure 4.14 the order parameter $\langle P_2 \rangle$ (a) and the area per lipid APL (b) are shown as a function of the temperature T the system has been quenched to. The transition temperatures are determined from the position of the discontinuities of the order parameter $\langle P_2 \rangle$ and the APL. With an increasing angle θ_{CDC} the transition temperature increases and the values are collected in Table 4.3. The APL in the L_α phase is, for a given temperature, higher for a smaller value of θ_{CDC}. This is due to steric effects because small values of θ_{CDC} prevent a close packing of the lipid chains.
Furthermore, one cannot observe a phase transition for the standard MARTINI DOPC model ($\theta_{\mathrm{CDC}} = 120\,°$) from the data shown in Figure 4.14. Even at a temperature of 200 K and simulations times of 50 μs an ordered gel phase could not be observed. This shows the clear limitations of the standard MARTINI DOPC model of describing the gel phase in a semi-quantitative manner. Therefore, the here performed variation of the θ_{CDC}-angle is a reasonable step towards a CG model of an unsaturated lipid which shows physically correct behavior with respect to the liquid-to-gel transition.

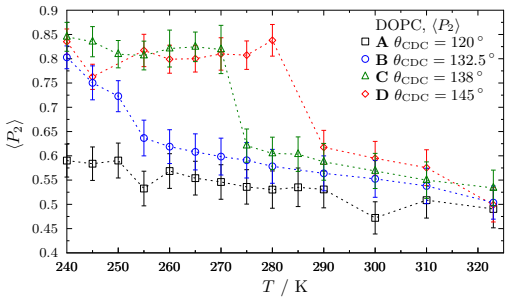

(a) Order parameter $\langle P_2 \rangle$ as a function of T.

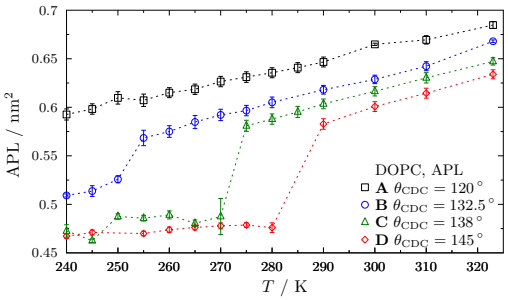

(b) APL as a function of T.

Figure 4.14.: Order parameter $\langle P_2 \rangle$ and APL as a function of the temperature for different θ_{CDC} and $K_\theta = 45\,\mathrm{kJ/mol}$.

Table 4.1.: Equilibrium angle θ_{CDC} and transition temperature T_{trans}.

θ_{CDC} / °	T_{trans} / K
132.5	250
138.0	270
145.0	280

To further investigate the influence of the set equilibrium angle θ_{CDC} on the structure and transition temperature, the measured CDC angle $\langle\angle\mathrm{CDC}\rangle$ is analyzed. In Figure 4.15 (a) $\langle\angle\mathrm{CDC}\rangle$ is shown as a function of T. Furthermore the bilayer thickness $\Delta d_{\mathrm{P-P}}$ is shown in Figure 4.15 (b). Here, one can see that the value of $\langle\angle\mathrm{CDC}\rangle$ is approximately proportional to the thickness $\Delta d_{\mathrm{P-P}}$.

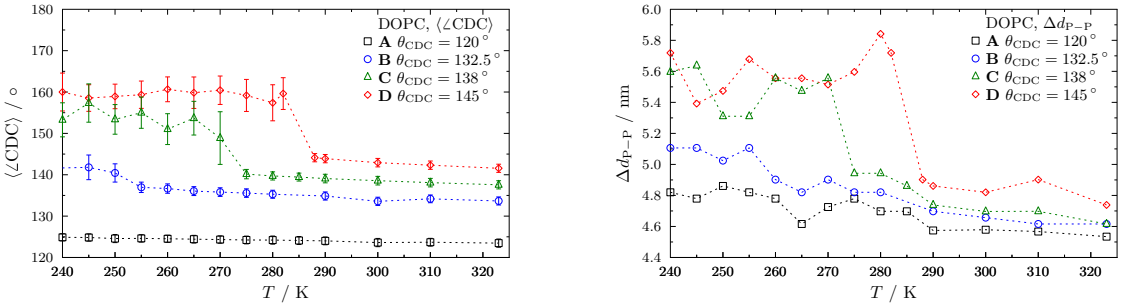

(a) Mean CDC angle $\langle\angle\mathrm{CDC}\rangle$ as a function of the temperature.

(b) Bilayer thickness $\Delta d_{\mathrm{P-P}}$ as a function of the temperature.

Figure 4.15.: Mean CDC angle and bilayer thickness as a function of the temperature for different θ_{CDC} and $K_{\mathrm{CDC}} = 45\,\mathrm{kJ/mol}$.

Jumps in the measured angle $\langle\angle\mathrm{CDC}\rangle$ can also be observed when quenching the system to lower temperatures. In the gel phase the $\langle\angle\mathrm{CDC}\rangle$ angle is significantly higher than in the liquid phase. The DOPC with the highest angle $\theta_{\mathrm{CDC}} = 145\,^\circ$ even reaches $\langle\angle\mathrm{CDC}\rangle = 160\,^\circ$ in the gel phase. For high temperatures $\langle\angle\mathrm{CDC}\rangle$ approaches the set equilibrium angle θ_{CDC}. The bilayer thickness $\Delta d_{\mathrm{P-P}}$ shows according behavior to the observed trends in $\langle P_2\rangle$, APL and $\langle\angle\mathrm{CDC}\rangle$. Here, the jump in thickness is much more pronounced for the higher angles $\theta_{\mathrm{CDC}} = 138\,^\circ$ and $\theta_{\mathrm{CDC}} = 145\,^\circ$. The measured mean angle in the gel phase ranges here from $\approx 150\,^\circ$ to $\approx 160\,^\circ$ which allows closer packing of the lipid chains. This results in a significant increase in $\Delta d_{\mathrm{P-P}}$ of $\approx 1\,\mathrm{nm}$ when undergoing the phase transition.
In conclusion, the DOPC model with an angle of $\theta_{\mathrm{CDC}} = 132.5\,^\circ$ describes the liquid-to-gel transition in a semi-quantitative way. It shows with 250 K the best agreement with the experimental transition temperature of $T_{\mathrm{trans}}^{\mathrm{exp}} = 256\,\mathrm{K}$ [80] of all the tested angles. Furthermore, the transition temperature difference $\Delta T_{\mathrm{trans}}$ between this DOPC model and the MARTINI DPPC model ($T_{\mathrm{trans}}^{\mathrm{DPPC}} = 295 \pm 5\,\mathrm{K}$) is $\approx 45\,\mathrm{K}$ which is consistent with the experimental difference of $\approx 60\,\mathrm{K}$. This agreement is important for the analysis of a two-component system consisting of DOPC and DPPC in section 4.1.3.
Another important aspect is the kink in the lipid tail which should be still pronounced in the gel phase. With a measured angle in the gel phase of $\langle\angle\mathrm{CDC}\rangle \approx 140\,^\circ$ for the DOPC model with $\theta_{\mathrm{CDC}} = 132.5\,^\circ$, this structural property is present for this modified model.

With this slight modification of the CDC angle, the MARTINI DOPC model which was originally parametrized to give a semi-quantitative representation of the liquid phase L_α is now also suitable to describe the liquid-to-gel transition and the gel phase L_β. Note, that the original parameters for the lipid tails in the MARTINI model were parametrized with the help of AA simulations at 323 K. Here, systems of aliphatic fragments were studied as template chains such as *cis*-9-octadecene. This fragment represents the lipid tail of DOPC. [101] Even though a good correspondence between the AA and CG representation was found, it is not surprising that the DOPC MARTINI model is not suitable to describe the complicated process of the liquid-to-gel transition and the gel phase correctly.

Variation of the force constants for the angular deformation of the CDC angle

The influence of the force constant K_{CDC} on the transition temperature is studied next. For these investigations the CDC angle was kept at $\theta_{\mathrm{CDC}} = 132.5\,^\circ$ because it describes the liquid-to-gel transition and the gel phase in a semi-quantitative way as shown above. In Figure 4.16 the order parameter $\langle P_2 \rangle$ and the measured angle $\langle \angle \mathrm{CDC} \rangle$ are shown for the DOPC models with force constants ranging from $40\,\mathrm{kJ/mol}$ to $90\,\mathrm{kJ/mol}$.

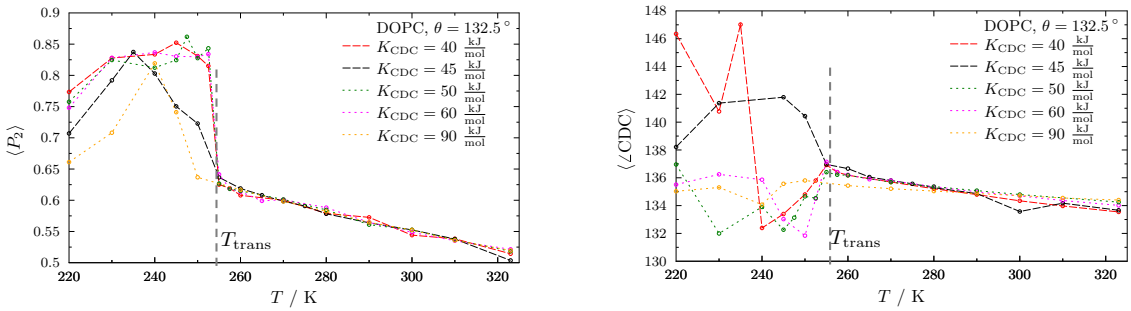

(a) Order parameter $\langle P_2 \rangle$ as a function of the temperature.

(b) Measured angle $\langle \angle \mathrm{CDC} \rangle$ as a function of the temperature.

Figure 4.16.: Order parameter $\langle P_2 \rangle$ and measured angle $\langle \angle \mathrm{CDC} \rangle$ as a function of the temperature.

From the positions of the jumps in Figure 4.16 (a) one can determine the transition temperatures T_{trans}. These are shown in Table 4.2. From the values of T_{trans} and trend of the curves of the order paramter $\langle P_2 \rangle$ as a function of the temperature T one can conclude that T_{trans} is independent of the choice of K_{CDC} in the given range. Only the $\langle P_2 \rangle$ curve for the "hardest" force constant $K_{\mathrm{CDC}} = 90\,\mathrm{kJ/mol}$ and the one for the standard force constant $K_{\mathrm{CDC}} = 45\,\mathrm{kJ/mol}$ differ from the other curves shown here.

Table 4.2.: Angle CDC $\theta_{\mathrm{CDC}} = 132.5\,^\circ$ at different K_{CDC} and their transition temperatures. $T_{\mathrm{trans}}^{\mathrm{DOPC}}$ is the transition temperature for the pure DOPC lipid system.

K_{CDC}/kJ/mol	$T_{\mathrm{trans}}^{\mathrm{DOPC}}$ / K
25	260
40	252.5
45	250
50	252.5
60	252.5
90	250

Even though there are no big changes in the order parameter $\langle P_2 \rangle$, the structure of the DOPC still depends on the different values for K_{CDC}. This is shown in Figure 4.16 (b) for the mean measured angle $\langle \angle \mathrm{CDC} \rangle$. For temperatures $T < T_{\mathrm{trans}}$, the mean measured angle $\langle \angle \mathrm{CDC} \rangle$ for $K_{\mathrm{CDC}} \leq 45\,\mathrm{kJ/mol}$ can be higher than $\langle \angle \mathrm{CDC} \rangle = 137\,^\circ$ which is the found angle at the transition temperature for all K_{CDC}. The $\langle \angle \mathrm{CDC} \rangle$ angles for $K_{\mathrm{CDC}} \geq 50\,\mathrm{kJ/mol}$ are smaller than $137\,^\circ$ for temperatures $T < T_{\mathrm{trans}}$.
One can therefore conclude that the lipid chains for $K_{\mathrm{CDC}} \geq 50\,\mathrm{kJ/mol}$ in the gel phase L_β are bent more than the ones with $K_{\mathrm{CDC}} \leq 45\,\mathrm{kJ/mol}$. This steric effect should have an influence on the packing of the chains and the thickness of the bilayer. For a dense packing of the chains the APL should be comparably small and the thickness $\Delta d_{\mathrm{P-P}}$ larger. In Figure 4.17 the APL and the thickness $\Delta d_{\mathrm{P-P}}$ are shown as function of T. Even though there are a lot of fluctuations, the lowest values in the phase L_β for the APL are found for $K_{\mathrm{CDC}} = 25\,\mathrm{kJ/mol}$ and the highest values for $K_{\mathrm{CDC}} = 90\,\mathrm{kJ/mol}$. The thickness $\Delta d_{\mathrm{P-P}}$ in Figure 4.17 (b) shows according behavior with $K_{\mathrm{CDC}} = 25\,\mathrm{kJ/mol}$ reaching values up to $\approx 5.5\,\mathrm{nm}$ in the ordered phase L_β and for $K_{\mathrm{CDC}} = 90\,\mathrm{kJ/mol}$ only a maximum value of $\approx 5.2\,\mathrm{nm}$. One can clearly see that the found values for $K_{\mathrm{CDC}} = 25\,\mathrm{kJ/mol}$ shows divergent behavior from the other discussed force constants.

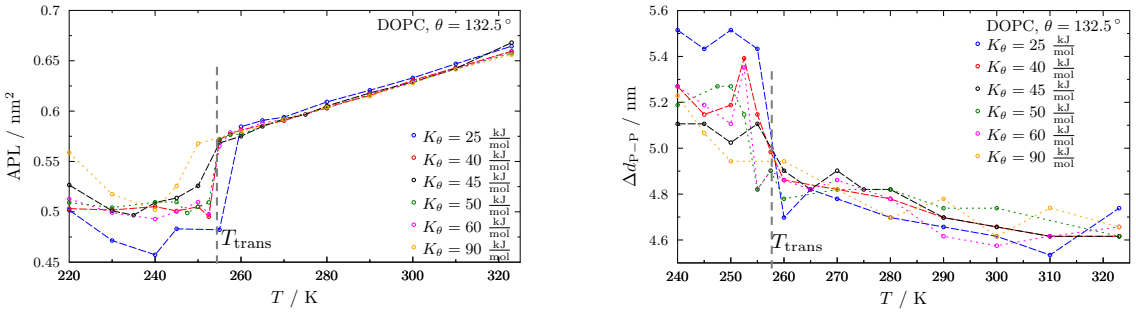

(a) APL as a function of T for different force constants K_{CDC}.

(b) Thickness $\Delta d_{\mathrm{P-P}}$ as a function of T for different force constants K_{CDC}.

Figure 4.17.: Area per lipid APL and thickness $\Delta d_{\mathrm{P-P}}$ as a function of the temperature.

For $K_{\mathrm{CDC}} = 25\,\mathrm{kJ/mol}$, the measured quantities $\langle P_2 \rangle$, APL and $\langle \angle \mathrm{CDC} \rangle$ are shown in Figure 4.18. The jump in APL, $\langle P_2 \rangle$ and $\langle \angle \mathrm{CDC} \rangle$ are all well defined at $T_{\mathrm{trans}} = 260\,\mathrm{K}$ which is $\approx 10\,\mathrm{K}$ higher than the transition temperatures observed with the other force constants. The lipid is also more stretched in the gel phase. The $\langle \angle \mathrm{CDC} \rangle$ is here $\approx 158\,^\circ$ and therefore as high as for the DOPC model with $\theta_{\mathrm{CDC}} = 145\,^\circ$ (cf. Figure 4.15 (a). The same angle is also found for $\langle \angle \mathrm{CCC} \rangle$ of the

standard DPPC model in the gel phase L_β (cf. Figure 4.8). Assuming that an angle of 160 ° is the favorable angle in the lipid chains of fully saturated lipid models, one can conclude that a force constant of $K_{CDC} = 25\,\mathrm{kJ/mol}$ is not adequate to correctly describe the unsatured DOPC model in the gel phase.

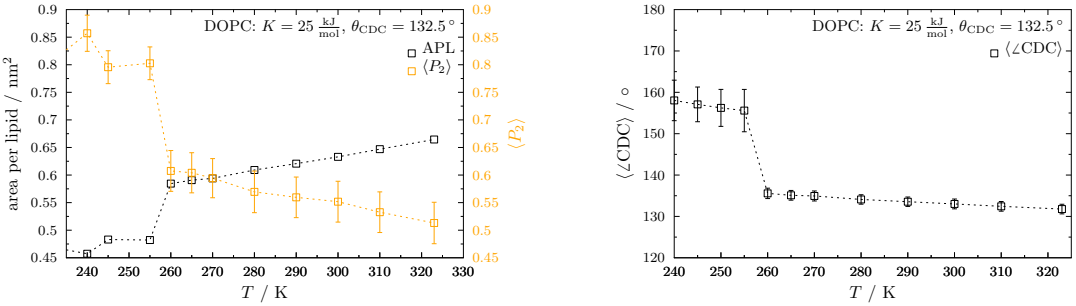

(a) Area per lipid APL and order parameter $\langle P_2 \rangle$ as a function of the temperature.

(b) Mean CDC angle $\langle \angle \mathrm{CDC} \rangle$ as a function of the temperature.

Figure 4.18.: APL, $\langle P_2 \rangle$ and $\langle \angle \mathrm{CDC} \rangle$ as a function of T for the DOPC model with $K_{CDC} = 25\,\frac{kJ}{mol}$ and $\theta_{CDC} = 132.5\,°$.

4.1.3. Phase transitions in DOPC/DPPC mixtures

Membranes in biological systems often consist of a mixture of different lipids which can have different degrees of saturation. [102] In order to study this aspect, systems consisting of a mixture of the unsaturated DOPC and the saturated DPPC were studied. The systems studied here consist of 64 DOPC and 64 DPPC for a total of 128 lipids or of 576 DOPC and 576 DPPC for a total of 1152 lipids. Like for the one-component systems of DOPC and DPPC, the results obtained from the big system consisting of 1152 lipids agree with the results of the smaller system of 128 lipids. Therefore, only the smaller system is showcased here.
Snapshots of different perspectives of the mixture of the small system at different temperatures, $T = 240\,\mathrm{K}$ and $T = 323\,\mathrm{K}$ are shown in Figure 4.19. The upper panel shows side views of the bilayer patch at $T = 323\,\mathrm{K}$ (**A**) and $T = 240\,\mathrm{K}$ (**B**) and in the lower panel the corresponding bilayer surfaces (**C** and **D**) at the given temperatures are shown. The parameters chosen for the CDC angle are $\theta_{CDC} = 132.5\,°$ and $K_{CDC} = 45\,\mathrm{kJ/mol}$.
At $T = 240\,\mathrm{K}$ the system is in the gel phase L_β, while at $T = 323\,\mathrm{K}$ it is in the fluid phase L_α. In the L_β phase no tilt is visible and the lipid chains of DOPC seem to be perfectly stretched. By looking at the bilayer surface of this phase, it is possible to observe that DOPC and DPPC have built patches but the two lipids are still mixed. This observation can be further quantified by counting the neighboring lipids of the same kind. For this kind of analysis for each DPPC the number of neighboring DPPC were counted and averaged. The procedure was repeated for the DOPC lipids accordingly. In this way one finds at $T = 323\,\mathrm{K}$ that each DPPC and each has on average 2.83 neighbors of the same kind of lipid. At a lower temperature of $T = 240\,\mathrm{K}$ one finds higher values for the number of neighboring lipids of the same kind: for DPPC 3.52 and for DOPC 3.58 on average. This increased number at lower temperatures can be taken as an indication that the patches are getting bigger at lower temperatures. In order to exclude system size effects, the same analysis was performed for the bigger system (576 DOPC and 576 DPPC)

and the here found values for the averaged numbers of neighbors for both kind of lipids at both temperature agree with the found values for the smaller system.

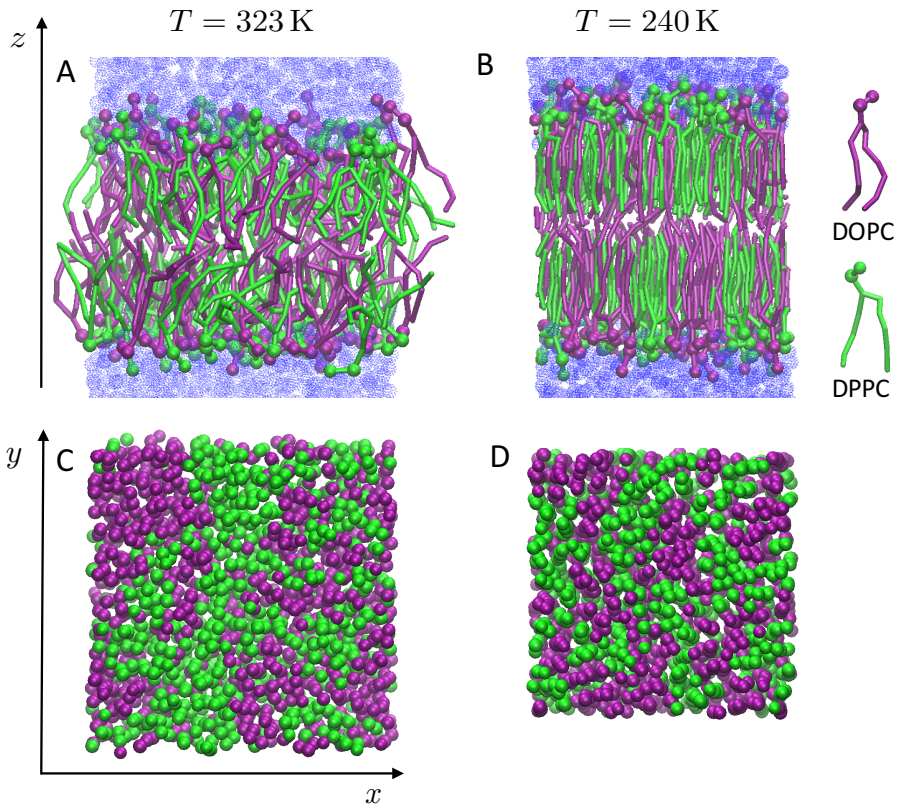

Figure 4.19.: Snapshots of the DOPC/DPPC system for different temperatures. The different kinds of lipids are color coded, DOPC is shown in purple and DPPC in green. Upper panel: Side view on the bilayer patches at different temperatures. **A:** $T = 323\,\mathrm{K}$ and **B:** $T = 240\,\mathrm{K}$. Lower panel: Bilayer surface at different temperatures. **C:** $T = 323\,\mathrm{K}$ and **D:** $T = 240\,\mathrm{K}$. For the CDC angle parameters $\theta_{\mathrm{CDC}} = 132.5\,^\circ$ and $K_{\mathrm{CDC}} = 45\,\mathrm{kJ/mol}$ were chosen.

The influence of DPPC on the structural properties of DOPC and vice versa will be examined next. For this, the angle distribution of all angles were calculated and the maximum was determined. This was done for the pure DPPC system (cf. section 4.1.1), the pure DOPC system (cf. section 4.1.2) and for the mixture of the two lipids. In Figure 4.20 DOPC and DPPC are sketched with the maximum angles found in the distributions for the temperatures $T = 240\,\mathrm{K}$ and $T = 323\,\mathrm{K}$. Here, the black solid lines represent the structure in the two-component system and the grey lines are the structures obtained from the one-component systems.
For DPPC (**A**) the structures are almost identical for the mixed and the pure system at both temperatures. The influence of DOPC on DPPC in the mixed system is therefore not strong. On the contrary, the influence of DPPC on DOPC in the mixed lipid system is much stronger (**B**). Here, a clear difference in the CDC angle can be observed at both temperatures. At 240 K, the CDC angle is far more stretched in the mixed system, while the opposite effect is seen at the higher temperature. A reason for this behavior at high temperatures can be the smaller overall

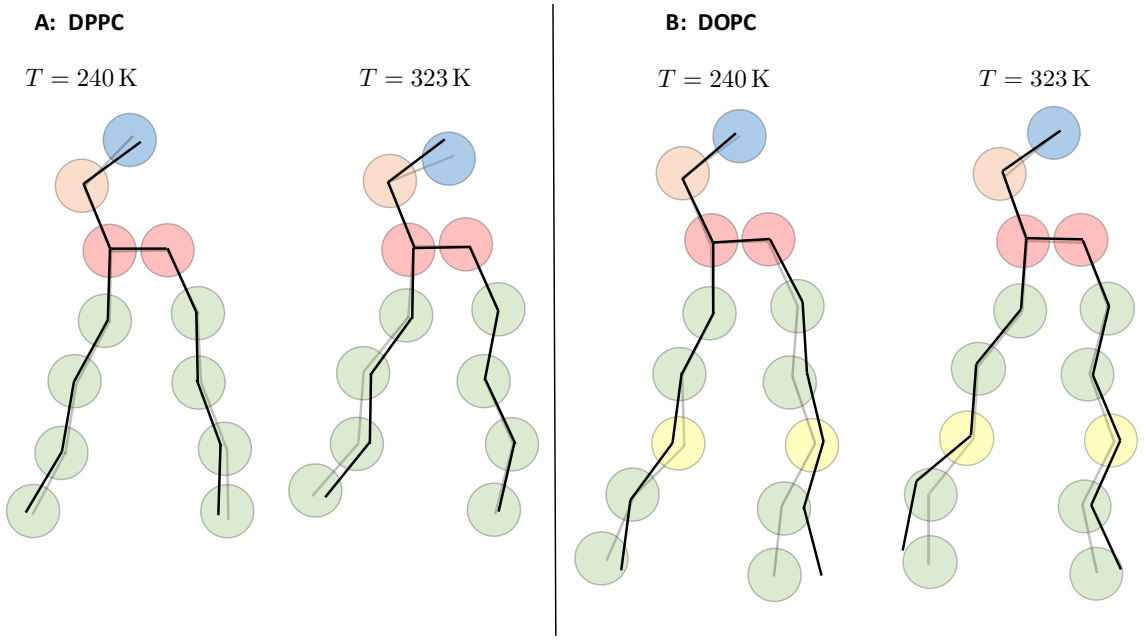

Figure 4.20.: Comparision of the different measured angles for the used DPPC model and the DOPC model ($\theta_{\mathrm{CDC}} = 132.5\,^\circ$ and $K_{\mathrm{CDC}} = 45\,\mathrm{kJ/mol}$). The structure obtained from the two-component system is shown as solid lines and the structure of the lipid in the one-component system is shown as grey lines. **A:** DPPC, $T = 240\,\mathrm{K}$, L_β phase (left) and $T = 323\,\mathrm{K}$, L_α phase (right). **B:** DOPC, $T = 240\,\mathrm{K}$, L_β phase and $T = 323\,\mathrm{K}$, L_α phase (right).

bilayer thickness of the mixed system ($\Delta d_{\mathrm{P-P}} = 4.4\,\mathrm{nm}$) compared to the pure DOPC system ($\Delta d_{\mathrm{P-P}} = 4.7\,\mathrm{nm}$) at $T = 323\,\mathrm{K}$.
Next, the behavior of the CDC and the CCC angles undergoing the liquid-to-gel transition will be analyzed. In Figure 4.21 the measured mean angles $\langle\angle\mathrm{CDC}\rangle$ and $\langle\angle\mathrm{CCC}\rangle$ in the two-component system are shown as full symbols and for comparison the values for the one-component systems are shown as open symbols. The two-component system shows a discontinuity at $T = 265\,\mathrm{K}$ for both angles. The trends of the curves are almost identical but shifted by $\approx 10\,^\circ$. Comparing these curves to the ones for the one-component systems, the strong influence of DPPC on DOPC in the mixture can be clearly seen. The curve form of DPPC is almost identical for both studied systems, with solely the position of the jump being shifted to lower temperatures for the mixed system. On the contrary, the curves for DOPC for the pure and mixed system differ much more especially at low temperatures. A difference of $\approx 10\,^\circ$ can be found. These observation coincide with the ones made for Figure 4.20.
The APL for the mixture and the pure system is shown in Figure 4.22 (a). Here a discontinuity can be seen at $T \approx 270\,\mathrm{K}$ for the two-component system (full symbols). Such a discontinuity is between the transition temperatures for the pure DOPC system ($T_{\mathrm{trans}} = 250\,\mathrm{K}$) and the pure DPPC system ($T_{\mathrm{trans}} = 290\,\mathrm{K}$) (open symbols). The values for the APL of the two-component system are lower than the values for the pure DOPC and higher than the values for the one-component DPPC system at all temperatures. This is consistent with the behavior of the measured mean angles $\langle\angle\mathrm{CXC}\rangle$ shown in Figure 4.21, where DOPC exhibits a larger value of $\langle\angle\mathrm{CDC}\rangle$ in the mixture than in the pure system. This allows a denser packing of the lipid tails and therefore a reduced value of the APL.

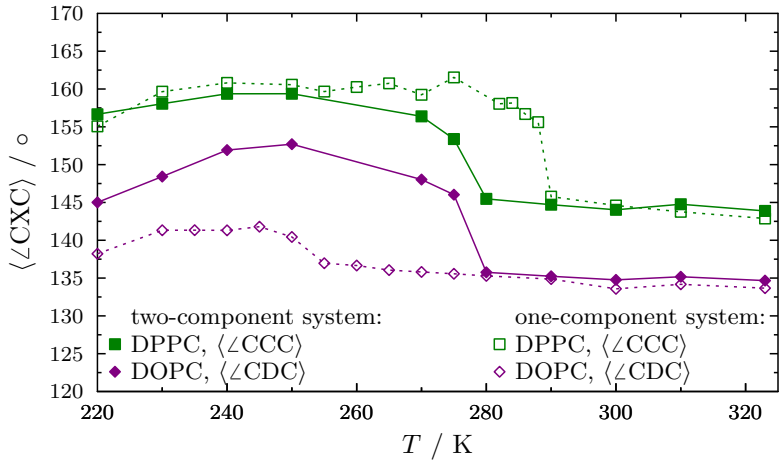

Figure 4.21.: Comparison of the measured mean angle $\langle\angle\mathrm{CXC}\rangle$, X = C, D, of the two-component system and the one component-system as a function of T.

In Figure 4.22 (b) the order parameter $\langle P_2\rangle$ is shown as a function of the temperature for the different systems. A discontinuity at 270 K marks the phase transition in the DOPC/DPPC two-component system. The shape of the curves in the mixed system are almost identical, with the DOPC curve being shifted to lower values of $\langle P_2\rangle$ by ≈ 0.05. Because DPPC and DOPC show a discontinuity at the same temperature and therefore have the same phase transition temperature, one can conclude that this system does not undergo a phase separation which can be observed in experiments. [103]

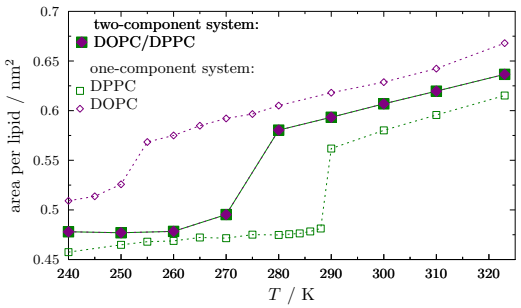

(a) Area per lipid APL as a function of the temperature T.

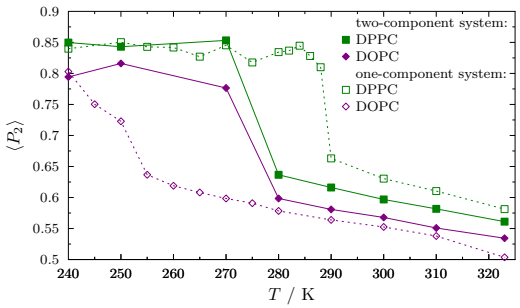

(b) Order parameter $\langle P_2\rangle$ as a function of the temperature T.

Figure 4.22.: Comparision of the APLs (a) and the order paramters (b) found in the two-component system and in the one-component systems.

Next, the influence of the force constant K_{CDC} on the transition temperature T_{trans} in a two-component DPPC/DOPC system will be investigated. Again, force constants ranging from $K_{\mathrm{CDC}} = 25\,\mathrm{kJ/mol}$ to $K_{\mathrm{CDC}} = 90\,\mathrm{kJ/mol}$ were tested (cf. section 4.1.2). The course of the $\langle\angle\mathrm{CDC}\rangle$, APL and $\langle P_2\rangle$ curves (cf. Figure C.1) do not differ much and are in agreement with the ones already discussed for a force constant of $K_{\mathrm{CDC}} = 45\,\mathrm{kJ/mol}$. Therefore also the transition tem-

peratures (see Table 4.3) do not vary much and are fluctuating between 265 K and 270 K. These fluctuations are due to the big steps in temperatures of up to 10 K at which the individual simulations were performed. The transition temperatures for the mixture are ≈ 10 K higher than the ones found for the pure DOPC system (see Table 4.2).

Table 4.3.: Angle CDC $\theta_{\mathrm{CDC}} = 132.5\,^\circ$ at different K_{CDC} and their transition temperatures for a mixed DPPC/DOPC system.

K_{CDC}/kJ/mol	$T_{\mathrm{trans}}^{\mathrm{DPPC/DOPC}}$ / K
25	270
40	265
45	270
50	265
60	270
90	270

Besides the simulation of the small bilayer patches also simulations of the big bilayer patch of 1152 lipids (576 DOPC and 576 DPPC) were performed. At temperatures of 240 K and 260 K and a simulation time of 50 μs no phase separation could be observed. The models here used for DPPC and DOPC are therefore not adequate to describe the phase separation on the μs-time scale.

4.1.4. Conclusion

In this section, different lipid models based on the Martini models for DPPC and DOPC were investigated with respect to the description they provide of the liquid-to-gel transition and the phase separation of a DPPC/DOPC mixture. These phospholipids are the standard examples for a saturated (DPPC) and an unsaturated (DOPC) lipid. In section 4.1.1 the already well studied DPPC Martini model [82] was used to introduce the simulation techniques and the differences between the gel phase L_β and the liquid crystalline phase L_α.
In section 4.1.2, it was shown that the standard DOPC MARTINI model is not able to reproduce the liquid-to-gel transition. In order to solve this problem the properties of DOPC were studied as a function of the various model parameters with a particular focus on the CDC equilibrium angle θ_{CDC} and its associated force constant K_{CDC}. These parameters represent the kink due to the C-C double bond in the hydrocarbon chain. It was shown that with an increasing value of θ_{CDC} the transition temperature is increasing. A value of $\theta_{\mathrm{CDC}} = 132.5\,^\circ$ gives semi-quantitative agreement with the experimental transition temperature.
The phase transition temperature shows little or no dependence on the force constant K_{CDC} in the interval studied ($25 - 90$ kJ/mol). On the contrary, K_{CDC} has a marked effect on the structural properties of DOPC in the gel phase and therefore on the observed kink in the lipid tail. For values $K_{\mathrm{CDC}} \geq 50$ kJ/mol the lipid tails are bent more than for $K_{\mathrm{CDC}} \leq 45$ kJ/mol.
Finally, the liquid-to-gel transition and the phase separation in DPPC/DOPC mixtures was examined in section 4.1.3. Here, a strong influence of DPPC on DOPC in the gel phase L_β was found. The lipid chains of DOPC are stretched due to the influence of DPPC. This results in a denser packing of the lipid chains and in a smaller APL and is accompanied with an increase in the order parameter $\langle P_2 \rangle$. The influence of DPPC on DOPC in the liquid phase is still existent but not as strong as in the gel phase. A variation of the force constant K_{CDC} does not result in a change of the transition temperature nor in the structure of the lipid tails. Mixtures of different

lipids with significantly different T_{trans} are known to undergo phase separation. This could not be observed for the here studied DPPC/DOPC system. The influences of DPPC on the structure of the DOPC model are too strong to adequately describe a phase separation.

4.2. Phase transitions in a coarse-grained saturated phospholipid bilayers using hybrid particle-field methods

In section 4.1 the temperature behavior of reconstituted DPPC and DOPC bilayers were studied extensively using the MARTINI model. Even though this CG approach offers a significant speed up compared to atomistic approaches, these *particle-particle* (PP) simulations are still computationally very expensive when simulating on a mesoscopic scale. A simulation approach accessing these long time and length scales is relevant for a successful modeling strategy of biological processes within a biomembrane. The hybrid *particle-field* (PF) method proposed by Kawakatsu and Milano in [10] for phospholipid bilayers is able to simulate on these scales at low computational cost. Extensive studies of self-assembly and physical behavior of a one-component DPPC system using this approach have already been presented in ref. [10, 21, 25]. In these publications it has been shown that this particle-field based model is suitable to describe the liquid phase L_α. All these studies have been performed at $T = 323\,\mathrm{K}$. In this work, the focus is on the overall temperature behavior and a correct representation of the important phases L_α and L_β at temperatures ranging from $T = 240\,\mathrm{K}$ to $T = 323\,\mathrm{K}$. Besides the PF approach, also the *particle-particle particle-field* (PPPF) is used. This approach can be understood as a refined version of the PF approach as it includes particle-particle interactions.
In order to better understand the differences between the used approaches (PP, PF and PPPF) a short overview over the similarities and the differences between these methods is given next. For the particle-field based approaches PF and PPPF, the intermolecular interactions are described by eq. (2.30). These two methods only differ in the second term for the short-range interactions. The term used to calculate the short-range interactions and a sketch of the used potentials are shown in Figure 4.23. The potentials for the PF approach is $U \propto r^{-1}$ whereas the PPPF approach uses a truncated Lennard-Jones potential. Also the PP approach uses a Lennard-Jones potential but with a larger cut-off. Besides different ways to compute the short-range interactions, the long-range interactions for the particle-field based approaches PF and PPPF are taken into account via a CG density grid (cf. Figure 2.6) whereas the PP approach uses the PME method (cf. Figure 2.3).
To further illustrate the impact of the used potential for the short-range interaction on the structural properties of the DPPC system, the radial distribution function (RDF) given by

$$g_{\mathrm{XY}}(r) = \frac{1}{\langle \rho_{\mathrm{Y}} \rangle_{\mathrm{local}}} \frac{1}{N_{\mathrm{X}}} \sum_{i \in \mathrm{X}}^{N_{\mathrm{X}}} \sum_{i \in \mathrm{Y}}^{N_{\mathrm{Y}}} \frac{\delta(r_{ij} - r)}{4\pi r^2} \tag{4.3}$$

is shown for the different approaches in the lower panel of Figure 4.23. $\langle \rho_{\mathrm{Y}} \rangle_{\mathrm{local}}$ is the particle density of type Y averaged over all spheres around particle X with radius $r_{\max}$. [50] The RDF is a description how the particle density varies as a function of the distance from a reference particle. A major impact on the structure of $g(r)$ has the form of the potential which describes short-range interaction. The RDF $g_{\mathrm{CC}}(r)$ shown in Figure 4.23 is for the C-beads (cf. inlay in the lower right corner in Figure 4.23).
Comparing the RDFs obtained by using the PP and PPPF approach, one can see that these show the same trends. A maximum for both approaches can be found at $r_{\max} = 0.5\,\mathrm{nm}$ and a second maximum at 1.0 nm. The maxima for the PP approach are more pronounced. This due to the fact that not only the repulsive forces up to $r_{\mathrm{cut}} = r_m = \sqrt[6]{2}\sigma = 0.53\,\mathrm{nm}$ with $\sigma = 0.47\,\mathrm{nm}$ are taken into account but also the attractive forces up to a cut-off of 0.9 nm. From the RDF for these approaches one can also conclude that at small distances there is no overlap between the beads because of $g(0) = 0$.

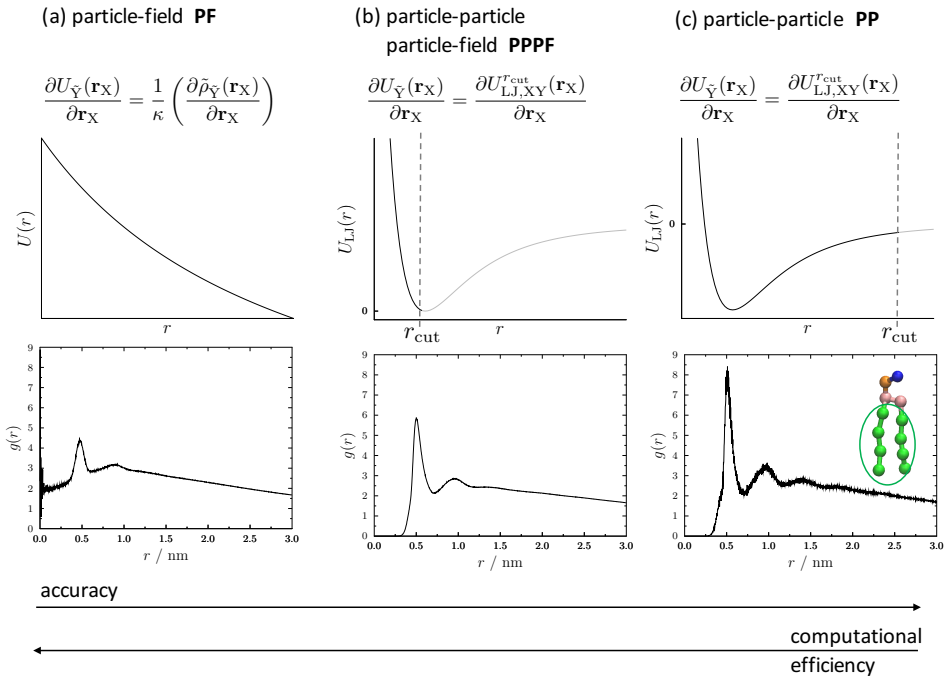

Figure 4.23.: Comparison of the different approaches to calculate the short-range interactions. A sketch of a typical potential is shown in the upper panel and the resulting radial distribution function $g_{CC}(r)$ for the C-beads (marked green beads in the stick model) of DPPC is shown in the lower panel. The radial distribution function $g_{CC}(r)$ are calculated at $T = 323\,\mathrm{K}$.

The result for the RDF of the PF approach looks different. The maximum is shifted to a smaller r-value of 0.47 nm and $g(0) \approx 2$. This non-zero value means that there is a spatial overlap of the beads which is due to the fact that the potential used for the short-range interactions has a much smaller slope than the Lennard-Jones based potentials. Although an overlap is physically not correct, this approach is still valuable due to its ability to describe the liquid phase L_α sufficiently. This chapter is organized as follows. In section 4.2.1, the PF approach is used to investigate the behavior of the the L_α-phase at a large range of temperature. Here, the main focus is on the description this model gives of the area per lipid and the lateral diffusion at various temperatures. Furthermore, the one-component DPPC system is investigated with the PPPF approach in section 4.2.2. Because of its inclusion of particle-particle interaction, this approach is more suitable to describe the ordered phase L_β.
For all simulations using the PF and the PPPF approach the program package OCCAM [10] has been used. Further technical details can be found in App. C.2.

4.2.1. Phase transitions of DPPC using the particle-field approach

In this section, the DPPC model [82] is investigated using the PF approach. Earlier studies of this model by Milano, Kawakatsu and De Nicola [10, 21, 25] using the PF approach are only focusing on the correct representation of the L_α-phase at $T = 323\,\mathrm{K}$. In this work, the DPPC model is studied with respect to its temperature behavior in the range from $T = 240\,\mathrm{K}$ to $T = 323\,\mathrm{K}$. The results of the PP simulation presented in section 4.1.1 are used as a reference. In order to

achieve a good representation of the liquid phase L_α using the PF approach, two major issues have to be solved:
Firstly, reasonable values for the mean field parameters χ_{ij} have to be found. As a basis the Flory-Huggins approach is used, cf. eq. (2.31). The here needed ε-values are taken from the MARTINI force field and the calculated mean field parameters are then further optimized. For bilayer systems, this optimization is done by comparing the number densities along the z-axis of the PF and the PP approach and changing the mean field parameters accordingly.
Secondly, the box size has to be adjusted because only NVT-ensembles can be simulated with the PF approach. As a starting point the box-dimensions obtained by a PP simulation of the same system are used and adjusted in such a way that the bilayer shows no curvature. This means that the APL is changed to a reasonable value. If the bilayer shows micelle-like structure, the APL is chosen too high whereas a wave-like structure indicates a too low APL.
The PF model of DPPC presented in [10] has proven to give a good representation of the liquid phase L_α at 323 K and is used as a starting point for further simulations at lower temperatures. The mean field parameters are shown in Table 4.4. These parameters are calculated using the Flory-Huggins approach as described in section 2.1.4, eq. (2.31).

Table 4.4.: PF interaction matrix for DPPC as described in [10]. The interaction parameter is given in $RT \times (\frac{\text{kJ}}{\text{mol}})$.

χ_{ij}	N	P	G	C	W
N	0.00	-1.50	6.30	9.00	-8.10
P	-1.50	0.00	4.50	13.50	-3.60
G	6.30	4.50	0.00	6.30	4.50
C	9.00	13.50	6.30	0.00	33.75
W	-8.10	-3.60	4.50	33.75	0.00

For a better agreement with the results of the PP approach the mean field parameter χ_{CW} which describes the interactions between the C-beads of the lipid tails and the water beads W has been multiplied by a factor of 2.5. A snapshot of the bilayer patch simulated with the PF approach and the particle density along the z-axis can be found in Figure 4.24.

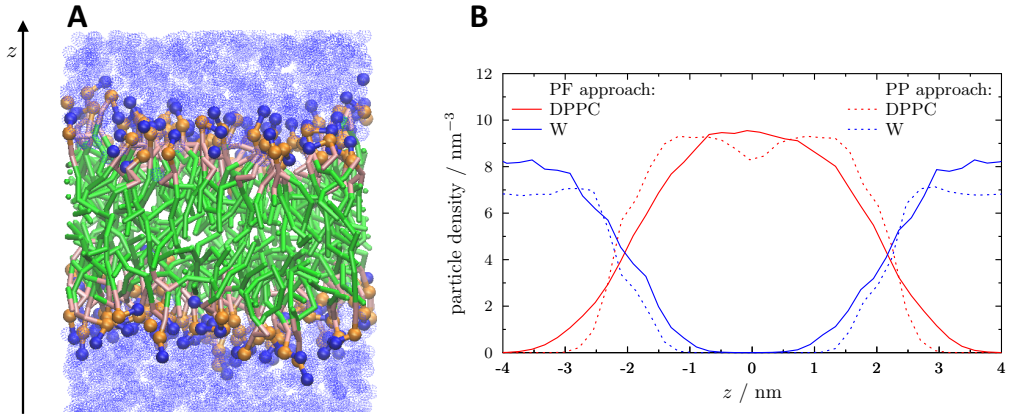

Figure 4.24.: Snapshot of the DPPC bilayer patch simulated with the PF approach (**A**) and particle density as a function of the z-axis (**B**) at $T = 323$ K.

The snapshot **A** can directly be compared with the snapshot shown in Figure 4.6 **A** for the PP approach. The lipids in the PF approach seem to be somewhat more "unordered" than the snapshot of the PP approach. This observation can be easily validated by comparing the number densities of both approaches along the z-axis as shown in Figure 4.24 **B**. The number density of DPPC using the PF is stretched from $z = -4\,\text{nm}$ to $z = 4\,\text{nm}$ whereas the number density of DPPC obtained with PP reaches only from $-3\,\text{nm}$ to $3\,\text{nm}$. Furthermore the number density of W beads reaches further into the lipid bilayer using the PF approach than when using the PP approach. From these observations one can conclude that the PF model gives a weaker phase separation between DPPC and W than the PP approach.
The basic details for the performed simulations are discussed next. More in-depth and technical details can be found in App. C.2. For the here performed PF simulation the APL, and therefore the box dimensions, have to be chosen by hand. As shown in section 4.1.1, a change in the APL is vital to observe a phase transition. In order to overcome this problem three different box sizes and starting configuration at different temperatures were tested:

- APL_1: Box sizes and starting configurations are obtained from a well-equilibrated PP simulation at the same temperature.
- APL_2: Box sizes are obtained by a linear fit of the APL_1-values for $T \geq 290\,\text{K}$. The starting configurations are the same as used for APL_1.
- APL_3: Box sizes and starting configurations are all obtained from a well-equilibrated PP simulation at 290 K.

In Figure 4.25 (a) the different APLs as a function of the temperature are illustrated. Note, that the goal of these simulations is to test the ability of the PF approach to give a physically sensible description of the DPPC bilayer patch at lower temperature and not to determine the correct value for the APL.

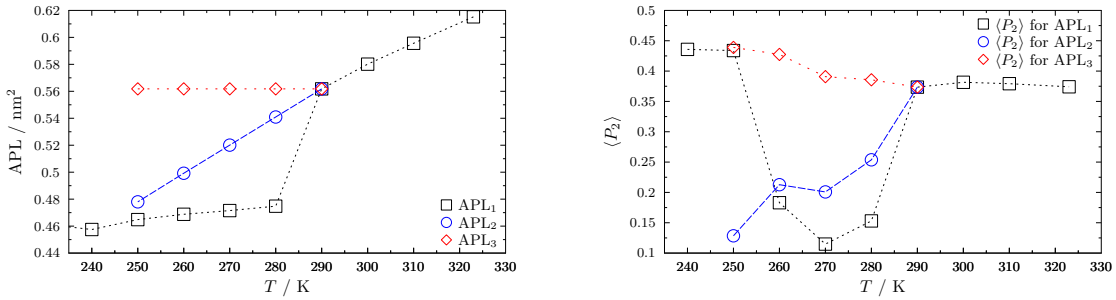

(a) APL vs temperature for DPPC simulated with the PF approach.

(b) Order parameter $\langle P_2 \rangle$ vs temperature for DPPC simulated with the PF approach.

Figure 4.25.: The order parameter $\langle P_2 \rangle$ and the area per lipid APL as a function of temperature.

The order parameter $\langle P_2 \rangle$ as a function of the temperature for the different values of the APL are shown in Figure 4.25 (b). For APL_1 the order parameter $\langle P_2 \rangle$ is at $T \geq 290\,\text{K}$ at around $\langle P_2 \rangle \approx 0.4$. This is much lower than the order parameter for the PP simulations (see Figure 4.7) in this area which ranges from ≈ 0.6 to ≈ 0.7. This due to the fact, that within the PF approach the beads can overlap (cf. Figure 4.23). The amount of overlap is only restricted by the compressibility κ which is here $0.05\,\text{Pa}^{-1}$. The order parameter decreases for APL_1 at

temperatures $T < 290\,\mathrm{K}$. This is due to too little space in the lateral direction. The same also happens for APL_2 at the same temperature, but the curvature is less pronounced due to a higher APL. A snapshot of the simulations at these temperatures can be found in 4.26. For the highest APL at this temperature, APL_3, there is no visible curvature and therefore also $\langle P_2 \rangle$ is at the highest value.

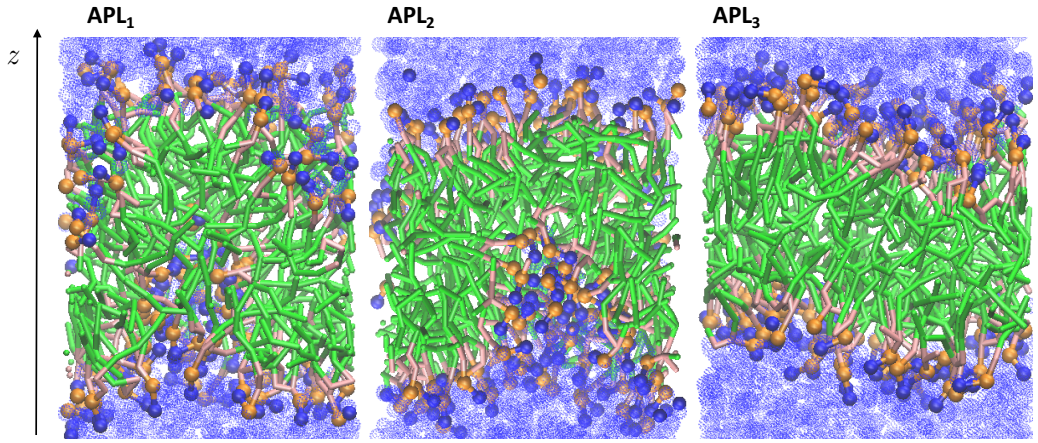

Figure 4.26.: Snapshots of the lipid bilayer at $T = 270\,\mathrm{K}$ for the different APL. For APL_1 and the APL_2 the bilayer shows a curvature due to too less space in the xy directions, for APL_3 almost no curvature of the bilayer can be observed.

The bilayer thickness $\Delta d_{\mathrm{P-P}}$ for the different APL sets is shown in Figure 4.27. For APL_3, $\Delta d_{\mathrm{P-P}}$ is the lowest in the area $250 - 290\,\mathrm{K}$ because there is no curvature in the bilayer. For APL_1 and APL_2 there is a step increase in the bilayer thickness at 290 K which is due to the curvature and not caused by a stretch in the lipid tails (cf. order parameter in Figure 4.25 (b)).

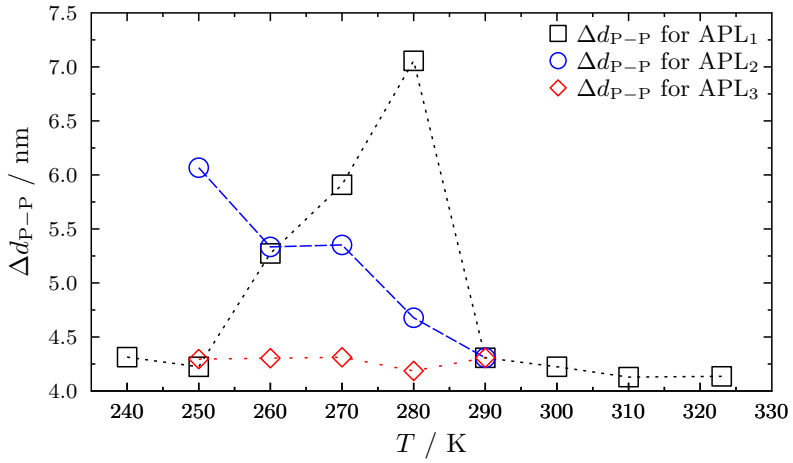

Figure 4.27.: Bilayer thickness $\Delta d_{\mathrm{P-P}}$ as a function of the temperature for the different APL.

Conclusion One can conclude, that a combination of APL_1 for $T \geq 290\,\mathrm{K}$ and APL_3 for $T < 290\,\mathrm{K}$ gives the most reasonable results at lower temperatures. Even though a clear phase

transition is not visible as seen in the PP approach, a slight increase in $\langle P_2 \rangle$ and $\Delta d_{\mathrm{P-P}}$ with decreasing temperature can be observed. This physically correct behavior validates the PF approach also for simulations at $T < 323\,\mathrm{K}$. The here used PF approach therefore gives a physically sensible description of the L_α-phase whereas it fails to describe the L_β-phase. This failure of describing the L_β-phase could be a matter of the chosen box size: for incorrect box parameters the APL is incorrect and therefore a transition to the higher ordered L_β-phase is not visible. On the other side one could also say that the here chosen approach for describing the short-range interaction is too coarse and the level of resolution too low. Especially the possible spatial overlap between different beads in the PF approach could be a big hindrance in describing the L_β-phase. In order to include "stronger" short-range interactions, the PPPF approach (see Figure 4.23 (b)) is tested in section 4.2.2.

4.2.2. Phase transitions of DPPC using the particle-particle particle-field approach

In this section, the DPPC one-component system is investigated using the PPPF approach at different temperatures. Here the focus is on the description of the phase transition and the overall temperature behavior. The PPPF approach is a combination of the PF and the PP approach and is illustrated in Figure 4.23 (b).
In Figure 4.28 the mixed resolution scheme for all performed simulations is presented. The intermolecular interactions of the water beads W are described by the PF approach whereas the intermolecular interactions within the lipid bilayer are described by the PF approach. This means that the DPPC lipids are described at a higher resolution than the water beads. The interaction between the solvent beads W and the lipids are described by the PF approach.

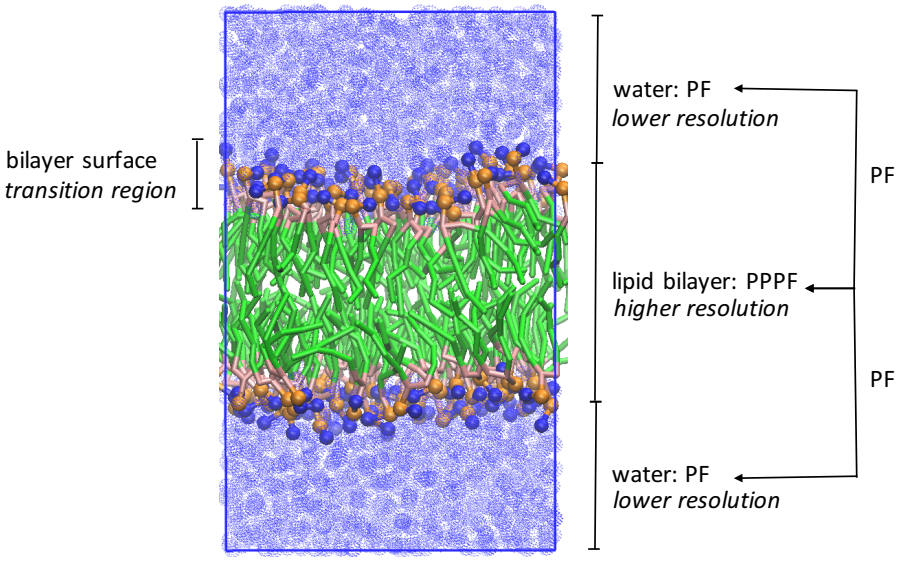

Figure 4.28.: Snapshot to illustrate the mixed resolution scheme in the one-component DPPC system. The intermolecular interaction between the water beads are described via the PF approach whereas the intermolecular interactions in the lipid bilayer are described via the PPPF approach. The interactions between water–lipid bilayer are described using the PF approach.

A common problem of simulations at different resolution levels is the description of the interaction between these levels especially in the transition region, here the bilayer surface. A stable and correct description of the bilayer surface is necessary in order to describe the whole system in a sensible manner. As a reference for a stable lipid bilayer surface the results of the PP approach are considered and furthermore compared with the results of the PF approach. Within the PP approach the bilayer surface is stabilized by several hydration shells. This can be visualized with the help of the RDF between the P beads of the lipids and the W beads, see Figure 4.29.

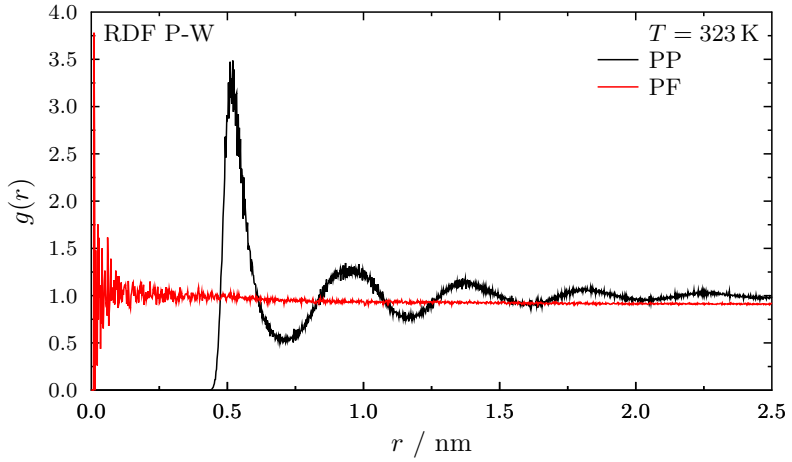

Figure 4.29.: Comparision of the P–W RDF obtained with the PP and PF approach at $T = 323\,\mathrm{K}$.

From the well pronounced structure of the RDF (PP approach) in Figure 4.29 one can conclude that each P bead is neatly surrounded by W beads. This extra layer of W beads around each P bead prevents the lipid heads to move too close to each other and results in an equal distribution of the lipid heads over the whole bilayer surface which is a characteristic of a stable lipid surface. Looking at the RDF obtained with the PF approach one can clearly see that the P and W beads do spatially overlap ($g(0) \neq 0$). Furthermore, there are no peaks within the shown RDF and therefore the W beads are not surrounding the P beads in a well structured manner as in the PP approach. The hydration shell around the lipid heads is therefore not described in a physical sensible way by the PF approach which can lead to an unstable description of the bilayer surface. This is due to the fact that the interaction within the bilayer described by particle-particle interaction are "stronger" than the particle-field interactions.
In order to overcome this problem for the here chosen PPPF approach, the intermolecular interactions of the lipids have to be adjusted so that they build a stable surface. In this work two different parameter sets to achieve this kind of distribution were tested:

1. In parameter set **PPPF(1)** the bilayer surface is stabilized via an increased effective bead size σ of the P and N beads of the head group. In this way, the beads are restricted in their movement and locked in place.

2. Parameter set **PPPF(2**) aims at increasing the overall structural integrity of the bilayer. This is done by increasing the attractive interactions of the C beads within the lipid tails by a slightly reduced the effective bead size σ and an increased depth of the potential given by the ε-value.

The values for these parameter sets can be found in Figure 4.30 (left panel). The varied parameters are the cut-off distance r_{cut}, the effective bead size σ and the depth of the Lennard-Jones potential ε. Next, the bilayer surface using these parameter sets at two different temperatures is investigated.

Bilayer surface

Figure 4.30 shows snapshots of the resulting bilayer surfaces at $T = 323\,\text{K}$ and $T = 240\,\text{K}$ for the two parameter sets PPPF(1) and PPPF(2). For comparison, snapshots at the same temperatures of stable bilayer surfaces obtained with the PP approach can be found in Figure 4.10.

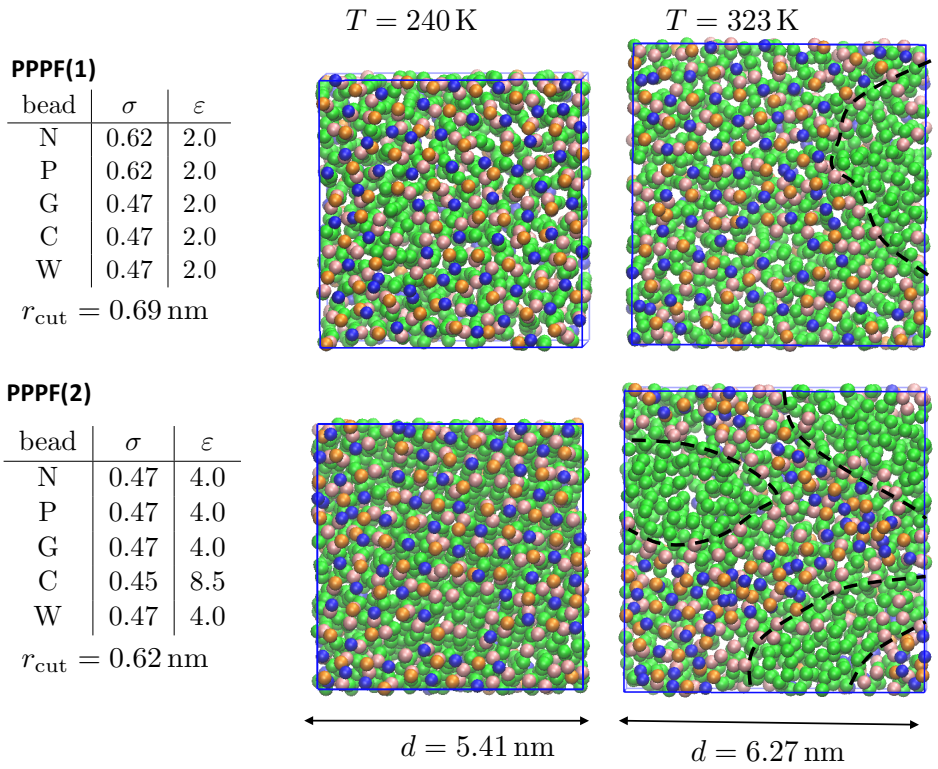

Figure 4.30.: Comparasion of the bilayer surface at different for the different parameter sets PPPF(1) and PPPF(2). The used non-bonded parameters and the cut-off are listed in the right panel (σ in nm and ε in kJ/mol). Snapshot of the bilayer surfaces at $T = 240\,\text{K}$ are shown in the middle panel and snapshots for $T = 323\,\text{K}$ in the right panel.

For both of the here used parameter sets, PPPF(1) and PPPF(2), there are patches at 323 K in which the lipid heads are aggregated. This results in hydrophobic lipid tail beads C (green beads) being directly at the surface of the bilayer which is marked by black dashed lines in Figure 4.30 (right panel). The area of the patch for the PPPF(1) parameter set is smaller than for PPPF(2). The reason for this difference in the distribution are the different chosen parameters for the head groups. The effective bead size of the beads N and P in the PPPF(1) parameter set is bigger than in the PPPF(2) parameter set and the bilayer surface is therefore stabilized by the short-range interaction of the head beads. The slightly increased aggregation of the head beads using the

PPPF(2) parameter set is therefore due to the small effective bead size of the lipid head beads. As a result, the hydrophobic C beads (green beads) are directly exposed to the water which is not a correct representation of a bilayer surface.
In the middle panel in Figure 4.30 the head beads P and N are evenly distributed over the whole bilayer surface which indicates a stable bilayer. This is due to the chosen length of the box vectors d_x and d_y which are almost 15 % smaller than the ones at $T = 323\,\mathrm{K}$. By choosing this APL smaller the head of the lipids are forced to get much closer together. The here shown bilayer surfaces can directly be compared with the surfaces at $T = 240\,\mathrm{K}$ for the PP approach (cf. Figure 4.10 right panel).

Investigation of the temperature dependence

Next, the temperature dependence of the DPPC system is investigated and the ability of the approaches and parameter sets to describe a phase transition are tested. Here, the focus is on the order parameter $\langle P_2 \rangle$ and the lateral diffusion coefficient D_{xy}.

Order parameter $\langle P_2 \rangle$ In Figure 4.31 the order parameter $\langle P_2 \rangle$ is shown as a function of the temperature T for the different parameter sets PPPF(1) and PPPF(2). For PPPF(1) one can find no signs of a phase transition but a decrease in $\langle P_2 \rangle$ with decreasing T. The parameter set PPPF(2) shows a clear jump in the $\langle P_2 \rangle$-value. From these results one can conclude that only the PPPF approach using the PPPF(2) parameter set is describing the phase transition similar to the PP approach (black squares). The PPPF(1) parameter set fails like the PF approach to describe a phase transition. This could be due to the fact that the lateral movement is too restricted due to the large effective bead size $\sigma_{\mathrm{N,P}} = 0.62\,\mathrm{nm}$.

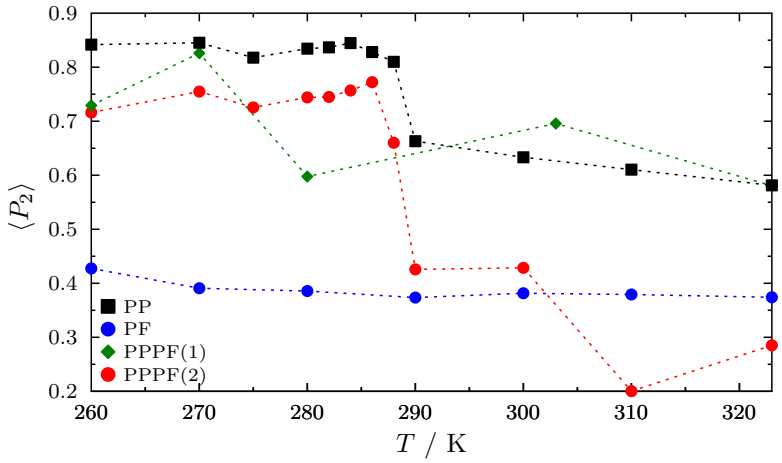

Figure 4.31.: $\langle P_2 \rangle$ as a function of T for the different approaches: PP, PF, PPPF(1) and PPPF(2).

Lateral diffusion coefficient D_{xy} In Figure 4.32 the lateral diffusion coefficient for the different approaches is shown as a function of the inverse temperature. Note, that only for the PP approach a phase transition is visible at $T = 290\,\mathrm{K}$ which is marked by a drop of the lateral diffusion coefficient by two orders of magnitude. The other approaches are therefore not undergoing a phase transition with respect to their lateral diffusion coefficient. Furthermore, their lateral

diffusion coefficient is lower than the one obtained for PP approach. From this one could conclude that the here used PPPF approach is describing the L_β-phase in a reasonable way but fails to describe the L_α-phase.
Still, the D_{xy}-value for the PPPF is steadily decreasing over the here monitored temperature range by two orders of magnitude from approximately $10^{-8}\,\mathrm{cm^2/s}$ to $10^{-10}\,\mathrm{cm^2/s}$. Furthermore a change in the slope can be observed around $T = 290\,\mathrm{K}$ ($1/T = 0.035\,\mathrm{K^{-1}}$) which indicates a changes in the activation energy E_A. The curves for the PPPF(1) and PPPF(2) approach only differ slightly and no real trend can be observed. The different activation energies E_A for the different approaches are shown in Table 4.5. As already stated in section 4.1.1, the activation energy is doubling for a transition from L_α- to L_β-phase which can be observed for the PPPF(2) approach. For the PPPF(1) parameter set a tripling of the E_A-value can be observed.

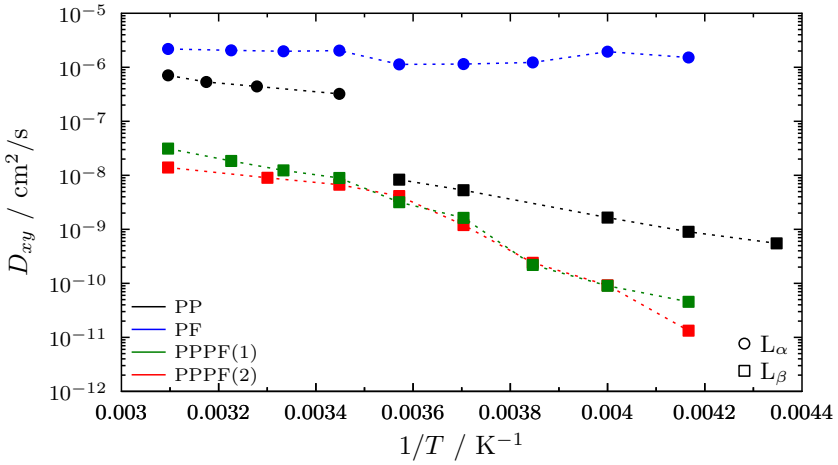

Figure 4.32.: Lateral diffusion coefficients D_{xy} as a function of the inverse temperature $1/T$ for the different approaches: PP, PF, PPPF(1) and PPPF(2).

Table 4.5.: Activation energy E_A for the lateral diffusion coefficients for different temperature ranges: $T \geq 290\,\mathrm{K}$ (L_α) and $T < 290\,\mathrm{K}$ (L_β).

approach	L_α: E_A / kJ/mol	L_β: E_A / kJ/mol
PP	17.89	29.84
PF	3.08	-
PPPF(1)	24.34	70.54
PPPF(2)	29.74	63.32

Conclusion One can conclude, that the here chosen PPPF approach with the PPPF(2) parameter set is describing the gel-phase L_β in a reasonable fashion. The results for the order parameter and the diffusion coefficient at low temperatures $T \leq 290\,\mathrm{K}$ are comparable with the much more precise and computational more expensive PP approach. The here proposed PPPF is therefore an important step towards mesoscale simulations of lipid bilayers at low temperatures in the gel phase.

4.2.3. Conclusion

In this section two different approaches to simulate a DPPC system at temperatures $T \leq 323\,\mathrm{K}$ were presented: the PF approach (cf. section 4.2.1) and the PPPF approach (cf. section 4.2.2). These approaches consider the CG MARTINI model of DPPC (section 4.1.1) as a basis for further approximations. Both approaches replace the long-range particle-particle interaction with interactions with a field and are therefore less accurate but also the computational cost is reduced. Furthermore the short-range particle-particle interactions are replaced by interactions with a particle density (PF approach) or by a truncated Lennard-Jones potential (PPPF approach).
The two particle-field approaches PF and PPPF were tested with respect to the description they give of the lipid bilayer at different temperatures. As a reference the results of the PP approach were taken.
The PP approach is able do describe the DPPC bilayer over a large range of temperatures and also describes the liquid and the gel phase in a physically correct manner. Therefore this approach is also able to describe the phase transition $\mathrm{L}_\alpha \rightarrow \mathrm{L}_\beta$ (cf. Table 4.6).
The PF approach is able to describe a stable bilayer surface over a wide range of temperatures. At lower temperatures the bilayer surface is still stable, i.e., the lipid heads are still equally distributed over the surface, but there is no jump in the area per lipid which would indicate the more ordered gel phase. The other physical properties such as the lateral diffusion coefficient D_{xy} and the order parameter $\langle P_2 \rangle$ are indicating the existence of a L_α phase over the tested range of temperatures. Furthermore, the PF approach fails to describe the gel phase L_β. These results are also visualized in Table 4.6.

Table 4.6.: Summary of the results of the simulated DPPC system using the different approaches PP, PF and PPPF. For a good description of the phase (L_α, L_β) with respect to the inspected property (surface, D_{xy}, $\langle P_2 \rangle$) the cell is colored green, for a bad description red and for a satisfying, yet not good description, orange.

	PP		PF		PPPF(1)		PPPF(2)	
bilayer surface	L_α	L_β	L_α	L_β	L_α	L_β	L_α	L_β
lateral diffusion D_{xy}	L_α	L_β	L_α	L_β	L_α	L_β	L_α	L_β
order parameter $\langle P_2 \rangle$	L_α	L_β	L_α	L_β	L_α	L_β	L_α	L_β

For the PPPF approach two different parameter sets were tested: PPPF(1) and PPPF(2). Here, a special focus is on the bilayer surface which acts as an interface between two levels of resolution: the DPPC bilayer which is described at a higher resolution with the PPPF approach and the water beads W which are described at a lower resolution with the PF approach. The DPPC bilayer and the surrounding water beads are are interacting via the PF approach.
Both parameter sets were investigated thoroughly at a large range of temperatures with respect to their phase behavior. Only the parameter set PPPF(2) is able to describe the L_β phase with respect to the investigated properties (see Table 4.6).
From these results one can conclude that even though the particle-field based approaches PF and PPPF do not describe the phase transition of the DPPC bilayer, they still are important and interesting approaches due to their ability to describe the liquid phase L_α (PF approach) and the gel phase L_β (PPPF). These two phases are important for the description of biological membranes. Because of the significant speed-up of particle-field based approaches, they are an important step towards simulations of membranes on a mesoscopic scale.

4.3. Cholesterol model for hybrid particle-field molecular dynamics simulations

In the previous section it was shown that the particle-field approaches PF and PPPF are suitable to describe the phases L_α and L_β at various temperatures. Besides the liquid phase L_α and the ordered gel phase L_β, the liquid-ordered phase L_O which is formed in the presence of cholesterol (CHOL) plays an important role in biomembranes of mammals. The liquid-ordered phase can be understood as a combination of the L_α- and L_β-phase: the packing of the lipids is increased (similar to the gel phase) while maintaining a high lateral diffusion coefficient (similar to the liquid phase). In order to reproduce the L_O-phase with the PF approach, a cholesterol (CHOL) model for this method is needed.
In this section, the development of such a model and the properties of the resulting L_O-phase are discussed. As a starting point the improved MARTINI model of cholesterol [71] was used. Its mapping is shown in Figure 4.33 **A** and further details about the bonded and the constraint parameters can be found in App. C.6. Figure 4.33 **B** shows the definition of the long molecular axis of the cholesterol model. The CG model of cholesterol shown here is fairly rigid, only the the C2 bead which represents the alkane chain is able to move more freely.

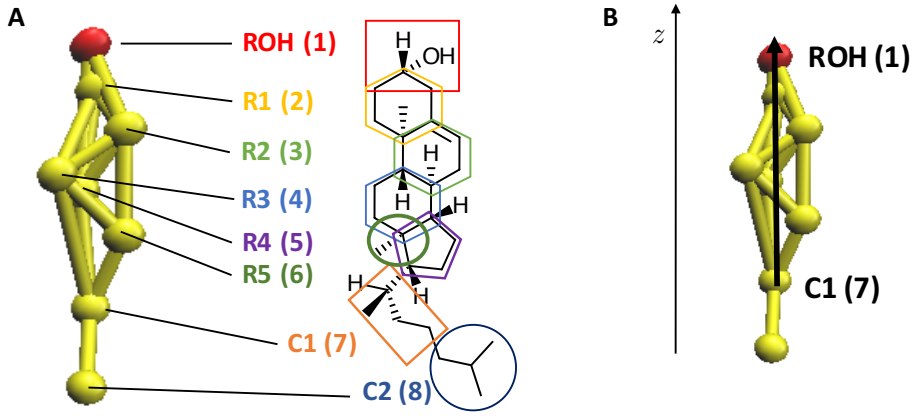

Figure 4.33.: **A:** Mapping of the cholesterol according to [71]. In the stick models the defined bonds and the constraints are shown. **B:** Long molecular axis of the cholesterol model.

For introductionary purposes a system consisting of DPPC and cholesterol is studied with the PP approach in section 4.3.1. Such systems using the PP approach are already studied extensively in [9, 104, 105]. Here the methods to characterize the L_O-phase in a DPPC/CHOL system are introduced. Based on these results a newly parametrized cholesterol model for the PF approach is presented in section 4.3.2.

4.3.1. Liquid-ordered phase simulated with the PP approach

The results of a PP simulation of a system consisting of 128 DPPC and 32 cholesterol (CHOL) are discussed in this section. The simulation was performed at 323 K and further computational details can be found in App. C.1. A snapshot of the bilayer patch is shown in Figure 4.34 **A** which can be directly compared with the snapshot of the DPPC system (L_α-phase) shown in Figure 4.6. In the DPPC/CHOL system the lipids are more stretched and the system is in the

liquid-ordered phase L_O (cf. Figure 4.3 **C**). In order to better understand the difference between the liquid-ordered phase L_O and the liquid phase L_α it is best to compare the order parameter $\langle P_2 \rangle$ and the lateral diffusion coefficient D_{xy} of these two phases:

- **Order parameter $\langle P_2 \rangle$:** For the order parameter of the DPPC system (L_α-phase) presented in section 4.1.1 one gets a value of 0.58 whereas for the DPPC/CHOL system (L_O-phase) the order parameter is 0.66 and is therefore increased by 0.08. The $\langle P_2 \rangle$-value in the L_O-phase therefore correspondents to the $\langle P_2 \rangle$-value at 290 K in the L_α-phase of the neat DPPC system.
- **Lateral diffusion coefficient D_{xy}:** For the L_O-phase and the L_α-phase the lateral diffusion coefficient is identical and has a value of $0.07 \pm 0.02 \cdot 10^{-5}\,\mathrm{cm^2/s}$.

This means that even though the order parameter in the L_O-phase is higher than in the L_α-phase at 323 K, both phases have the same lateral diffusion coefficient. For comparison: the lateral diffusion coefficient at $T = 290\,\mathrm{K}$ of the neat DPPC system in the L_α-phase is $0.0214 \pm 0.022 \cdot 10^{-5}\,\mathrm{cm^2/s}$ and therefore more then three times smaller than the lateral diffusion in the L_O-phase. Furthermore, the APL-value of DPPC in the L_O-phase can be approximated using the APL-value of 0.56 nm of the neat DPPC system at $T = 290\,\mathrm{K}$ (see Figure 4.11). With this value, the area per cholesterol can be estimated. The xy-plane of the simulation box has an averaged value of $41.5\,\mathrm{nm^2}$ thereof are $35.904\,\mathrm{nm^2}$ taken by the lipid which yields a total area for the cholesterol of $5.596\,\mathrm{nm^2}$. By assuming that the cholesterol is equally distributed throughout both lipid layers one gets for the area per cholesterol $0.350\,\mathrm{nm^2}$. This is a reasonable result because it is larger than the value for a bead with $\sigma = 0.47\,\mathrm{nm}$. The diameter for such a bead is approximately given by $r_m = \sqrt[6]{2}\sigma = 0.5264\,\mathrm{nm}$ and therefore the area is $\pi(r_m/2)^2 = 0.2176\,\mathrm{nm^2}$.

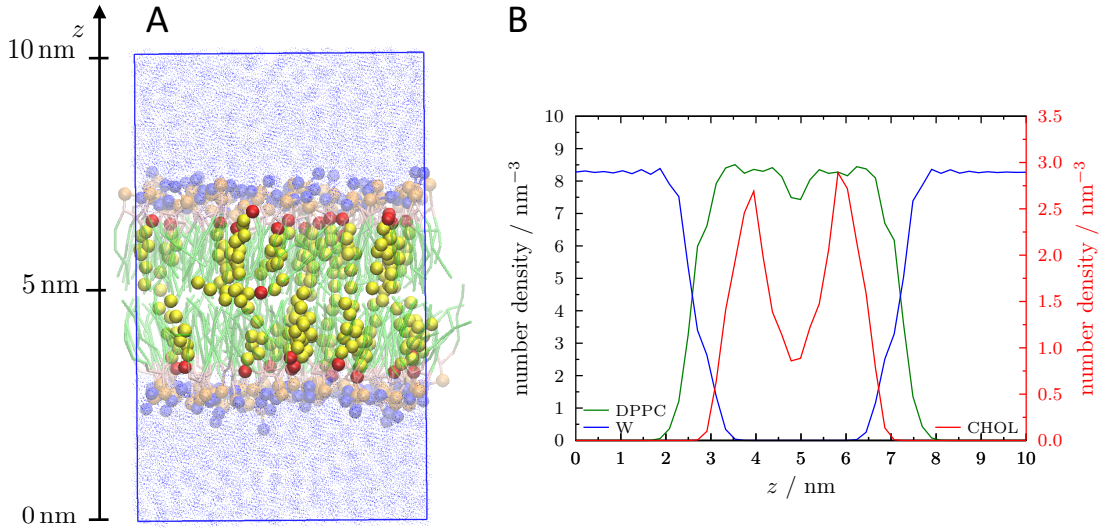

Figure 4.34.: **A:** Side view of bilayer patch consisting of 128 DPPC and 32 cholesterol simulated with the PP approach. The cholesterols are highlighted and colorcoded as in Figure 4.33. **B:** Corresponding number density along the z-axis.

The reason for the special properties of the L_O-phase is the placement of the cholesterol which can also be seen in the snapshot. The cholesterol is positioned within the bilayer in a "sheet"-like fashion and stretches the tails of the neighboring lipids and increasing the short-range order but

allowing lateral movement of the lipids hence the relatively high lateral diffusion coefficient. The polar head-group ROH is positioned right underneath the G-beads of the lipids and the whole cholesterol is aligned along the z-axis. Like for lipids one can calculate an order parameter which is again a measurement of the alignment of the long molecular axis (see Figure 4.33 **B**) along the z-axis. With an order parameter of 0.75 the cholesterol shows a good alignment along the z-axis. In Figure 4.34 **B** the placement of the cholesterol is further illustrated via the number density along the z-axis. Two peaks can be found due to the placement in the upper and lower lipid layer. Between these two peaks the number density is not reaching a value of zero. This is due to the following two reasons: firstly the placement along the z-axis is fluctuating. Secondly one can observe a rather fast flip-flop mechanism of the cholesterol. The approximate time a cholesterol stays in between the two lipid layers during this flip-flop event is 2 ns which is in agreement with the times found for the standard MARTINI cholesterol model as presented in [104]. A cholesterol between the two lipid layers can also be seen in the snapshot **A**. Nonetheless a flip-flop event of a cholesterol is rare and for the here shown DPPC/CHOL system only an approximate number of 15 events could be observed over the course of a 500 ns simulation.

4.3.2. Liquid-ordered phase simulated with the PF approch

In this section a new cholesterol model for the PF approach is presented and its ability to describe the liquid-ordered phase L_O is discussed. As a basis for all simulations, a system consisting of 2000 W and 128 DPPC is used. The development of the cholesterol model is done in two steps: Firstly, the placement of just one cholesterol within the bilayer is investigated using the PF approach. Furthermore the influence of different mean-field parameters χ_{ij} is analyzed and the placement of the cholesterol is adjusted by varying these parameters.
Secondly, 32 of these newly parametrized cholesterols are added to the bilayer. Here the focus is on the question if this new parametrized cholesterol gives a physically sensible representation of the L_O-phase using the PF approach and the results are directly compared with the ones obtained in section 4.3.1 for the PP approach.

1. Placement of cholesterol within the bilayer using the PF approach

The correct placement of one cholesterol within the bilayer is crucial in order to get a physically correct description of the L_O-phase. Using the PF approach, the interactions between different bead types and therefore the placement of certain molecules is heavily influenced by the chosen χ_{ij}-parameters. A first set of χ_{ij}-parameters is calculated using the Flory-Huggins approach eq. (2.31) and is shown in Table 4.8. A snapshot of the system using these calculated χ_{ij}-parameters can be found in Figure 4.35 **A** and the corresponding number density in **B**.
The snapshot and the number density are indicating that the cholesterol is placed in between the bilayer at $z = 5$ nm which is not an accurate description of the placement of cholesterol as discussed in section 4.3.1. For comparison the number density of the cholesterol obtained with the PP approach is shown in **B** as a red dotted line. Furthermore, the cholesterol is not aligned along the z-axis. In order to improve the overall placement and orientation of the cholesterol, the χ-parameters shown in Figure 4.36 are optimized and are marked in the same color in Table 4.8.

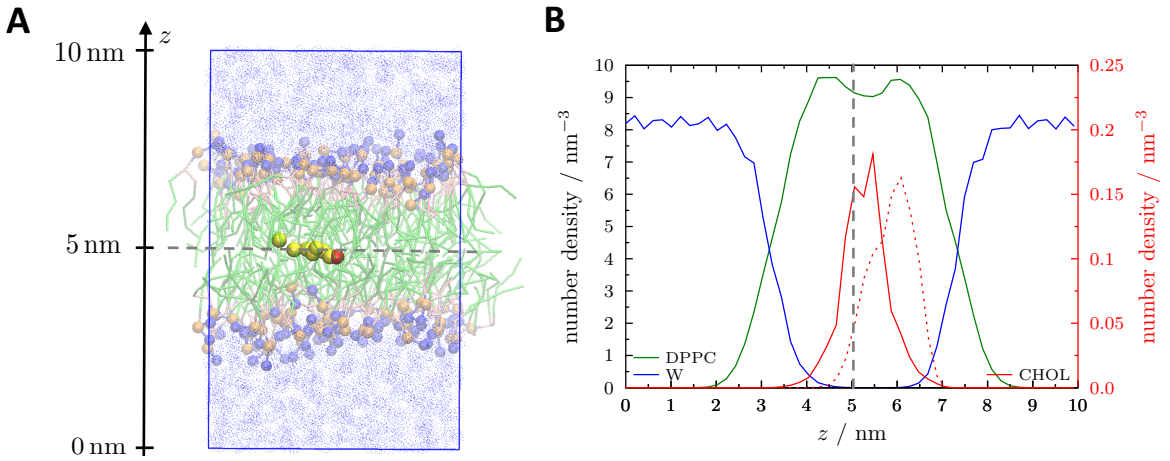

Figure 4.35.: **A:** Snapshot of the system consisting of 128 DPPC and one CHOL simulated with the PF approach. **B:** Number density along the z-axis for DPPC, W and the cholesterol CHOL (solid lines) using the PF approach. For comparision the number density of cholesterol obtained from a simulation of the same system using the PP approach is shown as a red dotted line.

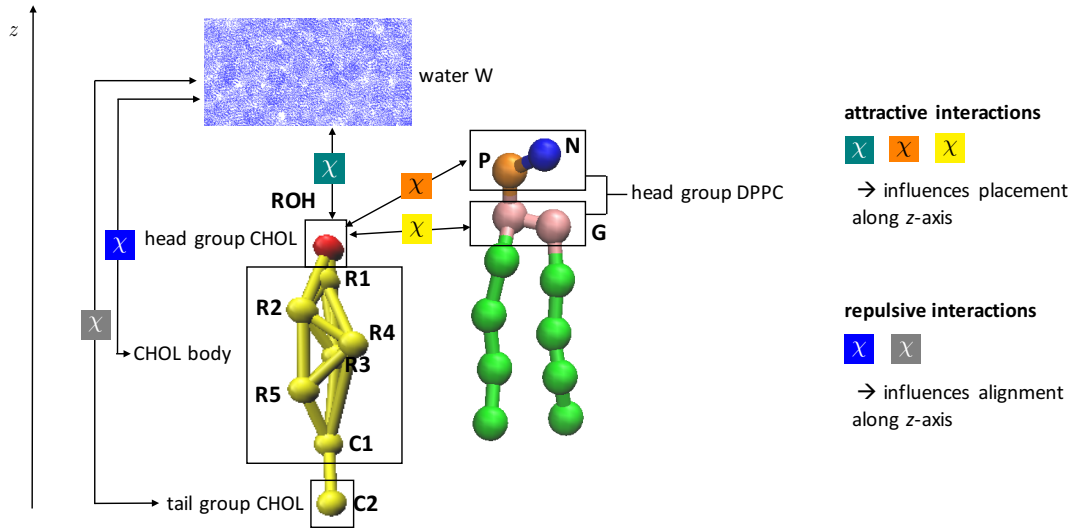

Figure 4.36.: Schematic illustration of the varied χ-paramters.

Note that a positive value of χ describes a repulsive interaction whereas a negative value an attractive interaction (cf. Figure 4.36, right side). Finding the right parameters is a rather complicated procedure because the parameters are heavily dependent on each other. In order to do this systematically the χ-parameters have been multiplied step-wise by a factor. A more in depth discussion of the influences of the different varied χ-parameters can be found in App. C.7. The parameters which give the best placement and orientation of the cholesterol are discussed next.

Attractive interactions By increasing the attractive interactions the placement of the cholesterol along the z-axis is influenced and it is moved nearer to the bilayer surface. In combination with the modified repulsive parameters shown in the next paragraph, the following χ-parameters give the best placement of the cholesterol:

- $\chi \times 5$ and $\chi \times 10$: By increasing the attractive interaction between the ROH-bead and the beads of the head group of lipid, the ROH group is more attracted to these beads and therefore placed nearer to them. A factor of ten for the ROH-G interactions (χ) is placing the ROH-bead nearer to the G beads than to the P and N beads which results in a more accurate description of the placement of the ROH-bead within the bilayer.
- $\chi \times 5$: The attractive interactions between the ROH-bead and the water beads W are increased by a factor of five. In this way the hydrophilic interactions are correctly represented and the head group is again placed nearer to the bilayer surface.

Repulsive interactions By varying the repulsive χ-parameters the alignment along the z-axis is influenced.

- $\chi \times 2.5$: In order to align the cholesterol along the z-axis the hydrophobic interaction between the C2 bead and the water beads was multiplied by 2.5. In this way the tail of the cholesterol is repulsed from the water and in combination with the above chosen parameters for the attractive interactions the cholesterol is aligned along the z-axis.
- $\chi \times 1$: The mean-field parameter for the repulsive interaction of the cholesterol "body" with the water beads were left as they are. Increasing this value would not only increase the alignment along the z-axis but also the "flip-flop" rate (cf. section 4.3.1) beyond a reasonable value.

The resulting number density for the whole cholesterol CHOL along the z-axis is shown in Figure 4.37 and it has an order parameter $\langle P_2 \rangle$ of 0.45. One can see a significant increase of the optimized PF model towards the original PF model. The position of the number densities of the optimized PF model and the PP model do almost agree. The slight broadening and the less pronounced peak of the optimized PF is due the more diffuse bilayer surface in the PF approach. This newly parametrized cholesterol model is therefore placed and positioned within the bilayer similar to the cholesterol model used in the PP approach. In the next section this new cholesterol is analyzed with respect to its description of the L_O-phase using the PF approach.

2. Simulation of the liquid-ordered phase using the PF approach

In order to investigate the new cholesterol model with respect to its description of the liquid-ordered phase L_O, a system consisting of 128 DPPC and 32 CHOL as in section 4.3.1 is analyzed. Computational details of the setup of the simulation can be found in App. C.5.
In Figure 4.38 **A** a snapshot of the DPPC/CHOL system simulated using the PF approach is shown. When comparing this snapshot with the one obtained by using the PP approach (see Figure 4.34) one can see that the lipids and the cholesterol are less ordered than in the system simulated with the PP approach. This reduction in the order is expected when using the PF approach (see Figure 4.23) and can be quantified with the help of the order parameter and directly be compared with the one of the PP approach of section 4.3.1. The obtained values are shown in Table 4.7.

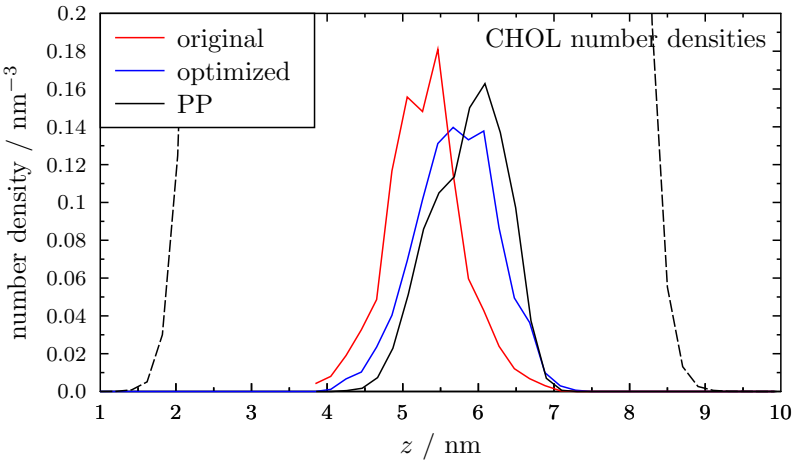

Figure 4.37.: Comparision of the number densities. The black dotted line is the number density of DPPC and is there to visualize the position of the cholesterol.

Table 4.7.: Comparision of the different lateral diffusion D_{xy} and order parameters of the DPPC lipids and cholesterols obtained with different approaches.

approach	system	$D_{xy}/10^{-5}\,\mathrm{cm^2/s}$	$\langle P_2\rangle_{\mathrm{DPPC}}$	$\langle P_2\rangle_{\mathrm{CHOL}}$	phase
PF	128 DPPC, 32 CHOL	0.2153 ± 0.0334	0.53	0.44	L_O
PF	128 DPPC	0.2183 ± 0.0378	0.35	-	L_α
PP	128 DPPC, 32 CHOL	0.0719 ± 0.0173	0.66	0.75	L_O
PP	128 DPPC	0.0709 ± 0.0152	0.58	-	L_α

In Figure 4.38 **B** the number densities for DPPC, W and CHOL along the z-axis are shown. For comparison the number density of cholesterol obtained with the PP approach is shown as a red dotted line. Both approaches show two peaks for CHOL but the one of the PF approach are less pronounced which is due to the character of the interactions in the mean field. One can conclude that the PF approach gives a reasonable description of the placement and orientation of the cholesterols in the bilayer.
Next the DPPC/CHOL system simulated using the PF approach is further investigated with respect to its ability to describe the liquid-ordered phase L_O. All results are compared with the results of the DPPC system and with the results of the PP simulations. The order parameter and the lateral diffusion for both approaches and both systems are shown in Table 4.7.
For the PF approach one can observe a significant increase in the order parameter of the lipid from the DPPC system to the DPPC/CHOL system of 0.18 whereas the lateral diffusion D_{xy} of the lipids stays constant in both system. Such a behavior clearly indicates that the DPPC/CHOL system simulated with the PF approach is in the liquid-ordered phase L_O. Note that the observed $\langle P_2\rangle$-values are lower and the D_{xy}-values are higher in the PF approach than in the PP approach due to the different descriptions of the intermolecular interactions.

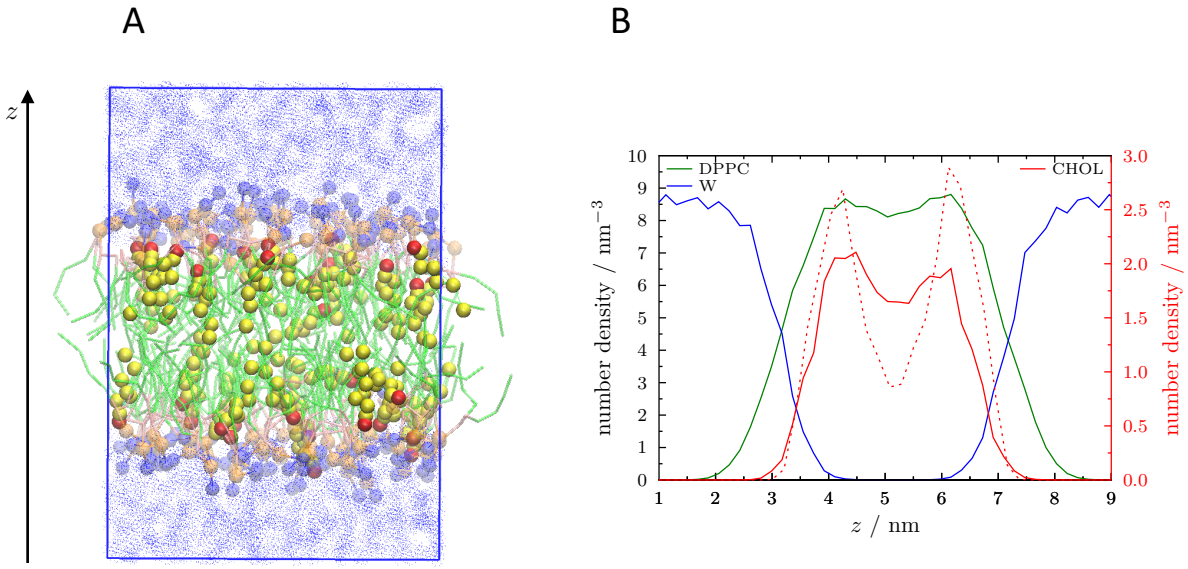

Figure 4.38.: **A:** Side view of bilayer patch consisting of 128 DPPC and 32 cholesterol simulated with the PF approach. **B:** Corresponding number density along the z-axis. For comparision the number density of he PP approach is shown as a dotted red line.

4.3.3. Conclusion

In this section a new cholesterol model for the PF approach based on the improved MARTINI model of [71] was presented and investigated with respect to the description it provides of the liquid-ordered L_O-phase. In order to gain insight into the characteristics of this phase, a system consisting of 128 DPPC and 32 CHOL using the PP approach was discussed first in section 4.3.1. The obtained results were taken as a basis for the parameterization of the cholesterol within the PF approach.
In section 4.3.1 the influences of different mean field parameters χ_{ij} and their impact on the placement of a single cholesterol within the lipid-bilayer were thoroughly discussed. The parameters which agree the most with the placement found using the PP approach were used in order to construct a system with 32 cholesterols and 128 DPPC. In this way a system was obtained which offers a physical sensible description of the L_O-phase. Due to the computational speed-up gained by using the PF approach, this is a big step towards the simulation of bilayer-systems on a mesoscopic scale.

Table 4.8.: Mean field parameters for the DPPC-cholesterol system.

χ_{ij}	N	P	G	C	ROH	R1	R2	R3	R4	R5	C1	C2	W
N	0.000	-1.500	6.300	9.000	-3.375	6.375	4.575	6.375	6.375	6.375	6.375	9.000	-8.100
P	-1.500	0.000	4.500	13.500	-4.875	10.875	9.075	10.875	10.875	10.875	10.875	13.500	-3.600
G	6.300	4.500	0.000	6.300	-4.875	3.675	3.675	3.675	3.675	3.675	3.675	6.300	4.500
C	9.000	13.500	6.300	0.000	4.425	-2.625	-2.625	-2.625	-2.625	-2.625	-2.625	0.000	33.750
ROH	-3.375	-4.875	-4.875	4.425	0.000	5.850	2.250	5.850	5.850	5.850	5.850	4.425	-1.875
R1	6.375	10.875	3.675	-2.625	5.850	0.000	0.000	0.000	0.000	0.000	0.000	-2.625	10.875
R2	4.575	9.075	3.675	-2.625	2.250	0.000	0.000	0.000	0.000	0.000	0.000	-2.625	6.675
R3	6.375	10.875	3.675	-2.625	5.850	0.000	0.000	0.000	0.000	0.000	0.000	-2.625	10.875
R4	6.375	10.875	3.675	-2.625	5.850	0.000	0.000	0.000	0.000	0.000	0.000	-2.625	10.875
R5	6.375	10.875	3.675	-2.625	5.850	0.000	0.000	0.000	0.000	0.000	0.000	-2.625	10.875
C1	6.375	10.875	3.675	-2.625	5.850	0.000	0.000	0.000	0.000	0.000	0.000	-2.625	10.875
C2	9.000	13.500	6.300	0.000	4.425	-2.625	-2.625	-2.625	-2.625	-2.625	-2.625	0.000	13.500
W	-8.100	-3.600	4.500	33.750	-1.875	10.875	6.675	10.875	10.875	10.875	10.875	13.500	0.000

5. Summary and outlook

This work comprises detailed studies of two different systems using MD simulation. Besides using the same simulation technique, both studies treat model systems which lay the groundwork in order to understand more complex biological systems. The investigated key feature of both studies is self-organization, whether it be reversible bond breakage under force in chapter 3 or self-assembled phospholipid bilayers in chapter 4. The performed simulations are completing the view on this feature and offer a detailed insight which would not be accessible by experimental methods. MD simulations serve therefore indeed as a computational microscope.

5.1. Pulling parameter dependence in reversible force probe molecular dynamics simulations

With the invention of the AFM, micromanipulation of single molecules have become readily available and are an innovative way to study nanoscopic systems under force. Such stretching experiments offer a unique way to investigate fundamental theories of statistical mechanics but lack an atomistic description. Due to big advances in computational power and simulation techniques, FPMD simulations can provide a detailed atomistic view of such experiments. Biomolecules like proteins and RNA have been studied already extensively but from a physical point of view they have a major drawback: because of their complex structure, the probed energy landscape cannot be controlled. More sophisticated systems like the studied calix[4]arene-catenanes in chapter 3 offer the opportunity to study the energy landscape as a function of molecular design and external force. There, three different variations are studied. They differ in the length of their mechanically interlocked loops and can therefore be stretched more or less. Previous studies have shown that the system with the shorter loops, T14, can be understood as a two state model and the one with the longer loops, T17 and T20, represent three state models. The investigations done in this work extend these studies and a special focus is on the dependence of FPMD simulations on the pulling parameters K and V. In most existing models to understand FPMD simulations, only the loading rate, $\mu = KV$, does matter but not the individual values of K and V.
In section 3.3 FPMD simulations of the calixarene T14 are studied for various values of K and loading rates ranging from $0.08305\,\mathrm{N/s}$ to $83.05\,\mathrm{N/s}$. After a short introduction into the structural and mechanical features of the system, the dependence of the characteristic forces on the pulling parameters are investigated. It is shown that some of the rupture and rejoin forces are depending only very weakly on variations of K for a given loading rate whereas others show a strong K-dependence. This behavior can be easily understood in terms of a harmonic model for the energy landscape which allows to reproduce the found characteristic forces.
A special feature of the here studied systems is the hydrogen bond network. The two different states, open and closed, are stabilized by two different sets of hydrogen bonds. The average number of hydrogen bonds is studied as a function of the average end-to-end distance. Here, the number of hydrogen bonds which stabilize the open state depend on the chosen loading rate and for a given loading rate the number of these hydrogen bonds shows only a minimal dependence on K. For the average number of hydrogen bonds which stabilize the closed state, neither a μ-

nor a K-dependence can be found. Interestingly, these observed trends for the open and closed state are identical for the pull and relax mode. Furthermore, with the help of the hydrogen bond network, a working definition of the transition state T can be defined. The found transition state is nearer to the closed state than to the open state. This means, that the found open state has a rather brittle structure in the range of the here tested forces.
The kinetics of the transition from the closed to the open state is of great interest and many different models exist to rationalize the determined rates for such transitions. For the calculated rates for both transitions, closed to open in the pull mode and open to closed in the relax mode, no fit to existing expression derived from the mean first passage times for model energy landscapes nor a model-free determination of the distance to the barrier gives reasonable results. All of the here tested expression have the underlying assumption of a thermally activated transition. The failure of these fits can be a hint towards the fact that the simulations are performed in the crossover region from activated to diffusive dynamics. In order to further investigate this assumption, the reversible bond breaking observed in the FPMD simulations is considered to be a process of diffusive barrier crossing in a model potential. The potential of mean force of the investigated calixarene T14 was used and an external force applied. Trajectories were generated via KMC simulations and transition rates were calculated as inverse MFPTs. From the found results one can conjecture that the FPMD simulations are most probably in the dynamical regime of a crossover from activated dynamics to diffusive dynamics.
Section 3.4 treats FPMD simulations of the calixarene T17 and T20. These systems can be understood as three state models and are directly compared with the calixarene T14 due to structural similarities. A particular focus is on the hydrogen bond network, which is stabilizing the closed and intermediate state of the calixarenes T17 and T20 and the closed and open state of the calixarene T14. The open state O of the calixarenes T17 and T20 are only stabilized by the entangled loops. Comparing the characteristic forces and their corresponding end-to-end distances of all three systems, one finds a big similarity: as long as the hydrogen bond network is involved, the found values differ only minimally. Furthermore the degree of reversibility is tuned by the length of the entangled loops: the further the calixarene system can be stretched, the less likely it is that the system finds its way back into the closed state. This gives complete control over the energy landscape and the degree of reversibility.
In this work, FPMD simulations of the sophisticated model systems calixarene T14, T17 and T20 are shown to give a detailed insight into the behavior of reversible bond breakage which would not be possible experimentally. Furthermore, these systems offer complete control over the degree of reversibility and it is possible to tune the energy landscape. They are therefore an ideal model system to study two and three state models. In this work the FPMD simulations were performed due to computational limitations with relatively high loading rates ($\sim 10^{-2}\,\mathrm{N/s}$) compared to those experimentally accessible ($\sim 10^{-8}\,\mathrm{N/s}$). In order to link the results obtained by FPMD simulations and by pulling experiments, slower pulling velocities for the simulations are needed. This can be achieved by reducing computational cost. The majority of the computational effort arises from the calculation of the solvent. By using a CG solvent, the costs can be reduced but calculating the interactions between CG solvent and an atomistic model is complex. Innovative methods like the adaptive resolution simulations (AdResS) method [106] allow to change the number of degrees of freedom of a system on-the-fly and are therefore promising approaches. The system can then pass from atomistic to CG resolution and vice versa as a function of the position of a molecule in the simulation box. For the FPMD simulations, the transition region from atomistic to CG has to be dynamic and change with the stretch of the calixarene. Such a dynamic approach for force probe simulations is not yet implemented in the existing program package. The well-studied calixarene systems offer an ideal testbed for the development of such

an approach because of the available information about the atomistic system.
Besides altering the systems and changing the solvent, the already performed FPMD simulations could be analyzed with the help of recent improvements in the theory of rapid force spectroscopy. The model by Bullerjahn [61] starts from a rigorous probabilistic model of bond dynamics and allows to extract expressions for the rupture force distributions and mean unbinding forces for slow and fast loading rates. With this model it could be further verified that the here performed FPMD simulations are indeed performed in the crossover region from activated to diffusive dynamics.

5.2. Molecular dynamics simulation of phospholipid bilayers

In order to understand functions and properties of lipid bilayers, a deep understanding of the overall structure and dynamics of these systems is required. MD simulations of simplified one-component and two-component models, so-called reconstituted lipid bilayers, offer deep insight into the properties and behavior of lipids even on a coarse grained level.
In this work the CG model of the phospholipid DPPC and DOPC are studied extensively using different MD approaches. The main focus of this work is on the phase behavior of these lipids. In order to induce a phase transition, the studied bilayer system are investigated over a large range of temperatures. Furthermore, the influence of cholesterol is investigated.
Through this work, a new parametrized CG model of the unsaturated DOPC is introduced. It is based on the CG MARTINI model but unlike the original model it is able to reproduce the liquid-to-gel transition in semi-quantitative agreement with the experimental data. This new model was obtained by varying the angle parameters of the bead which represents the C-C double bond. Furthermore, the influence of the mechanism of the phase transition and the influence in a two-component system on the saturated DPPC are investigated. In two-component systems, a phase-separation is expected for low temperatures which could not be observed on the investigated timescale.
The well-studied CG model of DPPC is investigated with particle-field approaches: the PF and the PPPF approach. These approaches take the CG model as a basis for further approximations and offer a significant speed-up of the simulations but are less accurate. Nonetheless, these approaches are an important step towards the simulation of systems on a mesoscale. Even though a phase transition could not be observed for neither one of the approaches, the liquid phase is well described by the PF approach and the gel phase by the PPPF approach.
Besides the abundant phospholipids, cholesterol is an important component in mammalian cells. Due to its rigid structure it increases the order within the lipid bilayer and a liquid-ordered phase is formed. This phase is important for the abundance of a cell wall in mammalian cells. The characteristics of the liquid-ordered phase is a compact structure of the bilayer while maintaining a relatively high lateral diffusion coefficient of the lipids. Here, a new parametrized cholesterol model has been introduced for the PF approach which is able to reproduce the liquid-ordered phase with its main characteristics.
In this work, MD simulations of lipid bilayer systems using different approaches are shown to be a powerful tool for the investigation of reconstituted bilayer systems. All biological important phases (liquid, liquid-ordered and gel phase) have been shown to be described even by less accurate but vastly more efficient approaches. This offers new possibilities for future investigations of biological multicomponent bilayer systems on a mesoscale. Such future investigation could also involve integral membrane proteins which are important for the proper cell function. [107] Atomistic systems have already been studied but the large simulation volume of up to 300 000 atoms poses a major computational challenge. [108] By using the CG models for the lipids and

the PF approach used in this work the cost could be reduced.

Bibliography

[1] R. O. Dror, R. M. Dirks, J. P. Grossman, H. Xu, and D. E. Shaw, Annu. Rev. Biophys. **41**, 429 (2012).

[2] M. Karplus and J. A. McCammon, Nat. Struct. Mol. Biol. **9**, 646 (2002).

[3] B. J. Alder and T. E. Wainwright, J. Chem. Phys. **27**, 1208 (1957).

[4] A. Rahman, Phys. Rev. **136**, A405 (1964).

[5] J. A. McCammon, B. R. Gelin, and M. Karplus, Nature **267**, 585 (1977).

[6] S. A. Adcock and J. McCammon, Chem. Rev. **106**, 1589 (2006).

[7] H. Grubmüller, Methods Mol. Biol. **305**, 493 (2005).

[8] A. P. Lyubartsev and A. L. Rabinovich, Soft Matter **7**, 25 (2010).

[9] S. J. Marrink, H. J. Risselada, S. Yefimov, D. P. Tieleman, and A. H. de Vries, J. Phys. Chem. B **111**, 7812 (2007).

[10] A. De Nicola, Y. Zhao, T. Kawakatsu, D. Roccatano, and G. Milano, J. Chem. Theory Comput. **7**, 2947 (2011).

[11] M. Born and R. Oppenheimer, Ann. Phys. **389**, 457 (1927).

[12] R. Iftimie, P. Minary, and M. E. Tuckerman, Proc. Natl. Acad. Sci. U.S.A. **102**, 6654 (2005).

[13] T. D. Kühne, M. Krack, and M. Parrinello, J. Chem. Theory Comput. **5**, 235 (2009).

[14] D. Frenkel and B. Smit, Understanding Molecular Simulations: From Algorithms to Application, Academic Press, 2nd edition, 2002.

[15] M. P. Allen, NIC Series **23**, 1 (2004).

[16] P. P. Ewald, Ann. Phys. **369**, 253 (1921).

[17] V. Rokhlin, J. Comput. Phys. **60**, 187 (1985).

[18] T. Darden, D. York, and L. Pedersen, J. Chem. Phys. **98**, 10089 (1993).

[19] H. J. C. Berendsen, J. Chem. Phys. **81**, 3684 (1984).

[20] M. G. Saunders and G. A. Voth, Annu. Rev. Biophys. **42**, 73 (2013).

[21] G. Milano and T. Kawakatsu, J. Chem. Phys. **130**, 214106 (2009).

[22] S. J. Marrink and A. E. Mark, J. Am. Chem. Soc. **125**, 15233 (2003).

[23] M. Fuhrmans and S. J. Marrink, J. Am. Chem. Soc. **134**, 1543 (2012).

[24] M. Baaden and S. J. Marrink, Curr. Opin. Struct. Biol. **23**, 878 (2013).

[25] G. Milano, T. Kawakatsu, and A. D. Nicola, Physical Biology **10**, 045007 (2013).

[26] T. Kawakatsu, Statistical physics of polymers: an introduction, Springer, Berlin, 2004.

[27] P. J. Flory, Principles of polymer chemistry, Cornell Univ. Press, Ithaca, 10. printing edition, 1978.

[28] L. Jiang, Y. Gao, F. Mao, Z. Liu, and L. Lai, Proteins **46**, 190 (2002).

[29] S. Liu, C. Zhang, H. Zhou, and Y. Zhou, Proteins **56**, 93 (2004).

[30] H. J. C. Berendsen, Simulating the physical world : hierarchical modeling from quantum mechanics to fluid dynamics, Cambridge Univ. Press, Cambridge, 2007.

[31] A. Villa, C. Peter, and N. F. A. van der Vegt, J. Chem. Theory Comput. **6**, 2434 (2010).

[32] G. I. Bell, Science **200**, 618 (1978).

[33] E. Evans and K. Ritchie, Biophys. J. **72**, 1541 (1997).

[34] N. G. van Kampen, in Stochastic Processes in Physics and Chemistry (Third Edition), North-Holland Personal Library, Elsevier, Amsterdam, 2007.

[35] G. Hummer and A. Szabo, Biophys. J. **85**, 5 (2003).

[36] O. Dudko, Phys. Rev. Lett. **96** (2006).

[37] N. Metropolis and S. Ulam, JASA **44**, 335 (1949).

[38] D. T. Gillespie, J. Comput. Phys. **22**, 403 (1976).

[39] D. T. Gillespie, J. Phys. Chem. **81**, 2340 (1977).

[40] N. Agmon and J. J. Hopfield, J. Chem. Phys **78**, 6947 (1983).

[41] M. Rief and H. Grubmüller, ChemPhysChem **3**, 255 (2002).

[42] G. Binnig, C. F. Quate, and C. Gerber, Phys. Rev. Lett. **56**, 930 (1986).

[43] E. L. Florin, V. T. Moy, and H. E. Gaub, Science **264**, 415 (1994).

[44] H. Grubmüller, B. Heymann, and P. Tavan, Science **271**, 997 (1996).

[45] J. Liphardt, B. Onoa, S. B. Smith, I. Tinoco, and C. Bustamante, Science **292**, 733 (2001).

[46] M. Janke et al., Nat. Nanotechnol. **4**, 225 (2009).

[47] G. Gil-Ramírez, D. A. Leigh, and A. J. Stephens, Angew. Chem. Int. Ed. **54**, 6110 (2015).

[48] T. Schlesier and G. Diezemann, J. Phys. Chem. B **117**, 1862 (2013).

[49] T. Schlesier, T. Metzroth, A. Janshoff, J. Gauss, and G. Diezemann, J. Phys. Chem. B **115**, 6445 (2011).

[50] B. Hess, C. Kutzner, D. van der Spoel, and E. Lindahl, J. Chem. Theory Comput. **4**, 435 (2008).

[51] W. L. Jorgensen and J. Tirado-Rives, J. Am. Chem. Soc. **110**, 1657 (1988).

[52] W. L. Jorgensen, D. S. Maxwell, and J. Tirado-Rives, J. Am. Chem. Soc. **118**, 11225 (1996).

[53] G. Bussi, D. Donadio, and M. Parrinello, J. Chem. Phys. **126**, 014101 (2007).

[54] M. Parrinello and A. Rahman, Phys. Rev. Lett. **45**, 1196 (1980).

[55] G. Diezemann and A. Janshoff, J. Chem. Phys. **129**, 084904 (2008).

[56] G. Diezemann, J. Chem. Phys. **140**, 184905 (2014).

[57] M. Manosas, D. Collin, and F. Ritort, Phys. Rev. Lett. **96**, 218301 (2006).

[58] Y. Zhang and O. K. Dudko, Proc. Natl. Acad. Sci. U.S.A. **110**, 16432 (2013).

[59] A. Maitra, Phys. Rev. Lett. **104** (2010).

[60] O. K. Dudko, G. Hummer, and A. Szabo, Proc. Natl. Acad. Sci. U.S.A. **105**, 15755 (2008).

[61] J. T. Bullerjahn, S. Sturm, and K. Kroy, Nat. Commun. **5**, 4463 (2014).

[62] M. Balsera, S. Stepaniants, S. Izrailev, Y. Oono, and K. Schulten, Biophys. J. **73**, 1281 (1997).

[63] G. van Meer, D. R. Voelker, and G. W. Feigenson, Nat. Rev. Mol. Cell Biol. **9**, 112 (2008).

[64] M. Venturoli, M. Maddalena Sperotto, M. Kranenburg, and B. Smit, Phys. Rep. **437**, 1 (2006).

[65] E. Gorter and F. Grendel, J. Exp. Med. **41**, 439 (1925).

[66] J. F. Danielli and H. Davson, J. Cell. Comp. Physiol. **5**, 495 (1935).

[67] S. J. Singer and G. L. Nicolson, Science **175**, 720 (1972).

[68] W. Helfrich, Z. Naturforsch. C Bio. Sci. **28**, 693 (1973).

[69] W. Rawicz, K. C. Olbrich, T. McIntosh, D. Needham, and E. Evans, Biophys. J. **79**, 328 (2000).

[70] K. Olbrich, W. Rawicz, D. Needham, and E. Evans, Biophys. J. **79**, 321 (2000).

[71] M. D. Daily, B. N. Olsen, P. H. Schlesinger, D. S. Ory, and N. A. Baker, J. Chem. Theory Comput. **10**, 2137 (2014).

[72] E. Corvera, O. G. Mouritsen, M. A. Singer, and M. J. Zuckermann, Biochim. Biophys. Acta **1107**, 261 (1992).

[73] D. Needham and R. S. Nunn, Biophys. J. **58**, 997 (1990).

[74] S. Bhattacharya and S. Haldar, Biochim. Biophys. Acta **1467**, 39 (2000).

[75] J. L. Rubenstein, B. A. Smith, and H. M. McConnell, Proc. Natl. Acad. Sci. U.S.A. **76**, 15 (1979).

[76] N. Kučerka, S. Tristram-Nagle, and J. F. Nagle, J. Membr. Biol. **208**, 193 (2006).

[77] M. Kranenburg and B. Smit, J. Phys. Chem. B **109**, 6553 (2005).

[78] N. R. Council, Fat Content and Composition of Animal Products: Proceedings of a Symposium, The National Academies Press, Washington, DC, 1976.

[79] L. Martinez, J. Agric. Food Chem. **52**, 3434 (2004).

[80] R. Koynova and M. Caffrey, Biochim. Biophys. Acta **1376**, 91 (1998).

[81] S. J. Marrink, A. H. de Vries, and D. P. Tieleman, Biochim. Biophys. Acta **1788**, 149 (2009).

[82] S. J. Marrink, J. Risselada, and A. E. Mark, Chem. Phys. Lipids **135**, 223 (2005).

[83] G. W. Feigenson, Nat. Chem. Biol. **2**, 560 (2006).

[84] G. W. Feigenson, Annu. Rev. Biophys. **36**, 63 (2007).

[85] R. Faller and S. J. Marrink, Langmuir **20**, 7686 (2004).

[86] S.-J. Marrink and A. E. Mark, Biophys. J. **87**, 3894 (2004).

[87] M. W. Matsen and M. Schick, Phys. Rev. Lett. **72**, 2660 (1994).

[88] F. Drolet and G. H. Fredrickson, Phys. Rev. Lett. **83**, 4317 (1999).

[89] G. H. Fredrickson, V. Ganesan, and F. Drolet, Macromolecules **35**, 16 (2002).

[90] Y. Lauw, F. A. M. Leermakers, and M. A. Cohen Stuart, J. Phys. Chem. B **110**, 465 (2006).

[91] E. Dickinson, V. J. Pinfield, D. S. Horne, and F. A. M. Leermakers, J. Chem. Soc., Faraday Trans. **93**, 1785 (1997).

[92] A. C. Balazs, C. Singh, and E. Zhulina, Macromolecules **31**, 8370 (1998).

[93] J.-R. Roan and T. Kawakatsu, J. Chem. Phys. **116**, 7283 (2002).

[94] J.-R. Roan and T. Kawakatsu, J. Chem. Phys. **116**, 7295 (2002).

[95] J. Zidar et al., J. Phys. Chem. B **113**, 15795 (2009).

[96] M. Fraňová, J. Repáková, P. Čapková, J. M. Holopainen, and I. Vattulainen, J. Phys. Chem. B **114**, 2704 (2010).

[97] F. Castro-Román, R. W. Benz, S. H. White, and D. J. Tobias, J. Phys. Chem. B **110**, 24157 (2006).

[98] S. J. Marrink and A. E. Mark, J. Phys. Chem. B **105**, 6122 (2001).

[99] A. L. Kuo and C. G. Wade, Biochemistry **18**, 2300 (1979).

[100] B.-S. Lee, S. A. Mabry, A. Jonas, and J. Jonas, Chem. Phys. Lipids **78**, 103 (1995).

[101] R. Baron, A. H. de Vries, P. H. Hünenberger, and W. F. van Gunsteren, J. Phys. Chem. B **110**, 8464 (2006).

[102] A. A. Spector and M. A. Yorek, J. Lipid Res. **26**, 1015 (1985).

[103] T. T. Mills, J. Huang, G. W. Feigenson, and J. F. Nagle, Gen. Physiol. Biophys. **28**, 126 (2009).

[104] W. F. D. Bennett, J. L. MacCallum, M. J. Hinner, S. J. Marrink, and D. P. Tieleman, J. Am. Chem. Soc. **131**, 12714 (2009).

[105] H. J. Risselada and S. J. Marrink, PNAS **105**, 17367 (2008).

[106] H. Wang, C. Schütte, and L. Delle Site, J. Chem. Theory Comput. **8**, 2878 (2012).

[107] J. Eichler, European Journal of Biochemistry **267**, 3402 (2000).

[108] J. Gumbart, Y. Wang, A. Aksimentiev, E. Tajkhorshid, and K. Schulten, Current Opinion in Structural Biology **15**, 423 (2005).

[109] M. Allen and D. Tildesley, Computer Simulations of Liquids, Oxford Science Publications, Oxford, 1987.

[110] B. Hess, H. Bekker, H. J. C. Berendsen, and J. G. E. M. Fraaije, J. Comput. Chem. **18**, 1463 (1997).

[111] H. C. Andersen, J. Chem. Phys. **72**, 2384 (1980).

A. Computational details

A.1. Periodic Boundary Conditions PBC

The aim of MD simulations is to provide information about the properties of a macroscopic system but most simulated systems only probe a system with a few hundred to thousand particles and are thereby far away from the thermodynamic limit. For such small systems, boundary conditions do not have a negligible effect because for N particles in a system, $N^{2/3}$ are at the surface. Even for a system consisting of $N = 10^6$ particles this would mean that 1 % are at the surface.
A solution to this problem are periodic boundary conditions (PBC). The volume containing the N particles is treated as the primitive cell in a lattice of identical cells (see Figure A.1). Here a given particle interacts with all the periodic images and as well with its own periodic image.

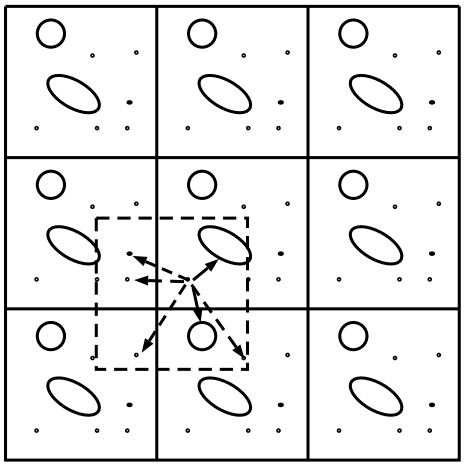

Figure A.1.: Representation of periodic boundary conditions.

A.2. Calixarene FPMD simulations

All simulations were performed using the GROMACS 4.0.7 program package [50] employing the OPLS-AA force field [51] [52]. For the short-ranged interactions a cut-off of 1.4 nm was used, the long-range Coulomb-interactions were treated using the particle mesh Ewald summation method [18] and for the van der Waals interaction a dispersion correction [109] was applied. Periodic boundary conditions were used and the simulation time-step was 2 fs which is possible because the bonded interactions were constrained to their equilibrium values using the LINCS-algorithm [110]. The neighbor list was updated every 10 fs. As solvent, mesitylene like in the experiment [46] was used.

B. Bulk properties

B.1. Dynamic strength

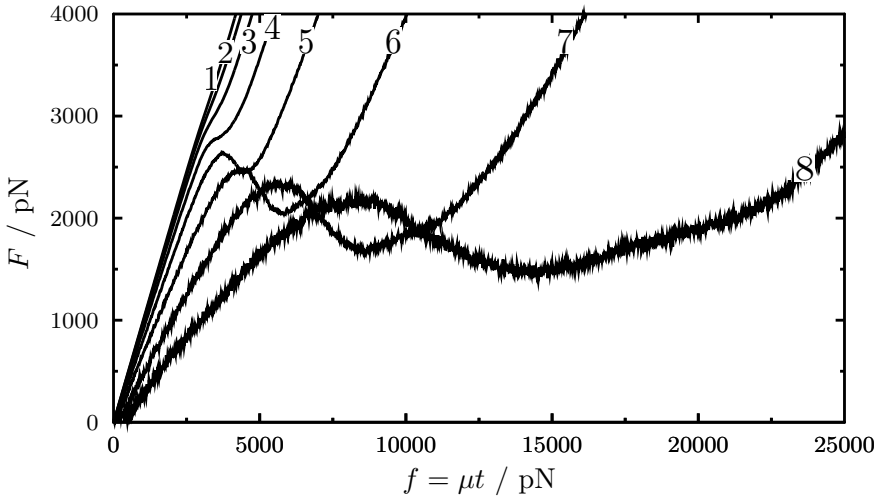

Figure B.1.: Dynamic strength (pull mode), i.e. the Ff curves averaged over 100 simulation for a loading rate of $\mu = 83.05\,\mathrm{N/s}$ plotted versus the applied force $f = \mu t$. The parameters for the curves are as follows: (1) $K = 0.2048\,\mathrm{N/m}$ and $V = 400\,\mathrm{m/s}$, (2) $K = 0.4153\,\mathrm{N/m}$ and $V = 200\,\mathrm{m/s}$, (3) $K = 0.8305\,\mathrm{N/m}$ and $V = 100\,\mathrm{m/s}$, (4)$K = 1.661\,\mathrm{N/m}$ and $V = 50\,\mathrm{m/s}$, (5) $K = 3.322\,\mathrm{N/m}$ and $V = 25\,\mathrm{m/s}$, (6) $K = 6.644\,\mathrm{N/m}$ and $V = 12.5\,\mathrm{m/s}$, (7) $K = 13.288\,\mathrm{N/m}$ and $V = 6.25\,\mathrm{m/s}$, (8) $K = 26.576\,\mathrm{N/m}$ and $V = 3.125\,\mathrm{m/s}$.

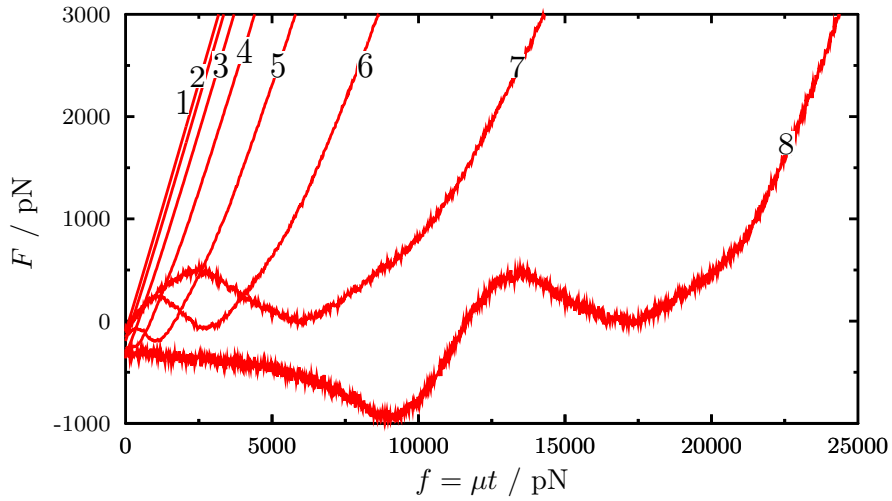

Figure B.2.: Dynamic strength (relax mode), i.e. the Ff curves averaged over 100 simulation for a loading rate of $\mu = 83.05\,\mathrm{N/s}$ plotted versus the applied force $f = \mu t$. The parameters for the curves are as follows: (1) $K = 0.2048\,\mathrm{N/m}$ and $V = 400\,\mathrm{m/s}$, (2) $K = 0.4153\,\mathrm{N/m}$ and $V = 200\,\mathrm{m/s}$, (3) $K = 0.8305\,\mathrm{N/m}$ and $V = 100\,\mathrm{m/s}$, (4)$K = 1.661\,\mathrm{N/m}$ and $V = 50\,\mathrm{m/s}$, (5) $K = 3.322\,\mathrm{N/m}$ and $V = 25\,\mathrm{m/s}$, (6) $K = 6.644\,\mathrm{N/m}$ and $V = 12.5\,\mathrm{m/s}$, (7) $K = 13.288\,\mathrm{N/m}$ and $V = 6.25\,\mathrm{m/s}$, (8) $K = 26.576\,\mathrm{N/m}$ and $V = 3.125\,\mathrm{m/s}$.

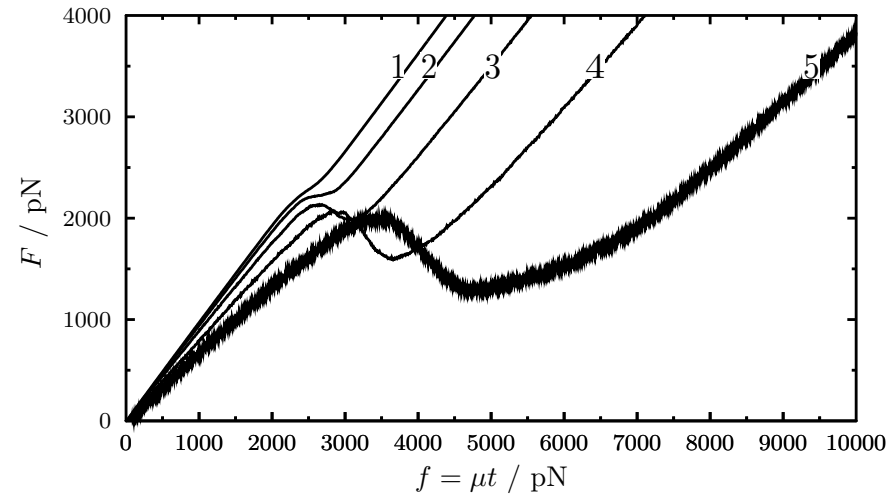

Figure B.3.: Dynamic strength (pull mode), i.e. the Ff curves averaged over 100 simulation for a loading rate of $\mu = 8.305\,\mathrm{N/s}$ plotted versus the applied force $f = \mu t$. The parameters for the curves are as follows: (1) $K = 0.4153\,\mathrm{N/m}$ and $V = 20\,\mathrm{m/s}$, (2) $K = 0.8305\,\mathrm{N/m}$ and $V = 10\,\mathrm{m/s}$, (3)$K = 1.661\,\mathrm{N/m}$ and $V = 5\,\mathrm{m/s}$, (4) $K = 3.322\,\mathrm{N/m}$ and $V = 2.5\,\mathrm{m/s}$, (5) $K = 6.644\,\mathrm{N/m}$ and $V = 1.25\,\mathrm{m/s}$.

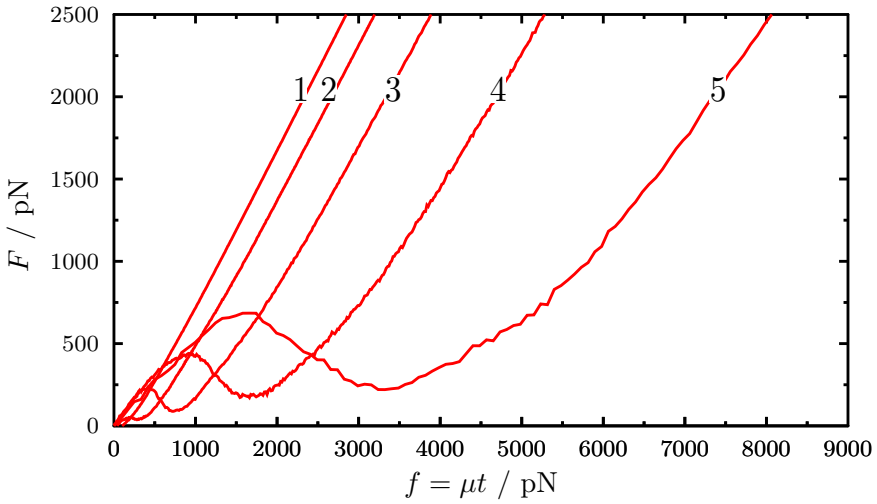

Figure B.4.: Dynamic strength (relaxl mode), i.e. the Ff curves averaged over 100 simulation for a loading rate of $\mu = 8.305\,\mathrm{N/s}$ plotted versus the applied force $f = \mu t$. The parameters for the curves are as follows: (1) $K = 0.4153\,\mathrm{N/m}$ and $V = 20\,\mathrm{m/s}$, (2) $K = 0.8305\,\mathrm{N/m}$ and $V = 10\,\mathrm{m/s}$, (3)$K = 1.661\,\mathrm{N/m}$ and $V = 5\,\mathrm{m/s}$, (4) $K = 3.322\,\mathrm{N/m}$ and $V = 2.5\,\mathrm{m/s}$, (5) $K = 6.644\,\mathrm{N/m}$ and $V = 1.25\,\mathrm{m/s}$.

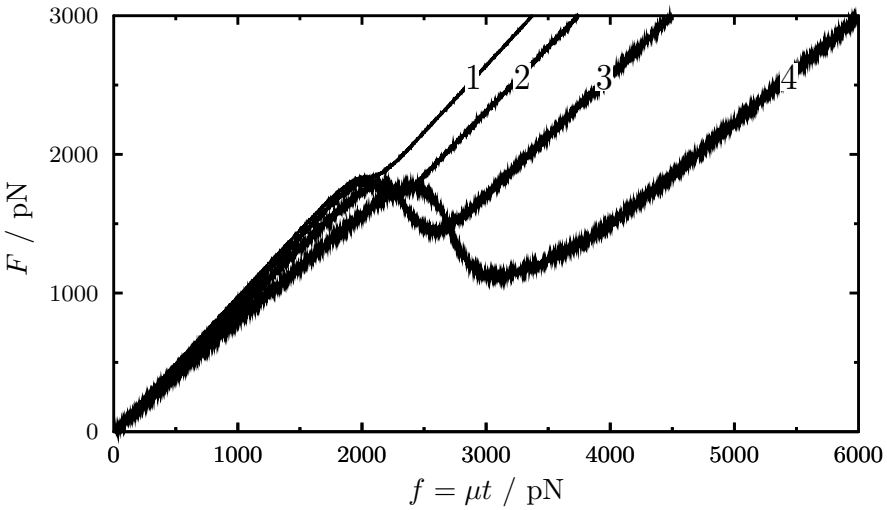

Figure B.5.: Dynamic strength (pull mode), i.e. the Ff curves averaged over 100 simulation for a loading rate of $\mu = 0.8305\,\mathrm{N/s}$ plotted versus the applied force $f = \mu t$. The parameters for the curves are as follows: (1) $K = 0.4153\,\mathrm{N/m}$ and $V = 2\,\mathrm{m/s}$, (2) $K = 0.8305\,\mathrm{N/m}$ and $V = 1\,\mathrm{m/s}$, (3)$K = 1.661\,\mathrm{N/m}$ and $V = 0.5\,\mathrm{m/s}$, (4) $K = 3.322\,\mathrm{N/m}$ and $V = 0.25\,\mathrm{m/s}$.

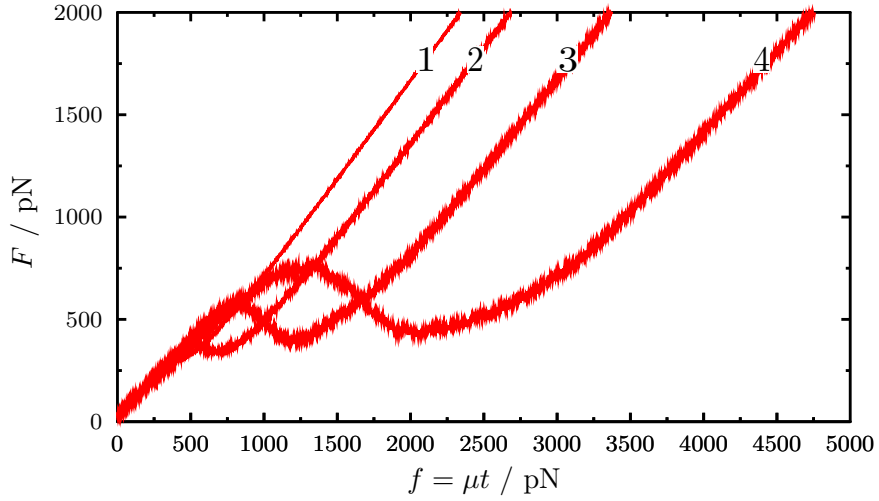

Figure B.6.: Dynamic strength (relax mode), i.e. the Ff curves averaged over 100 simulation for a loading rate of $\mu = 0.8305\,\mathrm{N/s}$ plotted versus the applied force $f = \mu t$. The parameters for the curves are as follows: (1) $K = 0.4153\,\mathrm{N/m}$ and $V = 2\,\mathrm{m/s}$, (2) $K = 0.8305\,\mathrm{N/m}$ and $V = 1\,\mathrm{m/s}$, (3)$K = 1.661\,\mathrm{N/m}$ and $V = 0.5\,\mathrm{m/s}$, (4) $K = 3.322\,\mathrm{N/m}$ and $V = 0.25\,\mathrm{m/s}$.

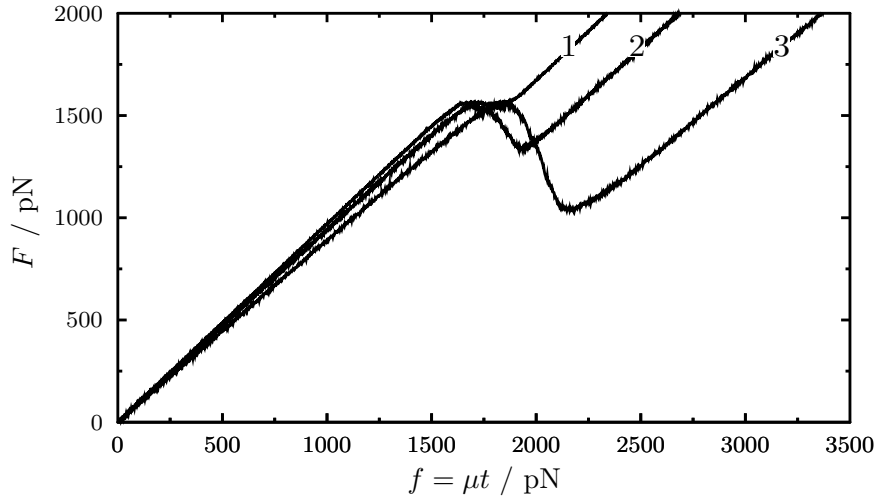

Figure B.7.: Dynamic strength (pull mode), i.e. the Ff curves averaged over 100 simulation for a loading rate of $\mu = 0.8305\,\mathrm{N/s}$ plotted versus the applied force $f = \mu t$. The parameters for the curves are as follows: (1) $K = 0.4153\,\mathrm{N/m}$ and $V = 0.2\,\mathrm{m/s}$, (2) $K = 0.8305\,\mathrm{N/m}$ and $V = 0.1\,\mathrm{m/s}$, (3)$K = 1.661\,\mathrm{N/m}$ and $V = 0.05\,\mathrm{m/s}$.

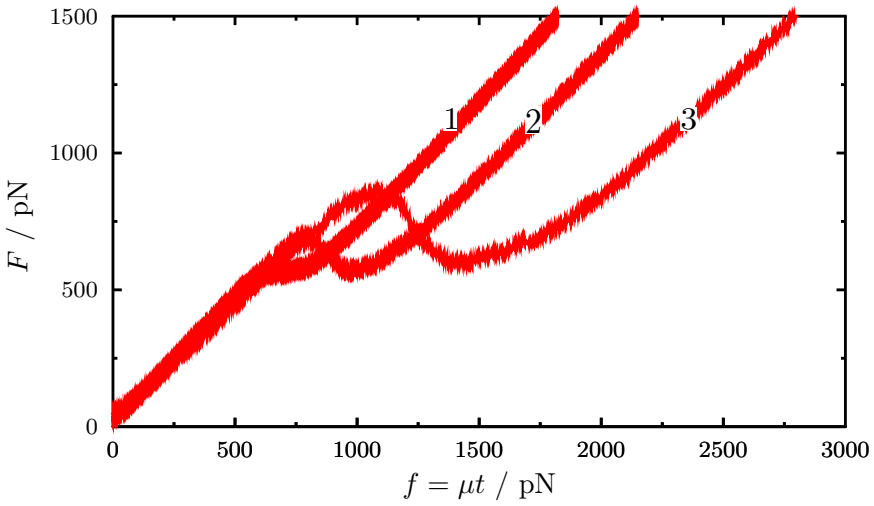

Figure B.8.: Dynamic strength (relax mode), i.e. the Ff curves averaged over 100 simulation for a loading rate of $\mu = 0.8305\,\mathrm{N/s}$ plotted versus the applied force $f = \mu t$. The parameters for the curves are as follows: (1) $K = 0.4153\,\mathrm{N/m}$ and $V = 0.2\,\mathrm{m/s}$, (2) $K = 0.8305\,\mathrm{N/m}$ and $V = 0.1\,\mathrm{m/s}$, (3)$K = 1.661\,\mathrm{N/m}$ and $V = 0.05\,\mathrm{m/s}$.

B.2. Hydrogen bonds

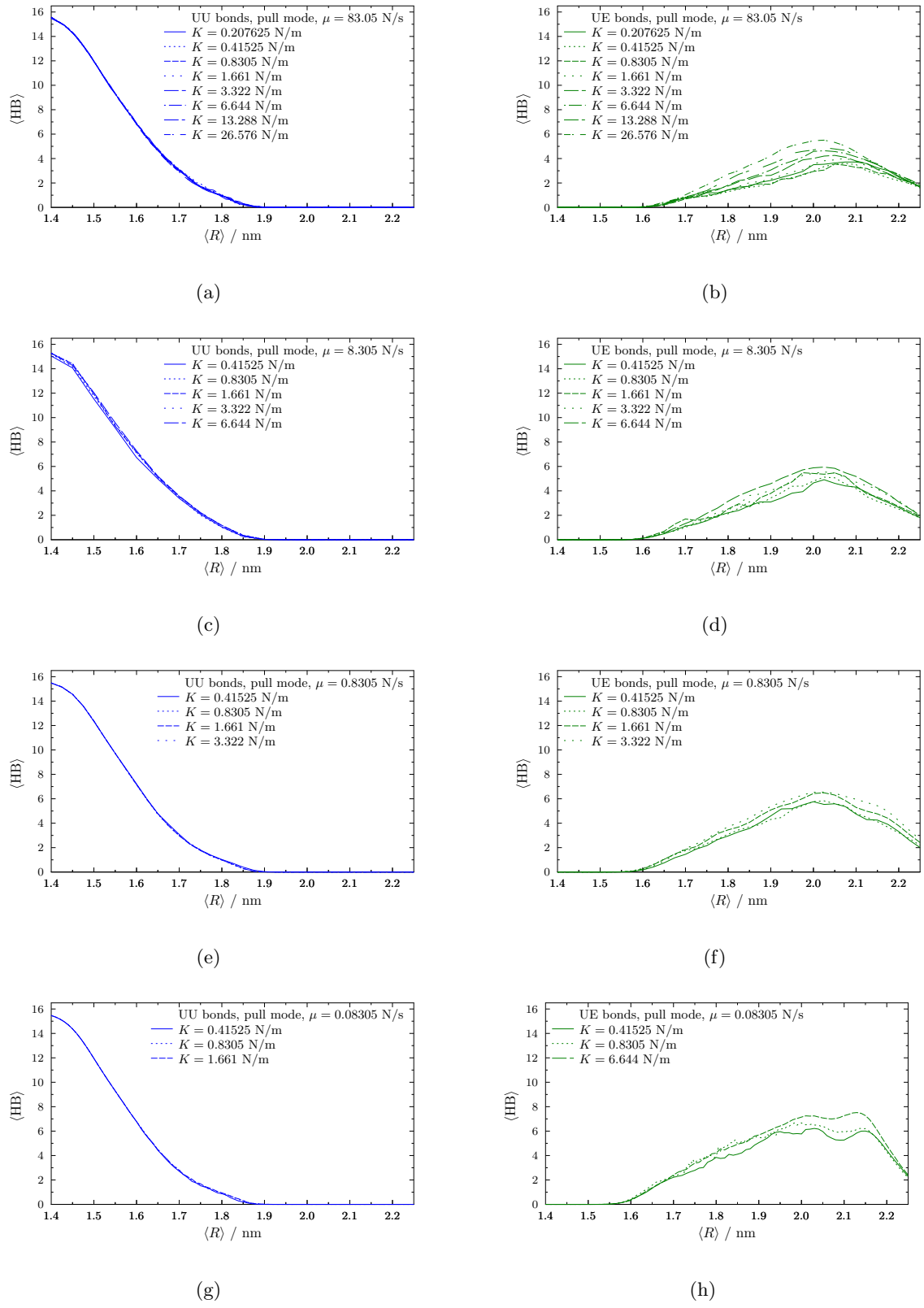

Figure B.9.: Pull mode: UU and UE bonds as a function of R for a loading rates ranging from $\mu = 0.08305 - 83.05\,\mathrm{N/s}$ and different sets of V and K.

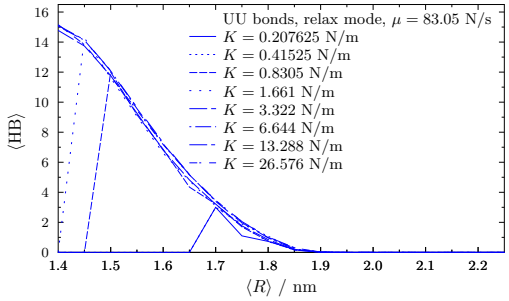

(a) Averaged UU bonds as a function of the end-to-end distance R.

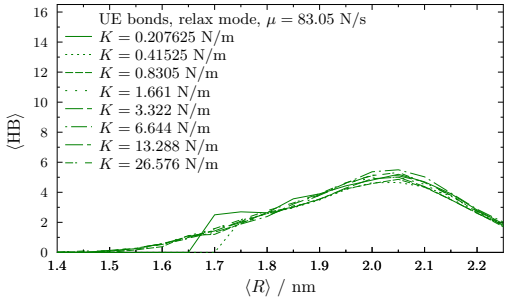

(b) Averaged UE bonds as a function of the end-to-end distance R.

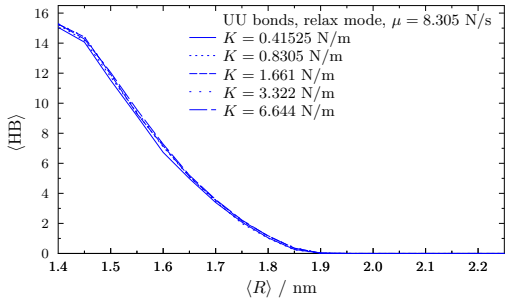

(c) Averaged UU bonds as a function of the end-to-end distance R.

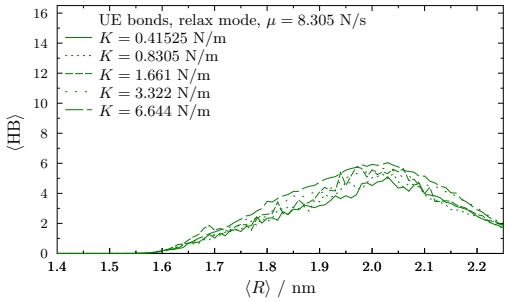

(d) Averaged UE bonds as a function of the end-to-end distance R.

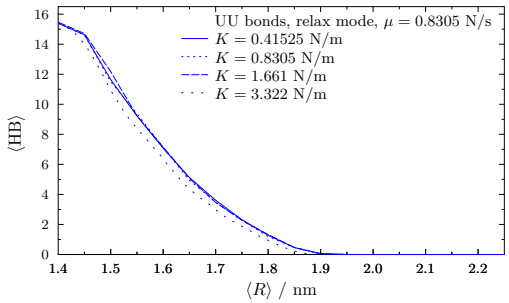

(e) Averaged UU bonds as a function of the end-to-end distance R.

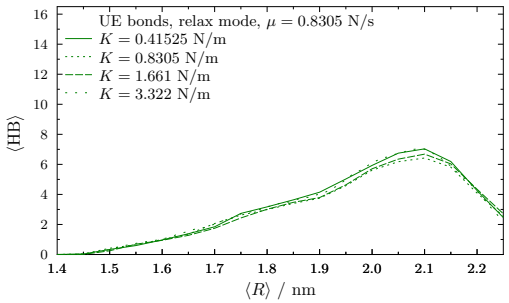

(f) Averaged UE bonds as a function of the end-to-end distance R.

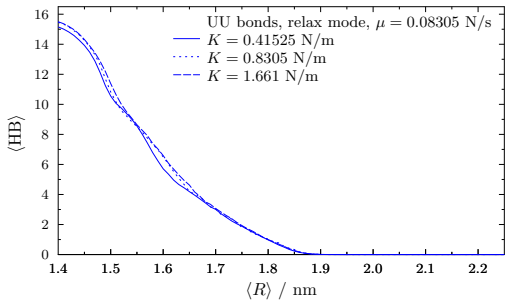

(g) Averaged UU bonds as a function of the end-to-end distance R.

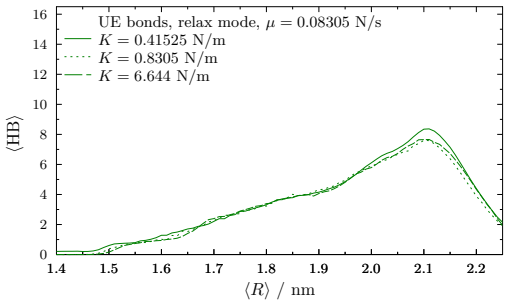

(h) Averaged UE bonds as a function of the end-to-end distance R.

Figure B.10.: Relax mode: UU and UE bonds as a function of R for a loading rates ranging from $\mu = 0.08305 - 83.05\,\mathrm{N/s}$ and differemt sets of V and K.

B.3. Polynomial describtion of the PMF

The PMF $V_{\mathrm{PMF}}(q)$ from [48] for the OPLS AA force field was fitted with eq. (3.22) using polynomial regression. The obtained parameters are $a = 7575.000$, $b = -54187.208$ $c = 143930.350$ $d = -167235.988$ and $e = 71631.237$. The extrema (q_{C}, q_{T}, q_{O}) of eq. (3.22) are given by

$$\begin{aligned} q_{\mathrm{C}}(f) &= u(f) + v(f) - \frac{\alpha}{3} \qquad \text{for} \qquad u(f) < 0 \\ q_{\mathrm{O}}(f) &= u(f) + v(f) - \frac{\alpha}{3} \qquad \text{for} \qquad u(f) > 0 \\ q_{\mathrm{T}}(f) &= -\sqrt{-\frac{4}{3}p}\cos\left(\frac{1}{3}\arccos\left(-\frac{x(f)}{2}\sqrt{-\frac{27}{p^3}}\right) + \frac{\pi}{3}\right) - \frac{\alpha}{3} \end{aligned} \tag{B.1}$$

with

$$u(f) = \sqrt[3]{-\frac{x(f)}{2} + \sqrt{\Delta(f)}} \tag{B.2}$$

$$v(f) = \sqrt[3]{-\frac{x(f)}{2} - \sqrt{\Delta(f)}} \tag{B.3}$$

$$x(f) = \frac{2\alpha^3}{27} - \frac{\alpha\beta'}{3} + \gamma(f) \tag{B.4}$$

$$p = b - \frac{\alpha^2}{3} \tag{B.5}$$

and

$$\Delta(f) = \left(\frac{x(f)}{2}\right)^2 + \left(\frac{p}{3}\right)^3 \tag{B.6}$$

$$\alpha = \frac{3b}{4a} \tag{B.7}$$

$$\beta' = \frac{2c + K}{4a} \tag{B.8}$$

$$\gamma(f) = \frac{d - f - Kq_C^0}{4a}. \tag{B.9}$$

C. Computational details: Lipids and cholesterol

C.1. Particle-particle simulations

All particle-particle (PP) simulations were performed using the GROMACS 4.6 [50] program package employing the MARTINI force field [9]. For the short ranged interactions a cut-off of 0.9 nm was used. The long-range Coulomb-interactions and the van der Waals interaction were treated using shifted potentials. A semi-isotropic simulation box with periodic boundary conditions was used. The simulation time step was 40 fs which is possible because the bonded interactions were constrained to their equilibrium values using the LINCS-algorithm [110]. The neighbor list was updated every 400 fs.
The lipid systems were setup as follows: The simulated lipid was randomly distributed in a simulation box and the energy of this system was then minimized. The water and the anti freeze was added and the system was again energy minimized. After that, a NVT simulation was run until the bilayer was built. Then a NPT simulation with semi-isotropic pressure coupling was run to equilibrate the system. This equilibration run was stopped when the pressure and the temperature reached the desired value.
For the two-component systems consisting of DPPC and cholesterol the setup of the system is equivalent to the setup of the lipid system described above. The only exceptions are that the cholesterol was randomly distributed in the simulation box together with the lipid before the first energy minimization and only the standard MARTINI water model W was used. Here, no anti freeze particle are used because the system is not quenched to lower temperatures.

C.2. Particle-field and particle-particle particle-field simulations

All particle-field (PF) and particle-particle particle-field simulations were performed using the OCCAM package [21]. For the short-ranged interactions a cut-off of 0.9 nm for the PF simulations was used. The cut-off in PPPF simulations was subject to change but in most simulations around 0.52 nm The simulation time step was 30 fs and density field was updated every 300 fs. The box size was kept constant and the Andersen thermostat [111] was used. The values for the non-bonded parameters for the discussed lipids are subject to change. Charge, mass and the bonded-parameters for the used DPPC model are shown in Table C.1.
The starting configuration were taken from well equilibrated PP simulations. The box size was adjusted to an averaged value. The antifreeze particles from the PP simulations were replaced by water. The volume of the box had to be further adjusted in z direction because the anti freeze particles are larger than the used water particles.

C.3. Parameters for the phospholipid models

Table C.1.: Parameters for charge and mass and the bonded and angle functions [9] for the PP, PF and PPPF approach for DPPC.

i	bead	charge	mass	i	j	length	K	i	j	k	θ	K
1	N	1	72	1	2	0.47	1250	2	3	3	120.0	25.0
2	P	-1	72	2	3	0.47	1250	2	3	4	180.0	25.0
3	G	0	72	3	3	0.37	1250	3	4	4	180.0	25.0
4	C	0	72	3	4	0.47	1250	4	4	4	180.0	25.0

Table C.2.: Parameters for charge and mass and the bonded and angle functions [9] for the PP, PF and PPPF approach for DOPC.

i	bead	charge	mass	i	j	length	K	i	j	k	θ	K
1	N	1	72	1	2	0.47	1250.00	2	3	3	120.00	25.000
2	P	-1	72	2	3	0.47	1250.00	2	3	4	180.00	25.000
3	G	0	72	3	3	0.37	1250.00	3	4	4	180.00	25.000
4	C	0	72	3	4	0.47	1250.00	4	4	4	180.00	25.000
5	D	0	72	4	4	0.47	1250.00	4	5	4	120.00	45.000
-	-	-	-	5	4	0.47	1250.00	5	4	4	180.00	25.000

C.4. Additional graphs for the DPPC/DOPC two-component system

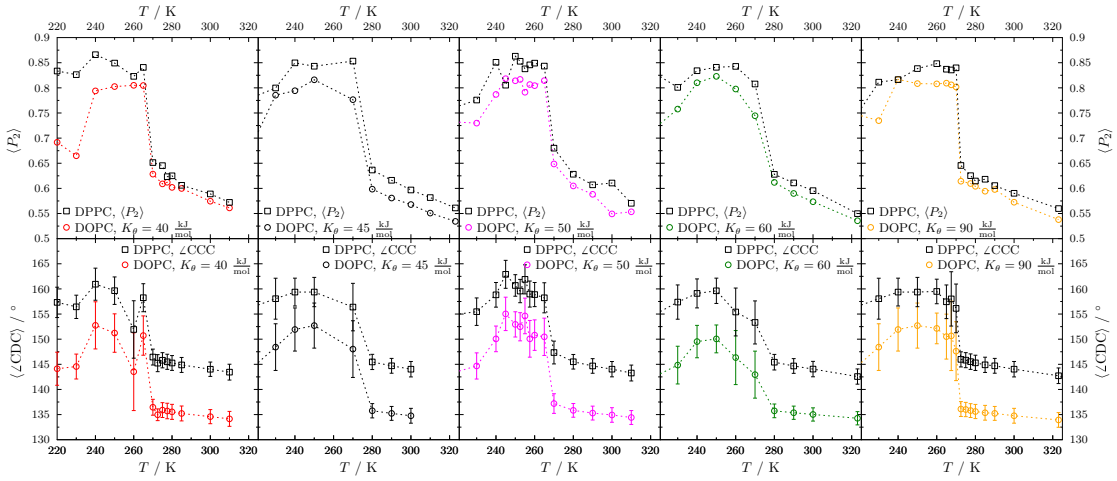

Figure C.1.: Order parameter $\langle P_2 \rangle$ and measured angle $\langle \angle \mathrm{CDC} \rangle$ as a function of the temperature for a DPPC/DOPC mixture with different values for K_{CDC}.

C.5. Particle-field simulations of the liquid-ordered phase

Here the setup of a system consisting of 128 DPPC, 32 CHOL and 2000 W simulated with the PF approach is described. As a starting configuration for the PF simulation, a snapshot of a well-equilibrated PP system of the same system (128 DPPC, 32 CHOL, 2000 W) was used. The initial box-size parameters were taken from a well-equilbrated PP simulation of a system consisting of 128 DPPC and 2000 W. In order to approximate additional volume taken by the 32 cholesterol, the results of section 4.3.1 were used. Here the area per cholesterol was approximated to be $0.350\,\mathrm{nm}^2$. With a bilayer thickness of about 0.41 nm the volume of the 32 cholesterol is $2.296\,\mathrm{nm}^3$. Assuming that the volume of a cholesterol is the same in the PF and PP approach is justified by the rigid structure.
In order to verify that the system is stable, a simulation of 1 μs starting from an well equilibrated snapshot was performed. The order parameter $\langle P_2 \rangle$ was recorded and showed only minor fluctuations and averaged at 0.53 ± 0.02. Furthermore number densities of DPPC, CHOL and ROH were recorded over 200 ns intervals and are in agreement with each other. Besides the structural properties, also the the recorded pressure and the potential energy stayed constant.

C.6. Parameters for the cholesterol model

Table C.3.: Bonded parameters as listed in [71].

i	j	r_{ij} / nm	K_{ij} / kJ mol^{-1}
1	2	0.184	$2.0 \cdot 10^4$
2	3	0.267	$2.0 \cdot 10^4$
2	4	0.433	$2.0 \cdot 10^4$
4	6	0.194	$2.0 \cdot 10^4$
4	7	0.499	$2.0 \cdot 10^4$
5	6	0.379	$2.0 \cdot 10^4$
6	7	0.599	$2.0 \cdot 10^4$
7	8	0.421	$1.25 \cdot 10^3$
2	6	0.416	$2.0 \cdot 10^4$
3	6	0.296	$2.0 \cdot 10^4$

Table C.4.: Constraints as listed in [71].

i	j	r_{ij} / nm
1	3	0.415
1	4	0.614
3	4	0.288
3	5	0.434
4	5	0.265
5	7	0.343

C.7. Influence of different mean-field parameters on the placement of CHOL

In order to improve the placement of the cholesterol, the influence of the different χ-parameters marked in different colors (see Table 4.8) are investigated in the following three paragraphs. An illustration of the varied parameters χ can be found in Figure 4.36. Firstly, the interaction between the head group ROH of the cholesterol and the head group of DPPC (N,P and G bead) is systematically analyzed. Secondly, the influence of the cholesterol with the water beads W is monitored.

1.Variation of the ROH-cholesterol / head-lipid mean field parameters Here, the mean field parameters χ and χ are varied. These parameters represent the attractive short-range interactions between the head group of the lipids and the group of the cholesterol (see Figure 4.36). By multiplying these parameters with a factor up to five, the influence on the placement of the cholesterol of these χ-paramters are investigated. The resulting number densities are shown in Figure C.2 and compared with the results obtained from the PP simulation (solid black line).

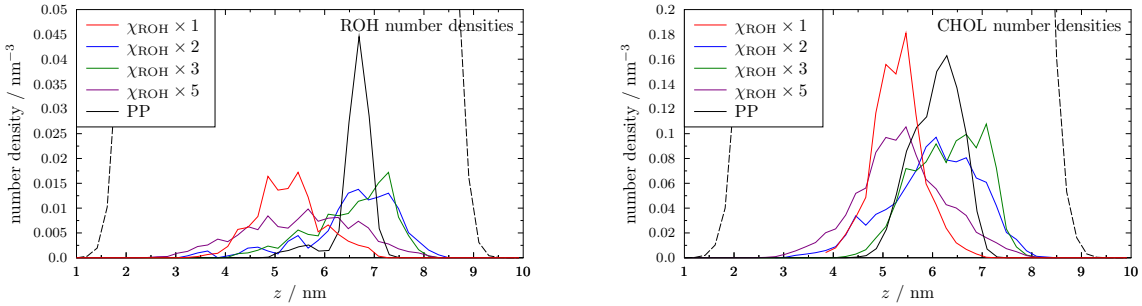

(a) ROH number densities.

(b) CHOL number densitites.

Figure C.2.: Comparision of the number densities. The black dotted line is the number density of DPPC and is there to visualize the position of the cholesterol.

For an factor of two (blue line) the maximum of the number density shifts nearer to the bilayer surface at $z \approx 9\,\mathrm{nm}$ but also the number density is broadening. For an even higher factor of three (green line) this trend is even increasing. By increasing the factor further to five, the shift towards the bilayer surface is decreasing but the number density is further broadening. The observed broadening for higher factors (≥ 5) is due to the fact that now the reach of the attractive interactions between the lipid head-group and the ROH-bead is so far increased that the position of the cholesterol is also influenced by opposite lipid bilayer surface.

2. Variation of the cholesterol / water mean field parameters Here the parameters χ, χ and χ were varied. These parameters describe the interactions between the hydrophilic head-group ROH and the the water beads W and the hydrophobic interactions between the "body" / the tail of the cholesterol and the water beads (see Figure 4.36). Like in the previous paragraph, the χ-parameters were multiplied with different factors and the number densities were monitored. The results are shown in Figure C.3.

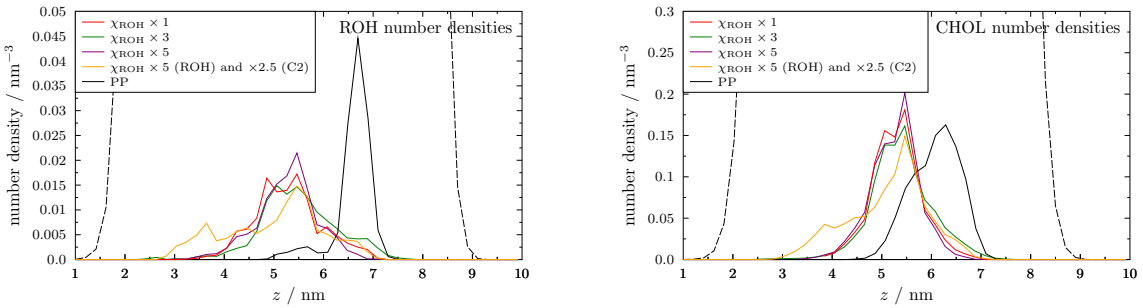

(a) ROH number densities.

(b) CHOL number densitites.

Figure C.3.: Comparision of the number densities. The black dotted line is the number density of DPPC and is there to visualize the position of the cholesterol.

Varying these parameters all at once with the same factor has only a minor effect on the placement of the cholesterol within the lipid bilayer. This is due to the fact that the turned up attractive parameters of the ROH-bead are counteracted by the repulsive parameters between the C-type beads of the cholesterol. In order to improve the orientation of the cholesterol only the interaction between the head group ROH and the "tail" group C2 were varied. Here, the hydrophilic interactions between the head group and the water were increased by a factor of five ($\chi \times 5$) and the hydrophobic interactions between the tail of the cholesterol were increased by an factor of 2.5 ($\chi \times 2.5$). By doing that, the head group is attracted more towards the lipid bilayer and at the same time the tail group is repulsed. This forces the cholesterol to align along the z-axis which can also be seen in Figure C.3 (solid orange line). The peak at $z \approx 3.5\,\mathrm{nm}$ is due to the fact that the cholesterol also attracted to the bilayer surface at the other side and therefore shows an flip-flop mechanism.

Optimized parameters

- $\chi \times 5$ and $\chi \times 10$: By increasing the attractive interaction between the ROH-bead and the beads of the head group of lipid, the cholesterol is placed nearer to the bilayer surface. Note that these values are higher than the sensible values discussed above in the first paragraph. There, the best results are obtained for a factor of three and for higher factors a broadening of the number density is observed. This broadening is not observed here because the interaction between cholesterol and the water beads are chosen so that they counteract this problem (see below).

- $\chi \times 5$, $\chi \times 1$ and $\chi \times 2.5$: The attractive interaction between the ROH bead and the water W were increased by a factor of five. Therefore the head bead is further attracted towards the bilayer surface but not as much as towards the beads of the head group of the lipid. In order to align the cholesterol along the z-axis the repulsive interaction between the C2 bead and the water beads was multiplied by 2.5. The remaining C-beads of the cholesterol "body" were left as they are.

D. Publications

- *Mechanical unfolding pathway of a model β-peptide foldamer*
  L. Uribe, S. Jaschonek, J. Gauss, and G. Diezemann. J. Chem. Phys. **142**, 204901 (2015).
- *Force probe simulations of a reversibly rebinding system: Impact of pulling device stiffness*
  S. Jaschonek and G. Diezemann. J. Chem. Phys. **146**, 124901 (2017).